# Discontinuous Galerkin Methods for Magma Dynamics

by

Seshu Tirupathi

B.Tech., Indian Institute of Technology Kanpur, Uttar Pradesh, India, 2005

M. Eng., Cornell University, New York, USA, 2007

A dissertation submitted in partial fulfillment of the
requirements for the degree of Doctor of Philosophy
in the Division of Applied Mathematics at Brown University

PROVIDENCE, RHODE ISLAND

May 2014

Abstract of "Discontinuous Galerkin Methods for Magma Dynamics" by Seshu Tirupathi, Brown University, May 2014

## Abstract

Generation and segregation of magma in the Earth and the interior of large planets has been a subject of intensive study in the earth science community. In particular, a fundamental understanding of melt migration beneath the mid-ocean ridge is necessary to explain the field observations on sections of the earth's mantle that has been uplifted to the surface.

The physical model of melt migration in a heterogeneous mantle is given by an advection-reaction type system consisting of two hyperbolic equations to evolve porosity and soluble mineral abundance, opx, and one elliptic equation to recover the global pressure. In this work, high order discontinuous Galerkin (DG) methods are presented for numerical modeling of melt migration for both advection and elliptic equations.

In addition, assembling and solving the elliptic equation is identified as the major bottleneck in these computations. To address this issue, numerical methods with adaptive mesh refinement, novel methods like local timestepping methods and a projective and adaptively applied pressure estimation techniques have been developed to significantly reduce the computational wall time without impacting the overall physical reliability in the modeling of important features of melt and segregation.

Important geophysical consequences like the formation of high-porosity channels and compaction-dissolution waves, features like the shapes of opx-depleted regions called dunites and the affect of mantle heterogeneities in dunite channel formation have been explained through the results obtained from the numerical simulations.

This dissertation by Seshu Tirupathi is accepted in its present form
by the Division of Applied Mathematics as satisfying the
dissertation requirement for the degree of Doctor of Philosophy.

Date_____ _____

Jan S. Hesthaven, Ph.D., Advisor

Recommended to the Graduate Council

Date_____ _____

Mark Ainsworth, Ph.D., Reader

Date_____ _____

Yan Liang, Ph.D., Reader

Date_____ _____

Edgar M. Parmentier, Ph.D., Reader

Approved by the Graduate Council

Date_____ _____

Peter Weber, Dean of the Graduate School

To my parents and my brothers

## Vitae

Seshu Tirupathi was born on April 13, 1983 in Hyderabad, India. He graduated from Indian Institute of Technology(IIT) Kanpur in 2005 with a Bachelor's degree in Aerospace Engineering. He graduated with a Master's degree in Mechanical Engineering from Cornell University in May, 2007.

## Acknowledgments

I would like to thank my advisor Professor Jan Hesthaven for the guidance and support he has provided for the last six years. The freedom he gave me to explore and find answers on my own while being able to approach him without hesitation when needed provided for an invaluable learning experience. His constant encouragement, especially in the initial few years of my research, really helped me remain motivated.

I would also like to thank Professors Yan Liang and Marc Parmentier who provided the base for my research. Their way of breaking a big problem into mini-problems of interest based on the results at our weekly group meetings helped me understand both the physical significance of my results and opened up the mathematical and computational challenges that needed to be addressed.

I would also like to thank Professor Mark Ainsworth for agreeing to serve on my PhD committee and taking the time to read my thesis.

Many people have helped at various times during the last 5 years with various aspects of my project. In particular, I would like to thank Professor Wolfgang Bangerth, Professor Guido Kanschat, Alan Schiemenz, Chenguang Sun and Conroy Baltzell and the whole deal.II community for this. I would also like to thank CCV at Brown for helping me with the computational resources required for this project.

Finally, this work was supported in part by NSF grants DMS-0530862 and OCE-1156706.

To all my friends at Brown for making my life happy outside work. It was a wonderful experience hanging out with all of you and I hope we get to stay in touch after Brown as well. Last, but surely not the least, it will be unfair if I leave out

two people who have really made a difference in my life at Brown: Ravi and Rohini. Thank you.

# Contents

# List of Tables

# List of Figures

# Nomenclature

Table 1: List of parameters and the ballpark values

| Parameter | Description | Values |
|---|---|---|
| $c_f^0$ | Concentration of melt at inflow | 0.47 |
| $c_{ol}^0$ | Concentration of independent component in olivine | 0.5 |
| $c_{opx}^0$ | Concentration of independent component in opx | 0.55 |
| $g$ | Acceleration due to gravity | 10 $\text{ms}^{-2}$ |
| $L$ | Compaction length | $1 - 10$ km |
| $n$ | Porosity exponent in permeability | $2 - 3$ |
| $p^0$ | Pressure scale | |
| $\phi_f^0$ | Inflow porosity | 0.02 |
| $\phi_{opx}^0$ | Inflow opx fraction | 0.15 |
| $R$ | Ratio of buoyancy-driven melt velocity to solid upwelling rate | $10 - 10^4$ |
| $t^0$ | Upwelling timescale | 1Ma |
| $w_0$ | Inflow melt velocity | $1 - 100$ m $\text{yr}^{-1}$ |
| $W_0$ | Solid upwelling rate | $10 - 100$ mm $\text{yr}^{-1}$ |

| Parameter | Description | Values |
|---|---|---|
| $\alpha$ | Dissolution rate constant | $7 \times 10^3 - 4 \times 10^4$ $\text{yr}^{-1}$ |
| $\beta$ | Ratio of opx dissolution rate to olivine precipitation rate | 0.5 |
| $\delta$ | Dimensionless solubility gradient | $10^{-3} - 10^{-1}$ |
| $\Delta c$ | Change in equilibrium melt concentration per compaction length | $10^{-6}$ |
| $\Delta\rho$ | Density difference between solid and fluid | 500 $\text{kg/m}^3$ |
| $\Delta V$ | Velocity reduction of solid due to dissolution | $10^{-4} - 10^{-2}$ mm $\text{yr}^{-1}$ |
| $\Gamma_{opx}$ | opx dissolution rate | |
| $\kappa_\phi$ | Permeability | |
| $\xi$ | Bulk viscosity | |
| $\hat{c}$ | Characteristic concentration | 0.065 |
| $\eta$ | Shear viscosity of solid | $10^{18} - 10^{18}$ Pa s |
| $\kappa_0$ | Reference permeability | $5.10^{-14}$m |
| $\mu$ | Viscosity of melt | $1 - 10$ Pa s |

# Chapter 1

# Introduction

Generation and segregation of magma in the Earth and the interior of large planets has been a subject of intensive study in the earth science community. However our understanding of magma generation and segregation is constrained by physical and chemical evidence based on geological observations of rocks exposed on the surface. One important example is ophiolites which are sections of the earth's mantle that have been uplifted and exposed at the surface. Figure 1.1 shows the photomosaics of ophiolites observed in Oman. The key observation from these outcrops is the local depletion of a soluble mineral, orthopyroxene (opx). The elongated opx-depleted regions are referred to as dunite in the geological literature. The region where the soluble mineral (opx) and the insoluble mineral (ol) are present is called harzburgite. In Figure 1.1, the lighter rocks are dunite and the darker rocks are harzburgite respectively. Dunite channel features can be observed more clearly in Figure 1.2, also obtained from field observations discussed in [61] and [44]. The main objective of the present study is to develop high-order numerical methods that can help explain the formation of dunite channels through the study of the chemical interaction between melt and solid mantle during melt migration in deformable porous media.

There is a broad understanding of how dunites are formed chemically. Magma or melt is generated by adiabatic decompressional melting during upwelling in the

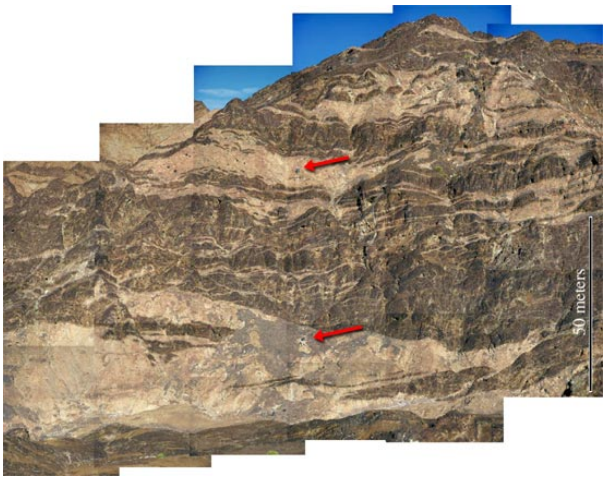


Figure 1.1: Photomosaic of a mountainside from Muscat Massif, Oman (taken from [8]). Lighter rocks marked by the red arrow are dunites and the dark brown region around the dunite are harzburgites.


Figure 1.2: Close up images of dunite channels taken from Cache Creek terrane in the Canadian Cordillera [61] on the left and from Massif du Sud, New Caledonia [44] on the right.

earth's upper mantle. Segregation of melt involves two-phase flow in which low viscosity melt percolates through a much more viscous solid matrix [9]. During its upward migration, melt generated in the deeper part of the upwelling mantle interacts both thermally and chemically with the overlying mantle through a reactive infiltration instability, whereby highly porous regions form due to a positive feedback between melt percolation and dissolution of the soluble mineral opx in the solid. This process results in the formation of dunite channels. On a related note, it has been suggested that high-permeability dunite channels act as conduits for focused flow, whereby melt may efficiently segregate from its source region while still maintaining its geochemical signature developed at depth. For further discussion we refer to [36, 35] and the references therein.

## 1.1 Approach

### 1.1.1 Physical Problem

Generation and segregation of melt in an upwelling mantle beneath the mid-ocean ridge involves interacting physical processes on a wide range of length scales. Melt generation takes place at the millimeter scale and this melt is driven by buoyancy forces and stresses that develop in the solid mantle, flowing on scales of hundreds of kilometers. This thesis focuses on the intermediate scale where buoyancy driven flow is considered and the time evolution of the fractions of melt and dissolvable mineral opx are explicitly tracked. The evolution of the soluble mineral (opx) is required to understand the formation of the observed opx-depletions and their spatial and temporal relation to localized melt flow in regions of high permeability. As discussed earlier, another important aspect of this thesis is to study the impact of dunite channels for the efficient extraction of melt formed in the deep mantle.

### 1.1.2 Numerical Methods

The governing partial differential equations for conservation of mass, momentum, and energy to model magma dynamics are highly nonlinear [43, 54, 7] and have to be solved numerically in almost all geological applications. Finite difference, finite volume (FVM) and finite element methods (FEM) are the standard spatial discretizations that have been used so far to solve the mass conservation or hyperbolic equations arising in magma dynamics. Early numerical study by Spiegelman *et al.* [59] used low order finite difference method which was both very efficient and simple. However, such methods cannot be extended easily to complex geometries and local grid size changes required to capture the local features of the solution, e.g. high-porosity channels which is a common feature in magma dynamics problems [59, 41, 53]. Finite volume methods have been used to model melt migration beneath the mid-ocean ridge [24, 33], and these methods provide the aforementioned geometric flexibility for lower order. However, increasing the order of accuracy in more than one dimension requires a particular grid structure and hence cannot be easily extended to general unstructured grids [30]. Unlike finite difference and finite volume methods, finite element discretization provides a very good alternative to address accuracy issues. Finite element methods assume that the solution is a linear combination of the basis functions which can be made arbitrarily high order to achieve the required accuracy [37]. The geometric flexibility of FEM also makes it feasible to use these methods in melt migration problems. Also, commercially available software packages make the application of FEM to certain cases in magma dynamics straightforward [11]. While these methods are ideal for elliptic equations i.e., to solve the pressure equation in the context of magma dynamics, they have some drawbacks for transport equations. Globally defined basis functions and the symmetric structure of the basis functions makes the semi-discrete scheme costly to implement and causes stability issues respectively. Apart from the standard methods, hybrid schemes have been developed to study melt migration problems. Examples include semi-Lagrangian

algorithms [57], mixed Fourier Collocation-discontinuous Galerkin method [52] and mixed discontinuous Galerkin and high-order finite difference method [41]. However these methods require significant amount of coding and can be prohibitively costly when extended to three dimensions.

Numerical methods that satisfy the requirements of high order accuracy with geometric flexibility through local approximation like finite elements and with stability requirements satisfied through methods like finite volume methods for transport problems are ideally suited for numerical computations in magma dynamics. These features can be achieved through a class of numerical methods termed discontinuous Galerkin (DG) methods.

## 1.2 Specifics of Hardware

All the computational experiments in this thesis have been performed with GNU C++ compiler (version 4.4.7) on Linux x86_64. The processor architecture is Intel Xeon E5540 (2.53 GHz) Nehalem with 8 cores and 24GB memory (DDR3, 1333 GHz).

## 1.3 Overview/Structure

This thesis is organized into 9 chapters concentrating on the numerical methods as well as the geological implications of the results obtained through the numerical simulations. An overview of each chapter is given below:

**Chapter 2:** This chapter presents the required background of magma dynamics followed by a derivation of the governing equations. The second part of this chapter gives a basic introduction to discontinuous Galerkin methods.

**Chapter 3:** This chapter presents the numerical discretization of the governing equations derived in Chapter 2, using DG methods and the robustness of this

discretization is quantified.

**Chapter 4:** This chapter gives the motivation for using local timestepping methods for magma dynamics followed by the details of the algorithm.

**Chapter 5:** This chapter presents the algorithmic details of projective pressure estimation, a numerical method developed to improve the computational time to solve coupled hyperbolic-elliptic equations, particularly magma dynamics problems in 2D and 3D, by exploiting temporal scale separation.

**Chapter 6:** 2D results obtained through the numerical simulations are presented along with a brief discussion of their physical significance.

**Chapter 7:** In this chapter, we characterize the shapes of dunite channels in 3D and discuss other significant results like dunite channels acting as pathways for melt migration.

**Chapter 8:** In this chapter other factors that influence dunite channel formation like melting, shearing and anisotropic permeability are briefly discussed.

**Chapter 9:** This chapter summarizes the results and the scope for extending this work to study the characteristics of melt migration. Potential applications of local timestepping methods and projective pressure estimation methods to other coupled hyperbolic-elliptic system of equations are discussed.

# Chapter 2

# Physical and Mathematical Background

## 2.1 Basics of Magma Dynamics

### 2.1.1 Fundamentals

Based on experimental and field observations, it is known that high-porosity channels are important pathways for melt migration in the mantle. There are various factors that affect melt migration such as temperature, pressure, solid deformation (e.g., shearing) etc. To better understand the assumptions for the physical model under consideration, the conceptual model is presented in Figure 2.1. As the plates are moving apart at the mid-ocean ridge axis, the mantle tries to move up because of the lower pressure that is created with the plate movement. At a depth of 80-120 km below the earth's surface, the temperature is equal to the solidus temperature, i.e., the temperature at which melting of the rock begins but the rock does not melt completely. The mantle does not melt at a greater depth even though the temperature is higher due to an increased pressure. The melt thus generated moves up and while some melt upwells in the vertical direction, there is also melt that shears

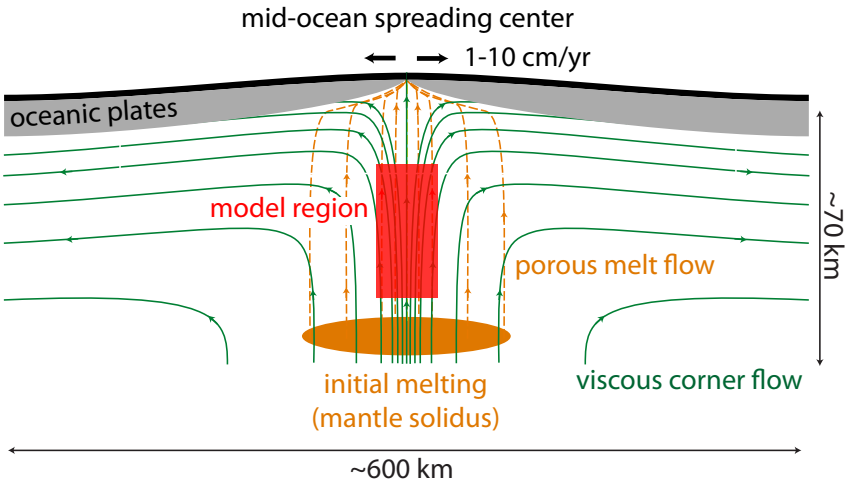


Figure 2.1: Conceptual model that is considered for the numerical simulations [27]. The rectangular region is the domain of interest.

because of the plates moving apart. The domain that is considered primarily in this thesis is marked by the rectangular region in the conceptual model. This region assumes that the flow is more or less vertical and that the effect of temperature is negligible in the process. Another important point to note is that the result of the simulations are assumed to be prior to the point where a corner flow is formed below the mid-ocean ridge. Thus, while the observed dunite channels are horizontal, the numerical study will result in the formation of vertical dunite channels as corner flow is not taken into account.

### 2.1.2 Concepts/Terminology

There are certain terms that repeatedly occur throughout this thesis and their definitions and significance are outlined in this section. For detailed description of these concepts, we refer [34].

**Porosity:** Porosity, $\phi_f$, is defined as the fraction of volume occupied by the melt or fluid in the solid matrix. The term is also termed as melt fraction.

**Solid Matrix:** It is composed of two minerals, a soluble mineral, opx, with a volume fraction denoted by $\phi_{opx}$ and an insoluble mineral, olivine, with a volume fraction denoted by $\phi_{ol}$.

**Compaction:** A negative compaction pressure implies that the stresses pull the grains of the solid matrix together while a positive compaction pressure implies that the grains are moving apart.

**Compaction Length:** A change in porosity causes a change or disturbance to the compaction pressure. The characteristic length-scale over which the disturbance decays back to the background compaction pressures is called the compaction length. In other words, it is the length-scale over which the disturbance interacts with the medium.

**Overturn Time:** The time for the solid at the bottom to advect all the way to the top of the domain.

### 2.1.3 Literature Review

Melt migration has been studied extensively through numerical, field observations and experimental studies. It has been observed that the major element composition of mid-ocean ridge basalt is not in chemical equilibrium with the residual mantle at low pressure. For this to occur, melts must rise from depths of at least 30 km in the asthenospheric mantle (ductilely-deforming region of the upper mantle) to the surface without extensive reequilibration with the surrounding mantle at shallow depth. Possible mechanisms that have been proposed to explain this include focused melt-flow through melt filled fractures, high-porosity melt channels or a combination

of these [35]. High-porosity channels and their corresponding relationship with dunite channels have been studied in detail by [42].

The formation of dunite channels in the mantle involves reactive dissolution when olivine normative basalts percolate through a partially molten harzburgite or lherzolite matrix. This results in preferential dissolution of pyroxene and precipitation of olivine which in turn increases local porosity and hence dunite permeability that accelerates melt flow and peridotite dissolution.

High-porosity channel formation with matrix deformation and reactive dissolution along a linear stability gradient was studied in [27, 2]. Stability diagram from [27] gives conditions that result in compaction-dissolution waves or high porosity channels. The stability diagram is shown in Figure 2.2. Results from linear stability analysis and numerical simulations show that elongated high-porosity melt channels develop spontaneously in the presence of a solubility gradient that is positive along the incoming melt flow direction. Further, in the presence of prescribed background melting, the formation of unstable dissolution channels becomes more difficult. The stabilizing effect of the matrix melting on melt localization was studied in [31] where it was shown that chemically uniform upwelling melting column, starting from its solidus, is stable relative to infinitesimal perturbation for the set of parameters explored in that study.

The detailed structure of melt channels and dunite channels and their spatial relationships in an upwelling mantle column was studied by [42, 52, 53]. To study the dunite channel distribution in these papers, opx abundance was explicitly tracked. These works further discuss important factors that affect the depth of dunite channels such as opx abundance in the initial mantle and the solubility gradient. These results were corroborated with a detailed linear stability analysis of reactive dissolution along a linear solubility gradient with a bulk viscosity that is inversely proportional to porosity [27].

This thesis builds on these recent studies by developing efficient and accurate

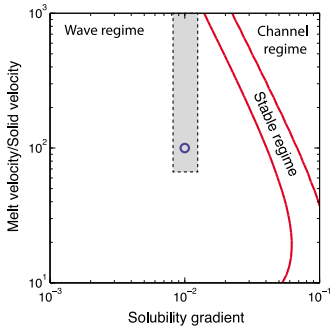


Figure 2.2: Stability diagram that defines the parameter regime for compaction-dissolution waves or high-porosity channels to occur. For details about the linear stability analysis, we refer to [27].

numerical models to study the detailed structure of high-porosity dissolution channels and compaction-dissolution waves in two and three dimensions, highlighting the implications of these results on the important characteristics of melt migration. In addition, dunite channel formation is extensively studied by extending or suitably modifying this formulation to model the following cases:

- Effect of variable viscosity.
- Simple cases of reverse solubility.
- Wave features with anisotropic permeability.
- Effect of shearing.
- Impact of melting.

### 2.1.4 Governing Equations

Following [53], we consider a binary system that consists of an interconnected melt network and a solid matrix comprised both of a soluble mineral, opx and an insoluble

mineral, olivine (ol). Let $\Gamma_{opx}$ be the dissolution rate of opx and $\Gamma_{ol}$ be the precipitation rate of ol in the melt, measured as the volume of mineral dissolved or precipitated per unit volume of the porous medium per unit time. Then $\Gamma_{ol} = -\beta\Gamma_{opx}$, where $\beta$ is the stoichiometric coefficient for opx dissolution. Mass conservation equations for the melt and the total solid are given by:

$$\frac{\partial \phi_f}{\partial t} + \nabla \cdot (\phi_f \mathbf{v}) = (1-\beta)\Gamma_{opx}, \tag{2.1}$$

$$\frac{\partial (1-\phi_f)}{\partial t} + \nabla \cdot [(1-\phi_f)\mathbf{V}] = -(1-\beta)\Gamma_{opx}, \tag{2.2}$$

where $\mathbf{v}$ and $\mathbf{V}$ are melt and solid velocities, respectively. Conservation of soluble mineral, opx, in the solid matrix is given by

$$\frac{\partial \phi_{opx}}{\partial t} + \nabla \cdot (\phi_{opx} \mathbf{v}) = -\Gamma_{opx}, \tag{2.3}$$

The volume fraction of olivine is derived from the volume fractions of $\phi_{opx}$ and $\phi_f$ as

$$\phi_{ol} = 1 - \phi_{opx} - \phi_f, \tag{2.4}$$

Equations (2.1)-(2.3) are derived using the Boussinesq approximation i.e., that the densities of the melt and the solid are the same and that the velocity of opx and ol is the same as the bulk solid velocity. Neglecting diffusion and dispersion in the melt and assuming constant and uniform mineral compositions, mass conservation equation for the independent component in the melt for the effective binary system is given by :

$$\frac{\partial (\phi_f c_f)}{\partial t} + \nabla \cdot (\phi_f \mathbf{v} c_f) = (c^0_{opx} - \beta c^0_{ol})\Gamma_{opx}, \tag{2.5}$$

where $c_f$, $c^0_{opx}$ and $c^0_{ol}$ are concentrations of the independent component in the melt, opx and ol, respectively.

Mass transfer can be modelled by the first-order kinetic approximation [60, 2, 59]

$$\Gamma_{opx} = \alpha_r \phi_f \phi_{opx} c_f^{eq}(\mathbf{x}) - c_f, \qquad 0 < \alpha_r < \infty, \tag{2.6}$$

where coefficient of proportionality $\alpha_r$ is a rate constant. For the effective binary system considered in this study, the equilibrium concentration, $c_f^{eq}$ varies only as a function of the vertical coordinate if the effect of temperature is small compared to that of pressure.

$$c_f^{eq}(\mathbf{x}) = c_f^{eq}(z) = c_f^0 + \Delta c F(z/L), \tag{2.7}$$

At the lower boundary of our domain the solubility takes the value $c_f = c_f^0$, and $\Delta c$ is the change in solubility over a compaction length $L$. In the limit $\alpha_r \to \infty$, concentration tends to equilibrium value and the dissolution rate is obtained by combining equations (2.1) and (2.5) with $c_f = c_f^{eq}$:

$$\Gamma_{opx} = \frac{\phi_f(\mathbf{v} \cdot \mathbf{n_z})\partial c_f^{eq}/\partial z}{c_{opx}^0 - \beta c_{ol}^0 - (1-\beta)c_f^{eq}} \mathcal{I}_{opx}, \tag{2.8}$$

In the equilibrium limit, the opx dissolution rate is proportional to the vertical melt flux and solubility gradient and is independent of opx abundance.

Darcy's law, relating relative melt flux to gradients of an effective pressure and melt buoyancy is used to determine the velocities, $\mathbf{v}$ and $\mathbf{V}$,

$$\phi_f(\mathbf{v} - \mathbf{V}) = -\frac{\kappa_\phi}{\mu}[\nabla p - \Delta\rho g \boldsymbol{n}_z], \tag{2.9}$$

where $\kappa_\phi$ is the permeability, $\mu$ is the viscosity of the melt, $p = p_f - p_s$ is the pressure difference between the melt ($p_f$) and the solid ($p_s$), $\Delta\rho = \rho_s - \rho_f$ is the density difference between the solid ($\rho_s$) and the melt ($\rho_f$), $g$ is the acceleration due to gravity, and $\boldsymbol{n}_z$ is the unit vector, positive upward. The permeability depends on

porosity through the power-law relation,

$$\kappa_\phi = \kappa_0 \left( \frac{\phi_f}{\phi_f^0} \right)^n, \tag{2.10}$$

where $\kappa_0$ is the permeability at the reference melt fraction $\phi_f^0$ and $n = 3$ in the present study. The pressure difference between the melt and the solid is related to the compaction rate of the matrix ($\nabla \cdot \boldsymbol{V}$) through the bulk velocity $\xi$,

$$p = p_f - p_s = \xi \nabla \cdot \mathbf{V}, \tag{2.11}$$

$$\xi = \frac{\eta}{\phi_f}, \tag{2.12}$$

where $\eta$ is the shear viscosity of the solid matrix. The effective pressure can be solved from a Helmholtz equation obtained by combining (2.1) and (2.2) and the divergence of (2.9),

$$\nabla \cdot [\frac{\kappa_\phi}{\mu}(\nabla p - \Delta \rho g \boldsymbol{n}_z)] = \frac{\phi_f p}{\eta}. \tag{2.13}$$

Eq. (2.2) can also be written in terms of the effective pressure,

$$\frac{\partial \phi_f}{\partial t} + \mathbf{V} \cdot \nabla \phi_f = (1 - \phi_f)\frac{\phi_f p}{\eta} + (1 - \beta)\Gamma_{opx}, \tag{2.14}$$

To derive the working model used in this study, we non-dimensionalize (2.1)-(2.14) with the following substitutions:

$$t = t^0 t', \qquad \boldsymbol{x} = L\boldsymbol{x}', \qquad \phi_f = \phi_f^0 \phi_f', \qquad \phi_{opx} = \phi_{opx}^0 \phi_{opx}',$$

$$c_f = c_f^0 + \Delta c c_f', \qquad p = p^0 p', \qquad \boldsymbol{v} = w_0 \boldsymbol{v}', \qquad \boldsymbol{V} = W_0 \boldsymbol{n}_z + \Delta V \boldsymbol{V}', \tag{2.15}$$

The time, length, pressure and velocity scales are

$$t^0 = \frac{L}{W^0}, \qquad L = \sqrt{\frac{\kappa_0 \eta}{\mu \phi_f^0}}, \qquad p^0 = \frac{\eta W_0}{L},$$

$$w_0 = \frac{\kappa_0 \Delta \rho g}{\phi_f^0 \mu}, \qquad \Delta V = \frac{\phi_f^0 w_0 (1-\beta)\Delta c}{c_{opx}^0 - \beta c_{ol}^0 - (1-\beta)c_f^0}, \tag{2.16}$$

where $L$ is the compaction length [43] and the timescale $t^0$ is the time needed for a matrix panel to advect a compaction length via solid upwelling. Substituting (2.15) and (2.16) into (2.3), (2.5),(2.9), (2.13) and (2.14) and after dropping the primes for clarity, we have the dimensionless equations.

$$\frac{\partial \phi_f}{\partial t} = -\frac{\partial \phi_f}{\partial z} + \phi_f p + \delta \Gamma_{opx} \tag{2.17}$$

The three right-hand-side terms of Eq. (2.17) represent upwelling, compaction, and dissolution, respectively. Upwelling is the gradual rise of the earth's mantle in the positive z (upwards) direction, compaction is the rate of relative volume change of the solid matrix and dissolution is the process by which opx is converted to melt. Together the three processes effectively form an advection-reaction type equation. Eq. (2.17) contains the dimensionless parameters $\delta$, representing the solubility gradient of the equilibrium concentration of the soluble mineral in the fluid.

Similarly, the evolution of opx abundance is described by the conservation law,

$$\frac{\partial \phi_{opx}}{\partial t} = -\frac{\partial \phi_{opx}}{\partial z} - \frac{\phi_f^0}{\phi_{opx}^0} \frac{\delta}{(1-\beta)} \Gamma_{opx} \tag{2.18}$$

In both the conservation equations, $\Gamma_{opx}$ represents the rate at which opx is consumed in the dissolution process. Hence, the dissolution term in Eq. (2.18) carries an opposite sign to Eq. (2.17); the former represents depletion of opx whereas the latter represents generation of melt.

Finally, under the assumption of local chemical equilibrium, the melt composition

is completely determined by the solubility curve for the effective binary system. The dissolution rate, $\Gamma_{opx}$, then is proportional to the Darcy flux, $\phi_f \mathbf{v}$, and is computed algebraically as

$$\Gamma_{opx} = R\frac{\phi_f(\mathbf{v}.\mathbf{n}_z)}{1-\delta z}\mathcal{I}_{opx} \tag{2.19}$$

where the indicator function $\mathcal{I}_{opx}$ returns 1 if $\phi_{opx}$ is positive and zero otherwise [53]. In this way, dissolution occurs only if the soluble mineral opx is present.

$$-\nabla.[\phi_f^3\nabla p] + \phi_f p = -R\frac{\partial \phi_f^3}{\partial z} \tag{2.20}$$

$$\phi_f \mathbf{v} = R^{-1}\phi \mathbf{n}_z - \phi_f^3(R^{-1}\nabla p - \mathbf{n}_z) \tag{2.21}$$

Equations (2.17)-(2.21) have four dimensionless parameters,

$$\frac{\phi_f^0}{\phi_{opx}^0},\ \delta = (1-\beta)\frac{\Delta c}{\hat{c}},\ Da = \frac{\alpha \hat{c} L \phi_{opx}^0}{w_0},\ R = \frac{w_0}{W_0} \tag{2.22}$$

The physical values and short definitions of the parameters and the symbols used in this text are defined in the nomenclature section.

## 2.2 Discontinuous Galerkin Methods

From a computational perspective, previous numerical studies utilizing a low-order finite difference scheme were presented in [59], and demonstrated the localization of the melt flow into high porosity channels. However, this work does not explicitly account for the soluble mineral opx, whose presence is essential to the formation of dunite channels, nor does it consider the effects of upwelling. Further numerical studies incorporating upwelling of the mantle were presented in [58], although this work does not discuss the specifics of the numerical model used. In [52], a high-order accurate numerical model was developed based on the physical models presented in [27, 53], which include upwelling, a porosity-dependent bulk viscosity, and an

additional equation to track the opx abundance. [52] also assumes a formulation of local chemical equilibrium with negligible diffusion in the melt. Linear stability analysis of this system predicts the emergence of compaction-dissolution waves [27]. In addition to the channeling instability, these features present a formidable challenge for numerical modeling. This challenge was previously addressed by developing a high-order numerical method that provides accurate resolution at a reasonable cost. This was achieved by using a high-order discretization consisting of a tensor product of the Fourier collocation [52] or a high-order finite difference scheme [41] in the horizontal direction and discontinuous Galerkin methods in the vertical direction.

However, all previous work employed a two-dimensional model and an extension to the three dimensional problem would require a substantial effort. Rather than attempting this approach, we explore the use of existing libraries and, in particular, the software library called deal.II, offering multiple options such as high-order elements, support for adaptivity and the flexibility of expressing the problem in a dimension independent way [6]. The main objective of the present work is to develop an efficient and accurate numerical model that can be used to study the interaction between the melt and solid mantle during melt migration in both 2D and 3D using discontinuous Galerkin methods. Following [52] we explicitly track the evolution of the soluble mineral (opx) to understand the formation of the observed opx-depletions and their spatial and temporal relation to localized melt flow in regions of high permeability. We evolve the governing system by solving the pressure equation using the current porosity values, and then evolve porosity and opx.

### 2.2.1 History

Discontinuous Galerkin (DG) methods, as stated in the introduction, inherently satisfy the requirements of high order accuracy with geometric flexibility through local approximation like finite element methods. The stability requirements are satisfied by incorporating the features of finite volume methods for transport problems. DG

methods are a class of finite element methods which use completely discontinuous basis functions. DG method was first proposed to solve the steady-state neutron transport equation by [45], the rigorous mathematical framework of DG methods for time-dependent problems was carried out by Cockburn and coworkers in a series of papers [21, 19, 18, 17, 16, 20]. There are several advantages of the DG methods making them attractive for applications of the type considered here. These include their ability for easy handling of complicated geometry and boundary conditions (an advantage shared by finite element methods), their flexibility for easy h-p adaptivity (splitting elements in space or increasing the polynomial degree) including changes of approximation orders between neighboring elements and allowing general meshes with hanging nodes and their compactness (evolution of an element depends only on information from immediate neighbors) hence allowing an efficient parallel implementation. These properties have led to a rapid spread into a wide range of computational problems in aeroacoustics [47], electro-magnetism [28], gas dynamics [22] and modeling of shallow water [25] among many others.

### 2.2.2 Motivation

Since DG combines the attractive features of both FE and FV methods, it is ideally suited for conservation laws and advection-reaction type equations as required in the case of conservation equations in magma dynamics. Since the solution can be discontinuous across cell interfaces, it decouples the global solution into local ones in contrast to FE methods. However, one problem with high-order methods including DG is that in the presence of strong discontinuities, the numerical solution will contain non-physical oscillations. This is also true when sharp gradients are introduced from the nonlinearity of the equations as is the case of the conservation equation of porosity (2.17). There are various techniques to resolve this like slope limiters, filters and adding an artificial viscosity term. In this project, artificial entropy viscosity is used to dissipate the numerical oscillations. The details of this method will be

discussed in the next chapter.

### 2.2.3 Basic Formulation

In this section, we present the basic formulation of discontinuous Galerkin methods for scalar conservation laws. The general form of a scalar conservation law is given as

$$\begin{aligned} \frac{\partial u(\boldsymbol{x},t)}{\partial t} + \nabla \cdot \boldsymbol{f}((u(\boldsymbol{x},t),\boldsymbol{x},t) = 0,\ \boldsymbol{x} \in \Omega \subset \Re^n \\ u\left(\boldsymbol{x},t\right) = g\left(\boldsymbol{x},t\right),\ \boldsymbol{x} \in \partial\Omega \\ u\left(\boldsymbol{x},0\right) = u_0(\boldsymbol{x}),\ \boldsymbol{x} \in \Omega \end{aligned} \tag{2.23}$$

where the flux $\boldsymbol{f}$ is given and it is assumed that the boundary conditions are available at all inflow points such that the PDE is well-posed.

The domain $\Omega$ is triangulated into K non-overlapping elements such that

$$\Omega \simeq \Omega_h = \bigcup\nolimits_{k=1}^{K} D^k \tag{2.24}$$

The function space $V_h$ is defined as element wise discontinuous polynomials of degree $N$ such that

$$V_h = \{v_h \in L^2(\Omega) : v_h|_k \in P^N(k) : \forall k \in \Omega_h\} \tag{2.25}$$

where $v_h$ is the multidimensional Legendre polynomial in the element $k$, $L^2$ is the space of square integrable functions and $P^N$ is the polynomial space of degree N chosen according to the required order of accuracy. We look for the numerical solution $u_h$, of the form

$$u(\boldsymbol{x},t) \simeq u_h(\boldsymbol{x},t) = \sum_{k=1}^{K} u_h^k(\boldsymbol{x},t) \in V_h \tag{2.26}$$

The local function, $u_h^k(\boldsymbol{x},t)$, is defined using a multidimensional Lagrange polyno-

mial, $l_i(\boldsymbol{x})$ which is based on the grid points, $\boldsymbol{x}_i$ or Legendre polynomial $\psi_i(\boldsymbol{x})$ as,

$$u_h^k(\boldsymbol{x},t) = \sum_{i=1}^{N_p} u_h^k(\boldsymbol{x}_i,t)\boldsymbol{l}_i(\boldsymbol{x}) = \sum_{i=1}^{N_p} \hat{u}_n(t)\psi_i(\boldsymbol{x}) \tag{2.27}$$

where $N_p$ are the number of terms in the local expansion. Taking the Lagrange basis for the discretization, we get the following weak form by multiplying Eq. (2.23) with a test function $l_m(\boldsymbol{x})$, and integrating by parts

$$\forall k,m : \int_D^k \left[\frac{\partial u_h^k}{\partial t}\boldsymbol{l}_m(\boldsymbol{x}) - \boldsymbol{f}_h \cdot \nabla l_m(\boldsymbol{x})\right] d\boldsymbol{x} = -\oint_\partial D^k \hat{\boldsymbol{n}}.\boldsymbol{f}^* l_m(\boldsymbol{x}) d\boldsymbol{x}, \tag{2.28}$$

Integrating by parts again, we get the following strong form:

$$\forall k,m : \int_D^k \left[\frac{\partial u_h^k}{\partial t}\boldsymbol{l}_m(\boldsymbol{x}) + \nabla \cdot \boldsymbol{f}_h l_m(\boldsymbol{x})\right] d\boldsymbol{x} = \oint_\partial D^k \hat{\boldsymbol{n}}.[\boldsymbol{f}_h - \boldsymbol{f}^*] l_m(\boldsymbol{x}) d\boldsymbol{x} \tag{2.29}$$

The two forms are mathematically equivalent but differ in implementation. Since the numerical solution $u_h^k$ is discontinuous across element boundaries $\partial D^k$, a numerical flux, $\boldsymbol{f}^*(u_h^{k^-}, u_h^{k^+})$, needs to be defined where $u_h^{k^-}$ and $u_h^{k^+}$ are the solutions in the element and its neighbor, respectively. This numerical flux depends on values of the solution on either side of the element boundary such that stability of the solution is ensured. This also couples the local solutions and hence allows for a global transfer of information. In general, the numerical flux $\boldsymbol{f}^*(a,b)$ must satisfy the following three properties:

1. $\boldsymbol{f}^*$ is Lipschitz continuous with respect to both arguments.

2. $\boldsymbol{f}^*$ is nondecreasing with respect to its first argument and nonincreasing with respect to its second argument.

3. $\boldsymbol{f}^*$ is consistent with the original flux $\boldsymbol{f}$ , that is, $\boldsymbol{f}^*(a,a) = \boldsymbol{f}(a)$.

While there are many numerical flux functions that satisfy the above three conditions,

the easiest and the most stable choice is the Lax-Friedrich flux

$$\boldsymbol{f}^*(a,b) = \frac{\boldsymbol{f}(a)+\boldsymbol{f}(b)}{2} + \frac{C}{2}\hat{\boldsymbol{n}}(a-b), \tag{2.30}$$

where $C$ is the local maximum of the directional flux Jacobian, i.e.,

$$C = \max_{u\in[a,b]} \left| \hat{\boldsymbol{n}} \cdot \frac{\partial \boldsymbol{f}}{\partial u} \right| \tag{2.31}$$

### 2.2.4 Time Integration

The spatial discretization using DG methods reduces the PDEs to a system of ordinary differential equations. The resulting semi-discrete scheme is of the form

$$\frac{du_h}{dt} = \mathcal{L}_h(u_h, t) \tag{2.32}$$

for some operator $\mathcal{L}_h$. The resulting system is then solved using a time integration scheme. There are two classes of time integration techniques, multi-stage methods and multi-step methods. In this section, explicit Runge-Kutta methods from the class of multi-stage methods are presented. Multi-step methods and their advantages are discussed in Chapter 5.

$$\begin{aligned} v^{(0)} &= u_h^n \\ v^{(i)} &= \sum_{k=0}^{i-1} \left( \alpha_{i,k} v^{(k)} + \Delta t \beta_{i,k} \mathcal{L}_h \left( v^{(k)}, t^n + \Delta t^{(k)} \right) \right), \qquad i = 1, ..., m, \\ v^{(m)} &= u_h^{n+1}. \end{aligned} \tag{2.33}$$

These are the standard Explicit Runge-Kutta (ERK) methods for time integration but the drawback of these methods is that the solution needs to be stored for every intermediate stage. An alternative to the fourth order scheme is the low-storage

version called the Low-Storage Explicit Runge-Kutta (LSERK) method,

$$
\begin{aligned}
& p^{(0)} = u_h^n, \\
& i \in [1, ..., 5] : \begin{cases} v^{(i)} &= a_i v^{(i-1)} + \Delta t \mathcal{L}_h \left( p^{(i-1)}, t^n + c_i \Delta t \right), \\ p^{(i)} &= p^{(i-1)} + b_i v^{(i)} \end{cases} \\
& u_h^{n+1} = p^{(5)}
\end{aligned}
\tag{2.34}
$$

which is also fourth order but it requires five stages of computation. Even though LSERK method requires one extra stage, it is compensated by the larger stable time step as compared to fourth order Runge-Kutta method [12].

## 2.3 Accuracy

In this section, the theoretical error estimates for DG methods are discussed. In one dimensional problems, if the solution to (2.23) is smooth, then the optimal $L^2$ error estimate for the general nonlinear conservation law for the fully discretized RKDG methods is given by

$$||u - u_h|| \leq C h^{N+1} \tag{2.35}$$

where $C$ depends on $u$ and its derivatives but is independent of $h$ [63]. For multi-dimensions, the optimal error estimate given in (2.35), can be proved for tensor products and basis functions and for certain specific triangulations when the usual piece-wise $N^{th}$ degree polynomial approximations are used [48, 15]. However, $L^2$ error estimate for the most general cases is half an order lower and given by $O(h^{N+\frac{1}{2}})$ [32].

## 2.4 Conclusion

This chapter introduced the foundations required to understand the magma upwelling process as well as the numerical schemes that will be developed in the later chapters to solve the governing set of equations for magma dynamics. Time integra-

tion methods were also introduced. These methods will be compared with multi-step methods in Chapter 5. For further information on discontinuous Galerkin methods, we refer to [30, 55].

# Chapter 3

# Numerical Scheme

To solve the system (2.17)-(2.21), we employ a discontinuous Galerkin (DG) scheme for the hyperbolic equations, (2.17), (2.18) and an interior penalty discontinuous Galerkin (IPDG) method for the elliptic equation (2.20). The rationale behind these choices is as follows. For the advection equations, DG methods are well suited for conservation laws and are robust and fast due to locality. IPDG methods were used for the elliptic equation as they are easily parallelizable and require very little storage compared to other DG methods by using a wider stencil through the flux. Complete details of the implementation of this method are given in [49]. Proceeding by a method-of-lines approach, the spatial operations in the hyperbolic equations (2.17)-(2.18) are discretized to produce a system of differential-algebraic equations that are a function of time only and can be integrated with a LSERK method.

## 3.1 Discretization

The domain $\Omega$ is triangulated into K non-overlapping elements such that

$$\Omega \simeq \Omega_h = \bigcup_{k=1}^{K} D^k \tag{3.1}$$

The function space $V_h$ is defined as elementwise discontinuous polynomials of degree $N$ such that

$$V_h = \{v_h \in L^2(\Omega) : v_h|_k \in P^N(k) : \forall k \in \Omega_h\}, \tag{3.2}$$

where $v_h$ is the multidimensional Legendre polynomial in the element $k$, $L^2$ is the space of square integrable functions and $P^N$ is the polynomial space of degree N in the element. We seek solutions $\phi_{f_h}$ , $\phi_{opx_h}$ in this function space. Following the procedure in [30], the discretized form of the porosity evolution equation (2.17) is

$$\begin{aligned} \int_{D^k} v_h \partial_t \phi^k_{f_h} d\mathbf{x} - \int_{D^k} \phi^k_{f_h} \mathbf{n}_z . \nabla v_h d\mathbf{x} = \\ - \oint_{\partial D^k} v_h (\phi^k_{f_h})^* \mathbf{n}_e . \mathbf{n}_z d\mathbf{x} + \int_{D^k} v_h p \phi^k_{f_h} d\mathbf{x} + \int_{D^k} \delta v_h \Gamma^k_{opx_h} d\mathbf{x}, \end{aligned} \tag{3.3}$$

where $\mathbf{n}_e$ is the outward pointing normal to the cell face $\partial D^k$. We choose an upwinding flux as

$$\begin{aligned} \phi^{k,*}_f(\phi^{k,-}_f, \phi^{k,+}_f) &= \phi^{k,-}_f, \ \mathbf{n}_z . \mathbf{n}_e \geq 0 \\ &= \phi^{k,+}_f, \ \mathbf{n}_z . \mathbf{n}_e \leq 0, \end{aligned} \tag{3.4}$$

The opx evolution equation is discretized in a similar fashion

$$\begin{aligned} \int_{D^k} v_h \partial_t \phi^k_{opx_h} d\mathbf{x} - \int_{D^k} \phi^k_{opx_h} \mathbf{n}_z . \nabla v_h d\mathbf{x} = \\ - \oint_{\partial D^k} v_h (\phi^k_{opx_h})^* \mathbf{n}_e . \mathbf{n}_z d\mathbf{x} - \int_{D^k} \frac{\phi^0_f}{\phi^0_{opx}} \frac{\delta}{(1-\beta)} v_h \Gamma^k_{opx_h} d\mathbf{x}, \end{aligned} \tag{3.5}$$

Lastly, the elliptic equation is a modified Helmholtz equation and this is discretized using interior penalty discontinuous Galerkin Method (IPDG). Following [30], dis-

cretization for the pressure equation becomes,

$$\sum_{k\in\Omega_h}\int_k \phi_f^3\nabla p.\nabla v + \int_\Omega \phi_f p v + \epsilon\sum_{e\in\partial D_{in}\cup\partial\Omega_d}\int_e\{\phi_f^3\nabla v.\mathbf{n}_e\}[p] - \sum_{e\in\partial D_{in}\cup\partial\Omega_d}\int_e\{\phi_f^3\nabla p.\mathbf{n}_e\}[v] + \sigma\sum_{e\in\partial D_{in}\cup\partial\Omega_d}\int_e[p][v] = \int_\Omega -R\frac{\partial\phi_f^3}{\partial z}v + \sum_{e\in\partial\Omega_d}\int_e(\epsilon\phi_f^3\nabla v.\mathbf{n}_e + \sigma_e v)g_D, \tag{3.6}$$

Here $\epsilon$ is a parameter which can take the values $\{-1, 0, 1\}$ and $\sigma_e$ is a penalty parameter that penalizes the jump in the function values across the cell face. As a solver, we use a matrix-free implementation of the biconjugate gradient stabilized (BiCGStab) iterative method with a block Jacobi preconditioner for the elliptic equation [50].

## 3.2 Numerical Validation

To verify the convergence of the DG scheme we follow the approach of [52] by taking the same parameter and domain setup. We take a domain of size $(x, z) \in [0, 1]\times[0, 2]$ and the non-dimensional parameters are given by $R = 100$, $\delta = 0.01$ and $\eta = \frac{\phi_f^0}{\phi_{opx}^0(1-\beta)} = 0.266$. We assume exact, steady solutions for porosity and pressure as

$$\phi_{f_e}(x, z, t) = \exp(0.04z)(1 + 0.1\cos(2\pi x)), \tag{3.7}$$

$$p_e(x, z, t) = p_0 + 0.1\cos(2\pi(x))z\sin(0.75\pi z)). \tag{3.8}$$

Substituting these exact solutions into (2.17) and (2.20) yields a residual for each equation that is in turn added back to the equations, guaranteeing a prescribed exact solution. We integrate this system to steady state with very small time steps. From general analysis of the DG method [29] we expect the error of the scheme to diminish as a power of the size of the element $h$. This is confirmed in Figure 3.1, where we

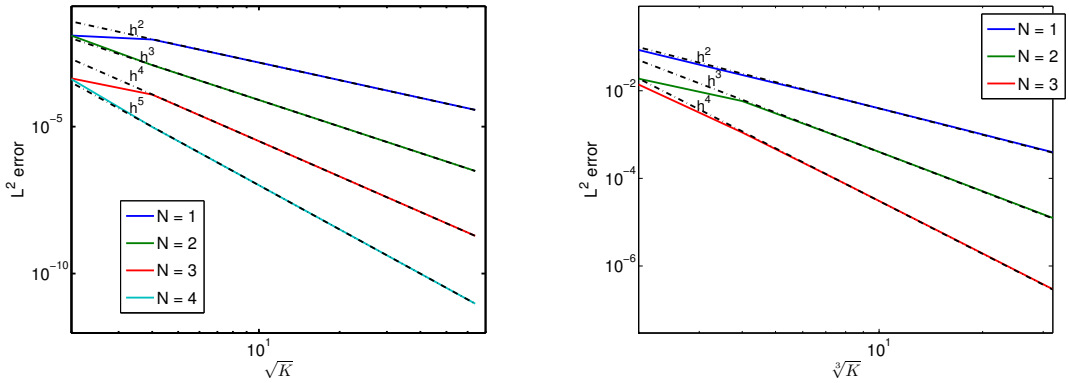


Figure 3.1: Convergence study. Error analysis with the manufactured solutions discussed in section 3.2 using $P^1$, $P^2$ and $P^3$ elements respectively. The dashed line represents the optimal convergence rates, $h^{N+1}$. The solid line is the computed error which also converges optimally. Here, $h = K^{(\frac{-1}{dim})}$ where $K$ is the number of elements and $dim$ is the dimension of the problem.

observe that the $L^2$-error decays as $h^{(N+1)}$ where $N$ is the degree of polynomial and $h$ is the diameter of the cell.

## 3.3 Handling Numerical Oscillations

The basic DG formulation suffices to solve the governing set of equations when there are no steep gradients of porosity as is generally true in the channel regime. But in the wave regime, the random variation of porosity combined with the source term, $\Gamma_{opx}$, which scales with $z_{max}$, results in numerical oscillations. There are many methods that can be used to ensure that these spurious oscillations are controlled with three standard procedures being:

1. **Filters:** Filtering is the easiest way to control the oscillations and is performed by damping the high modes and leaving the low modes unchanged. Consider

a simple advection equation,

$$\frac{\partial u_h}{\partial t} + \frac{\partial f(u_h)}{\partial x} = 0. \tag{3.9}$$

Filtering can be considered equivalent to adding a dissipation term $\epsilon(-1)^{\bar{s}-1}[\frac{\partial}{\partial x}(1-x^2)\frac{\partial}{\partial x}]^{\bar{s}}u_h$ to the advection equation given in (3.9). The effect of this dissipative term can also be achieved by considering the modified form of the solution as:

$$u_h^F(x,t) = \sum \sigma(n/N)\hat{u}_n(t)\tilde{P}_n(x), \tag{3.10}$$

where $\sigma(n/N)$ is a filter function. However, filtering may not work for all the problems e.g. there are situations where shocks cannot be controlled by filters except if the solution is completely damped, with the result that the physical characteristics of the problem are inaccurate. For this reason, filters were not employed in this work while solving the porosity equation. For more information on filter functions and their properties, we refer to [30].

2. **Limiters:** Limiters work by limiting the spatial derivatives to control oscillations. The essence of limiters comes from finite volume schemes and limiters that work well for finite volume schemes have been extended to DG methods as well with similar success. See [21, 19, 18, 17, 10, 39] and references therein. Some recent work employs WENO limiters directly in a DG setting [64]. Let $\phi_f^n$ be the solution at time step $n$ and $\phi_f^{n,l}$ be the solution after the limiter is applied. The limited solution should maintain the cell average to satisfy the conservation property. Following the procedure in [20], TVB limiters can be applied to $\phi_f^n$. The limiting procedure is applied on the first derivatives, $\phi_{f_x}$ and $\phi_{f_z}$ using the cell averages of the cell and its neighbors by defining a function: $\bar{m}(\phi_{f_x}, \bar{\phi}_{f_{i+1,j}} - \bar{\phi}_{f_{i,j}}, \bar{\phi}_{f_{i,j}} - \bar{\phi}_{f_{i-1,j}})$ where $\bar{m}$ is the TVB minmod

function defined as

$$\bar{m}(a_1, a_2, ...a_m) = \begin{cases} a_1, & \text{if } |a_1| \leq M\Delta x^2 \\ m(a_1, a_2, ...a_m), & \text{otherwise,} \end{cases} \tag{3.11}$$

where the minmod function $m$ is defined by

$$m(a_1, a_2, ...a_m) = \begin{cases} s \min_i |a_i|, & \text{if } s = sign(a_1) = ... = sign(a_m) \\ 0, & \text{otherwise.} \end{cases} \tag{3.12}$$

Here $M$ is a tunable parameter that is problem dependent. This is to make sure that the limiter does not engage near smooth extrema. $\phi_{f_z}$ is limited similarly by applying the minmod function as: $\bar{m}(\phi_{f_z}, \bar{\phi}_{f_{i,j+1}} - \bar{\phi}_{f_{i,j}}, \bar{\phi}_{f_{i,j}} - \bar{\phi}_{f_{i,j-1}})$ These methods, although successful, have a couple of drawbacks. The limiting procedure involves a lot of post-processing of the solutions and hence increases cost. The other disadvantage is that all the higher order terms are set to zero if the limiter changes the first derivative, thus reducing the accuracy of the solution. To capture all the essential characteristics of the physical process, the mesh needs to be highly refined and this again induces cost, especially when solving the problems in 3D. Figure 3.2 illustrates that, while the limiter controls the oscillations for the four chosen values of $M$, the wave pattern is completely diffused for $M = 0, 1$.

3. **Artificial diffusion:** The oscillations can also be controlled by adding an artificial viscosity. Such methods come with the drawbacks of spatially discretizing one more operator for the governing equation and also limiting the time step because of the diffusive term. But the simplicity and robustness of implementing these methods makes them an attractive method to implement.

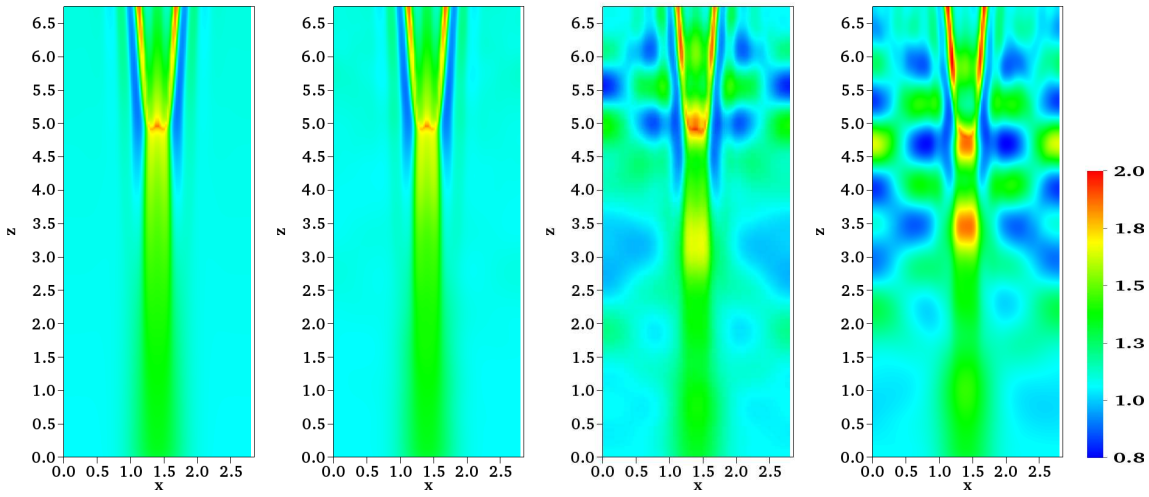


Figure 3.2: Porosity distribution with TVB limiters for various choices of M. From left to right $\{M = 0, 1, 10, 20\}$ with $3^{rd}$ order DG methods and $40,000$ cells.

Although the viscosity term can be applied throughout the domain, this will result in a problem that is similar to that observed in applying filters. Therefore, the additional viscosity term must primarily act in regions of numerical oscillations and be small in regions where the porosity variation is smooth. We consider the entropy viscosity proposed by [65], which is based on the residual of the governing equations. The artificial viscosity is a piecewise constant function defined by:

$$\nu|_k = \alpha \min\{c_{max} h_k, c_E h_k^2 \max(D_1(\phi_h))\}, \tag{3.13}$$

where $\alpha$ is a stabilization constant that is tweaked to scale the artificial viscosity according to the requirements of the problem. The second term $D_1(\phi_h)$ is defined as:

$$D_1(\phi_h) := \max(\max_{x \in k} |Re_i(\phi_h)|, \max_{x \in \partial k} |J_i(\phi_h)|)/N_h, \tag{3.14}$$

With the individual terms in the definition of $D_1(\phi_h)$ given as:

$$Re_i(\phi_h) := \frac{\phi_f^n - \phi_f^{n-1}}{\Delta t^n} + \partial_z \phi_f^{(a)} - p^{(a)}\phi_f^{(a)} - \Gamma_{opx}^{(a)}, \tag{3.15}$$

where the superscript $(a)$ indicates the average of the function at $n$ and $n+1$

$$J_i(\phi_h) := [\![\phi_f^{(a)}]\!], \tag{3.16}$$

$$N_h(\phi_h) := \text{var}(\phi_f^{n+1}) = \max_{\Omega} \phi_f^{n+1} - \min_{\Omega} \phi_f^{n+1}. \tag{3.17}$$

Intuitively, the change in residuals $Re_i$ and the jump terms $J_i$ defined as the difference in the value of the porosity across faces of a cell with respect to the total variation in porosity $N_h$, determine the amount of artificial viscosity to be used in the cell. Implementation and performance of this scheme are discussed in detail in [65, 14].

The weak form of the porosity equation with the artificial viscosity term is given as:

$$\begin{aligned}\sum_K (\frac{d\phi_f}{dt}, v) = \sum_K ((\phi_f^n)\boldsymbol{\eta}, \nabla v)_K - ((\phi_f^n)(\mathbf{n}\cdot\boldsymbol{\eta}), v)_{\partial K} \\ + \sum_K (\phi_f^n p^n + \Gamma_{opx}^n, v)_K \\ - \sum_K \int_k \nu \nabla \phi_f^n . \nabla v + \epsilon \sum_{e \in \partial D_{in} \cup \partial \Omega_d} \int_e \{\nu \nabla v . \mathbf{n}_e\}[\phi_f^n] \\ - \sum_{e \in \partial D_{in} \cup \partial \Omega_d} \int_e \{\nu \nabla \phi_f^n . \mathbf{n}_e\}[v] + \sigma \sum_{e \in \partial D_{in} \cup \partial \Omega_d} \int_e [\phi_f^n][v] \\ + \sum_{e \in \partial \Omega_d} \int_e (\epsilon \nu \nabla v . \mathbf{n}_e + \sigma_e v) g_D.\end{aligned} \tag{3.18}$$

Here $\boldsymbol{\eta} = (0, 1)$ is the vector field notation that results in the advection of melt in the z direction in (2.17). The diffusion term is discretized using an IPDG method similar to the pressure equation. This results in the last 5 terms on the right hand side in the weak form of the extra diffusion term in (3.18). The parameters $\epsilon$ and

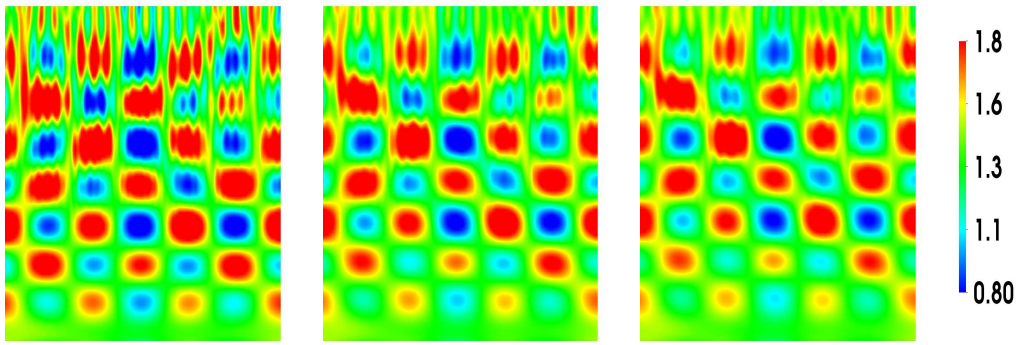


Figure 3.3: Porosity at $t = 10.0$ with 4th order DG elements with 3600 cells and random inflow perturbation with different stabilization constants $\alpha$. From left to right, $\alpha = \{0.3, 0.5, 0.6\}$. Computational domain is $(x, z) \in [0, 5.7] \times [0, 6.75]$.

$\sigma_e$ are the same as given for the discretization of the pressure equation and $\nu$ is the artificial viscosity added to control the numerical oscillations. This equation also results in two boundary integral terms. The periodic boundary conditions and the Dirichlet boundary conditions need to be taken into account for the diffusion term as well. The Neumann term is taken to be zero as we require only Dirichlet boundary conditions to be satisfied for the original set of governing equations.

Figure 3.3 shows a comparison between the porosity solutions at $t = 10$, for viscosity parameters $\alpha = 0.3, 0.5, 0.6$ respectively. The physical significance of these results will be discussed later. As can be seen from the plots, as the viscosity parameter, $\alpha$, increases, the dissipation increases and the waves are not as strong. The stabilization constant used throughout this thesis for wave regime computations is $\alpha = 0.15$, unless specified otherwise.

## 3.4 Adaptivity

The characteristics of dunite channels reflect in only a small region in the whole domain. While DG methods with a uniform mesh work perfectly to study the characteristics of melt migration, it gets computationally prohibitive to have a mesh

uniformly refined to study the boundary effects of dunite channels since it requires a highly refined mesh at the dunite boundary. Adaptive mesh refinement strategies are a natural choice and are employed by refining the mesh where the melt fraction changes rapidly and coarsening the mesh where melt fraction changes slowly. However, since the solution at the next time step is not known, the mechanism to define the criterion for regions of refined and coarsened mesh should be made from the values of porosity at the current and previous time steps. This criterion requires a refinement indicator for porosity since we are interested in the variation of porosity over time. In this case, the refinement indicator $\eta$ is based on the gradient of porosity and we can evolve the solution by using a refined mesh where the gradients are steep and a coarse mesh if the gradients are smooth. So for the refinement indicator, the gradient of porosity is calculated and stored for every cell.

$$\eta_k = |\nabla \phi_f^n(\boldsymbol{x}_k)|, \tag{3.19}$$

where $\boldsymbol{x}_k$ is the cell center. Based on this indicator, the top 20% of the cells with the highest gradient are marked for refinement and the bottom 20% of the cells with small gradients are marked for coarsening. The maximum level of refinement is user defined to control the overall cost of the mesh refinement. It is also ensured that the final mesh has no interfaces between cells that differ in refinement by more than one level. This constraint is imposed because of the restrictions of the deal.II package and not the robustness of DG methods which in general can handle more than one level of difference at the cell interface. While mesh coarsening and refinement should be done every time step for the accurate alignment of the mesh with the solution, the overhead associated with the transfer of solution from one mesh to the other at every time step renders this very costly. So, most of the results presented in this thesis were computed by adapting the mesh once every 50 time steps.

Now, by noticing that the gradients are sharp only in the x-direction in the context of magma upwelling, adaptive mesh refinement can be further improved by

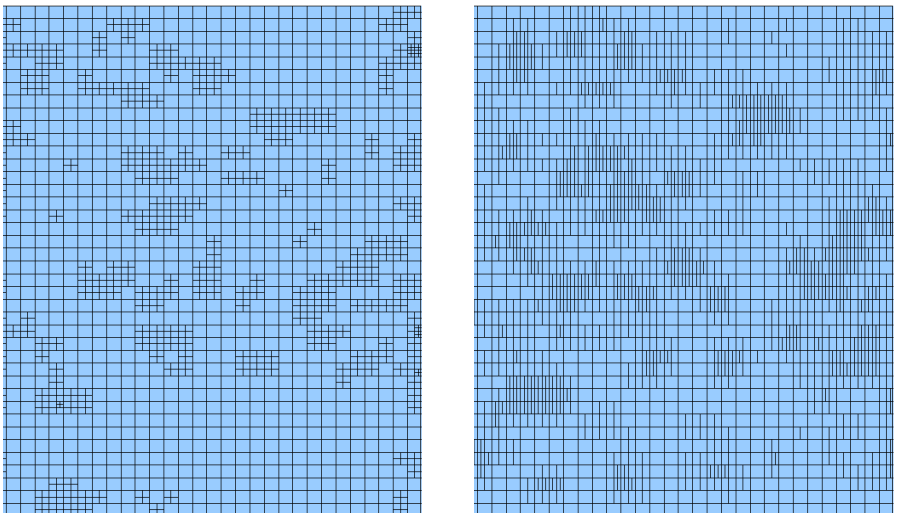

Figure 3.4: Comparison of isotropic (left) and anisotropic (right) mesh refinement

making it anisotropic. Based on the refinement indicators, the mesh is refined only in the x-direction while the mesh is uniform in the z-direction. Every cell marked for refinement is now divided into two cells in the x-direction unlike isotropic mesh refinement where the cell is typically refined in both the x and z-direction. Refer to Figure 3.4 for an illustration of this.

## 3.5 Parallelization

Parallelization in DG methods is carried out by partitioning the entire domain into blocks, where each processor does the computational work associated with the discretized operators of only those cells that belong to the block owned by the processor. Since the governing equations are time dependent, the domain is repartitioned if the adaptive mesh refinement is employed so that the load balancing remains even across the processors at all times. Figure 3.5 gives $2D$ and $3D$ examples of partitioned domains. The $2D$ partitioning is for a non-uniform mesh to illustrate that the processor load is distributed such that each the number of elements per processor is approximately the same. The $3D$ partition is for a uniform mesh. Strong scaling and weak

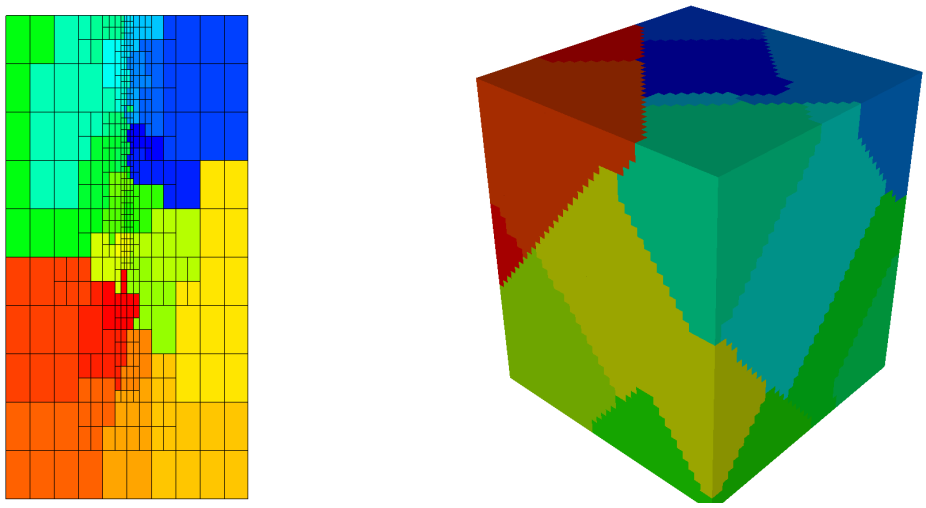

Figure 3.5: Domain partitioning for uniform and non uniform meshes in $2D$ and $3D$. Different colors correspond to different processors. The $2D$ domain is partitioned into 32 processors while the $3D$ domain is partitioned into 16 processors.

scaling studies were done to ensure that the computational time decreases with an increase in the number of processors (strong scaling) for a fixed total problem size and the load per processor is even (weak scaling). The results in Figure 3.6 show that the numerical setup is optimally scalable. As can be seen from the plots of weak scaling, the load balancing among the processors is better when the number of processors is less than 32 as the impact of the pressure solve is considerably less.

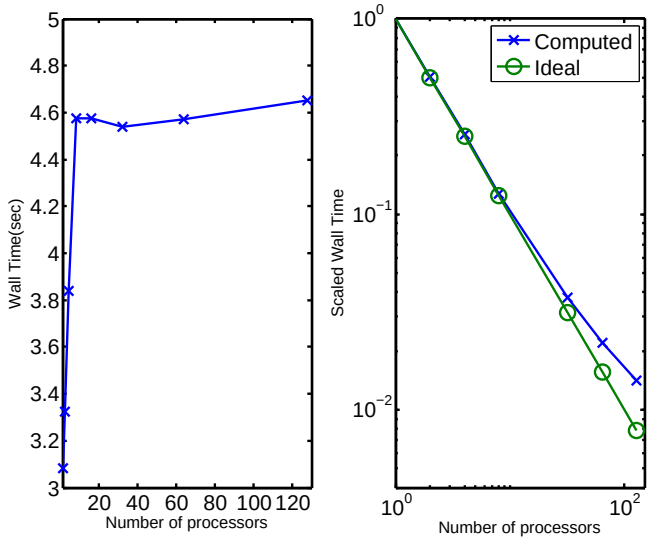


Figure 3.6: Strong and weak scaling analysis: Weak scaling for a Runge-Kutta time-step with 2000 dofs per processor using $P^2$ polynomials. Strong scaling using $P^2$ polynomials.

# Chapter 4

# Local Timestepping Methods

## 4.1 Motivation

Dunite channels constitute a small portion of the domain. Based on the studies done by Kelemen *et. al.* [35], dunite dykes or veins make up to $5 - 15\%$ of the mantle in the Oman ophiolites. Therefore, it can be inferred that dunite channels are formed in a small region of the domain under consideration. In order to study the features of dunite channels, a highly refined mesh is required near the channel and a coarse mesh otherwise. However explicit timestepping methods need to satisfy the Courant-Friedrichs-Lewy (CFL) condition for stability and this is given by:

$$\Delta t = C \min{}_k\{h_k\},$$

where C is a constant depending on the order of the DG polynomials and the stability region of the time stepping algorithm [21]. The drawback of explicit timestepping methods is that this restriction has to hold globally even if the most refined cells are only a small fraction of the whole domain which is typical of the channel regime problems in magma dynamics. Many multi-stage and multi-step methods have been proposed to address multi-rate problems [3, 23, 51]. In this chapter, we look at the

advantages of using local timestepping (LTS) methods wherein the problem is solved only in that part of the domain where the CFL condition for a particular timestep must be satisfied.

## 4.2 Numerical Method

Following the 2D numerical simulations in [53], we know that Gaussian boundary conditions result in high porosity channels in the upper part of the simulation domain where the amplitude of porosity is high. Also, across the high porosity channel, large horizontal gradients in porosity, $\phi_f$, and opx fraction, $\phi_{opx}$, are observed. The numerical method for these results uses $6^{th}$ order DG elements in the vertical dimension and a Fourier collocation scheme in the horizontal direction. This method consists of a uniformly high order method in the whole domain even though the prominent characteristics of $\phi_f$ and $\phi_{opx}$ are found in a small region near the channel boundary. To better and more efficiently resolve these horizontal gradients, we use a non-uniform mesh. To study the efficiency of DG methods with LTS in the context of magma migration, we consider a refined mesh near the channels and a coarse mesh elsewhere. The advantage of such a variable mesh is lesser memory usage and an improvement in the computational wall time. We could also consider a relatively low order method with a variable mesh to efficiently resolve the dynamics of the problem. In this case, spatial refinement (h-refinement) gives the required numerical accuracy achieved through order refinement (p-refinement). Therefore, to overcome the shortcomings in the numerical methods of [52, 53] and [41], we use DG numerical methods where there are no restrictions on element size and local approximation.

The resulting semi-discrete hyperbolic equations with spatial DG discretization can be integrated using an explicit method. This is simple to implement, requiring only function evaluations of the nonlinear right-hand sides to (2.17) and (2.18). The terms limiting time integration therefore are the upwelling and dissolution terms in

Table 4.1: Computational time for the major segments of the numerical scheme for $2^{nd}$ degree DG polynomials with 6400 cells.

| Section | Wall time(s) | % Total |
|---|---|---|
| Assemble Transport Equation | 2.94 | 15.0 |
| Assemble Pressure Equation | 6.84 | 35.0 |
| Solve Transport Equation | 0.01 | 0.1 |
| Solve Pressure Equation | 6.97 | 36.0 |

(2.17) and these are typically of comparable magnitude.

Although the time step is constrained by the hyperbolic equations, it requires us to assemble and solve the elliptic equation after every timestep. This accounts for the major computational time in evolving the system of equations over time. This can be seen in Table 4.1 which gives the time distribution for a domain consisting of $80 \times 80$ cells with $2^{nd}$ degree DG polynomial elements. Since the pressure equation only weakly affects the porosity and opx equations, local timestepping provides a good alternative to this problem if a method can be developed to efficiently include the constraint imposed on the advection equations because of the pressure equation. Local timestepping methods have been used for hyperbolic equations before [23, 26] and this chapter of the thesis extends the LTS formulation with a constraint for the hyperbolic equations in the form of the pressure equation within the context of melt migration.

### 4.2.1 Multi-Rate Multi-Step Methods

To understand the mechanism of multi-rate methods, we consider a domain with two levels; a refined level near the dunite channels and a coarse mesh otherwise. Let the values in the refined level be represented by the subscript $f$ and the values in the coarser mesh be defined by $s$. After the spatial discretization using DG methods, the

resulting ODE system can be represented as a $2 \times 2$ autonomous system of ODEs:

$$\partial_t \begin{pmatrix} f(t) \\ s(t) \end{pmatrix} = \begin{pmatrix} a_{ff}(f) + a_{fs}(s) \\ a_{sf}(f) + a_{ss}(s) \end{pmatrix}, \tag{4.1}$$

where the interaction between the fast and slow components is due to the flux terms at the interface of the coarse and refined cells.

The initial value problem is solved by a set of initial values for the fast and slow variables respectively,

$$f_0 = f(0) \qquad s_0 = s(0). \tag{4.2}$$

Multi-step methods are better suited for local timestepping methods as compared to multi-stage methods as the values at stages need to be calculated for the flux terms when solving the fast components at a time level that is not synchronized with the slow component. Half time-step calculations are easier to compute for multi-step methods as compared to multi-stage methods.

Adams-Bashforth methods are the most common multi-step methods. To illustrate the efficiency of local timestepping methods we consider four cases with refinement levels of 1, 2, 3 and 4, respectively, at the top of the domain based on the knowledge that there is a strong correlation between the boundary conditions and channel formation [41]. Let $n_l$ define the number of refinement level in the mesh and $N_l$ the total number of levels in the mesh. Let $t_{n_l}$ be time for level $n_l$ with known variable values. For example, the coarsest level in Figure 4.2 has $n_l = 4$ and the most refined level has $n_l = 1$. If $\Delta t$ is the maximum stable time step for the most refined level then $\Delta t_{n_l} = 2^{n_l - 1}\Delta t$. For local timestepping methods, time integration is performed at each level $n_l$ when the CFL condition at that level needs to be satisfied using 3rd order Adams-Bashforth method (AB3) which is given by:

$$\phi_f^{n+1} = \phi_f^n + (\Delta t)_{n_l}[\frac{23}{12} f_n - \frac{16}{12} f_{n-1} + \frac{5}{12} f_{n-2}],$$

where $f_n$ are the function evaluations from the right hand side in equation (2.17). For the function evaluations, all the cells that are in a particular refinement level, $n_l$, need only the solutions at the previous time steps corresponding to that level. Solutions may be needed from the coarser neighbor only for the upwinding flux terms and these can be extrapolated using Adams-Bashforth methods by integrating the right hand side for half time step. Like the fundamental derivation of Adams-Bashforth methods, we consider a polynomial $p(t)$ that passes through $f_{n_{l-1}}, f_{n-1_{l-1}}, f_{n-2_{l-1}}$ for the coarser neighbor as

$$p(t) = \sum_{i=0}^{2} f_{n-i_{l-1}} L_i(t),$$

where $L_i(t)$ are the Lagrange polynomials with the interpolation points corresponding to the previous stable time steps for that level. Then, the flux terms at half time step required for the flux computations of its refined neighbor can be derived by:

$$\phi_{f_{n+\frac{1}{2}}} - \phi_{f_n} = \int_{t_n}^{t_{n+\frac{1}{2}}} p(s)ds.$$

These methods work as expected for hyperbolic equations and have been used in various applications before [38, 3, 23, 51]. However in this approach, the constraint of the pressure equation, accounting for the major portion of the computational time, still needs to be solved globally even though the timestep constraint is imposed by the hyperbolic equations. Since the pressure varies slowly with time, the pressure solutions from the previous time steps can be used to extrapolate the solution at the intersection of the coarse and refined cells. Now to solve the pressure equation locally, the solution from the coarse neighbors is extrapolated to the half time steps of the refined neighbors when necessary. These extrapolated values of pressure provide the Dirichlet boundary conditions to solve the pressure equation locally. The local time stepping scheme is illustrated in Figure 4.1 and the algorithm for LTS methods is given in Algorithm 1.

**for** $n = 1 : 2^{N_l - 1}$ **do**

Find coarsest level $n_{l_{CFL}}$ such that the CFL condition for that level is matched: $t_n - t_{n_{l_m}} = (\Delta t)_{n_{l_{CFL}}}$

**for** *all levels,* $l \leq n_{l_m}$ **do**

Compute the right hand side terms, $f_i$ for $l < n_{l_m}$.

Compute the flux terms from the coarser level using $\phi_{f_{n+\frac{1}{2}}} - \phi_{f_n} = \int_{t_n}^{t_{n+\frac{1}{2}}} p(s)ds$

Advance $\phi_{f_n}$ only for cells of level, $l \leq n_{l_m}$

Extrapolate the pressure values from $n_{l_m+1}$ at the interface of the cells at level $n_{l_m}$ and $n_{l_m+1}$ to time $t_n$.

Solve the pressure equation only for cells of level, $l \leq n_{l_m}$ with the boundary conditions given by the actual boundaries or the coarser neighbors computed in previous step.

**end**

**end**

**Algorithm 1:** Local timestepping algorithm for one global time step.

Comparison of total time required to reach steady state for global RK3 and local AB3 methods is given in Table 4.2. Here $N_l$ is the total number of levels for the computation. As can be seen, Adams-Bashforth methods are not efficient for uniform meshes as the CFL condition is $\frac{1}{5}^{th}$ of RK3 methods. But as the number of levels increases, assuming the number of refined cells are only a small fraction of the total number of cells, the CFL condition is dominated by the number of function evaluations that are required at every time step. Thus, when local timestepping methods are used, the number of function evaluations are limited to the mesh that is needed for the CFL condition to be satisfied and as a result the computational wall time decreases as the number of function evaluations on the global mesh at every

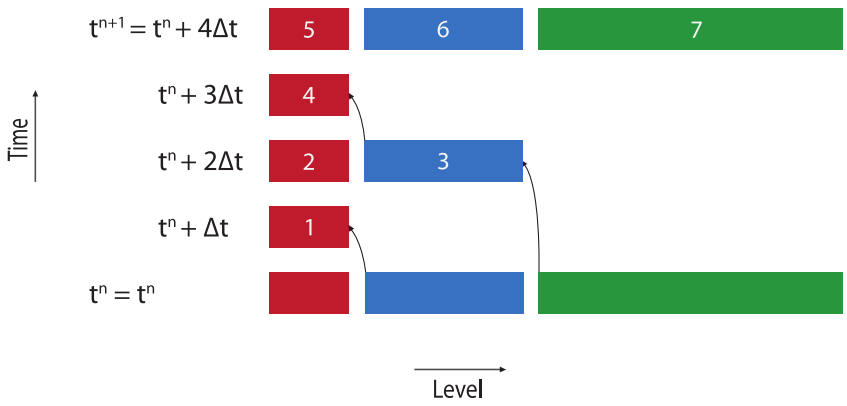


Figure 4.1: Local timestepping schemata for a 3 level mesh. The number indicates the order of evaluation and head of the arrows indicate the timestep at which the coarser neighbor needs to be extrapolated to the half timestep (see text for discussion).

time step take much longer time even though the CFL condition is greater for global Runge Kutta methods. While the results are shown for 2D channel regime problems, the percentage gain in computational time is more significant for 3D channel regime problems where the function evaluations and solver time is significantly more than 2D and the fraction of very refined cells is typically very small. Also, as the numerical simulations were run using deal.II, it puts an additional constraint on the maximum level difference between neighboring elements to be one level. The computational time can be vastly improved if the level difference between neighboring elements could increase.

Table 4.2: Wall time with local timestepping scheme for multilevel meshes.

| $N_l$ | **Assembling** | | **Solver** | | **Total Time (s)** | | **% Gain** |
|---|---|---|---|---|---|---|---|
| | RK3 | AB3 | RK3 | AB3 | RK3 | AB3 | |
| 1 | 2.19E+3 | 3.55E+3 | 1.28E+2 | 2.01E+2 | 2.32E+3 | 3.75E+3 | -61.49 |
| 2 | 4.42E+3 | 4.73E+3 | 2.51E+2 | 3.22E+2 | 4.68E+3 | 5.05E+3 | -8.06 |
| 3 | 1.16E+4 | 8.68E+3 | 1.58E+3 | 1.61E+3 | 1.32E+4 | 1.03E+4 | 22.21 |
| 4 | 4.08E+4 | 3.07E+4 | 7.81E+3 | 3.05E+3 | 4.86E+4 | 3.37E+4 | 30.53 |

## 4.3 Examples

The previous section illustrated the importance of local timestepping methods by guessing the region of channel formation. However, it is very difficult to guess the regions of melt migration priori. DG methods with adaptive mesh refinement can be used if the regions of dunite channel formation is not known. In order to capture the porosity variation at the boundary of the dunite channels, a uniformly refined mesh can be used but it can be computationally prohibitive. As can be seen in the previous case with uniform mesh (one level), in Figure 4.3, the mesh that was considered does not show channel bifurcation clearly. Adaptive mesh refinement with DG methods provides a good alternative to this in a computationally efficient manner for a general mesh that is more applicable for realistic problems. Adaptive mesh refinement strategies are employed by refining the mesh where the melt fraction changes rapidly and coarsening the mesh where melt fraction changes slowly. Following the strategies mentioned in Chapter 3, for adaptive mesh refinement based on the gradient indicator, results in Figure 4.4 illustrate the importance of refining the mesh only where necessary. As can be seen from Figure 4.4, the gradient of porosity captures all the essential features of channel formation and the mesh is refined only in the region of dunite channel boundary close to steady state.

Figure 4.5 shows a comparison of the line profile plot of porosity along $y = 2$ for uniform and adaptive mesh refinement. We get similar results using both the

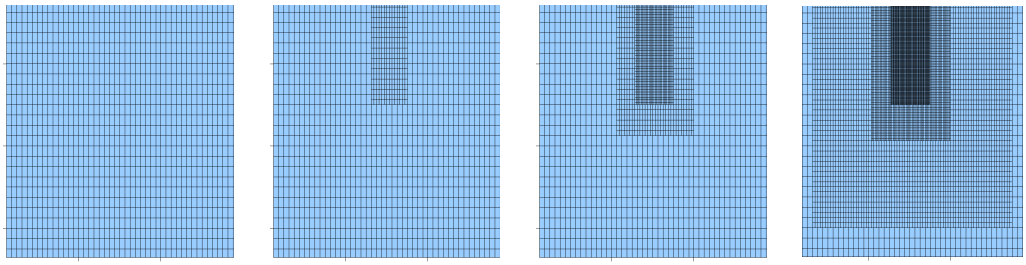

Figure 4.2: Meshes with various levels of refinement near the high-porosity channel(region enclosed by the boxes in Figure 4). From left to right, total number of levels are 1, 2, 3 and 4 respectively.

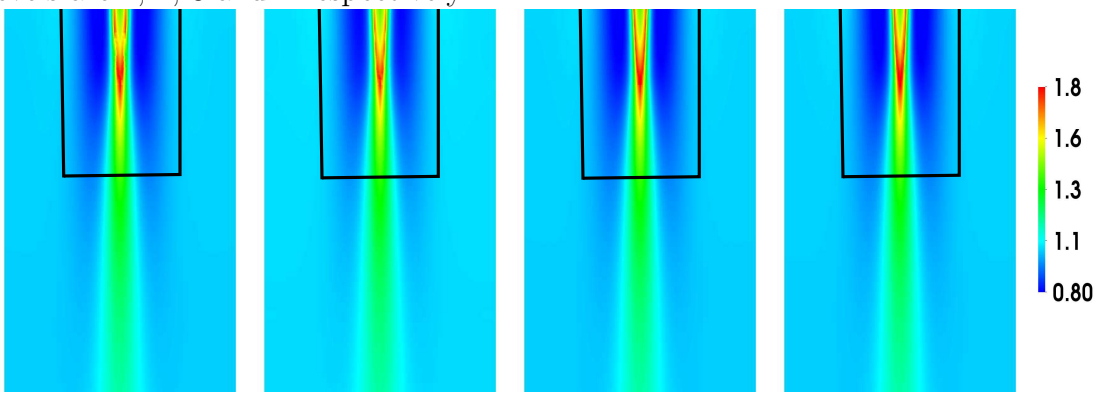


Figure 4.3: Steady state solutions with sustained Gaussian inflow perturbation for various levels of refinement near the high-porosity channel. From left to right, number of levels are 1, 2, 3 and 4 respectively. Meshes for the regions enclosed by the boxes are shown in Figure 4.2. All the simulations are using $3^{rd}$ order DG elements with 6400 cells in the coarsest level.

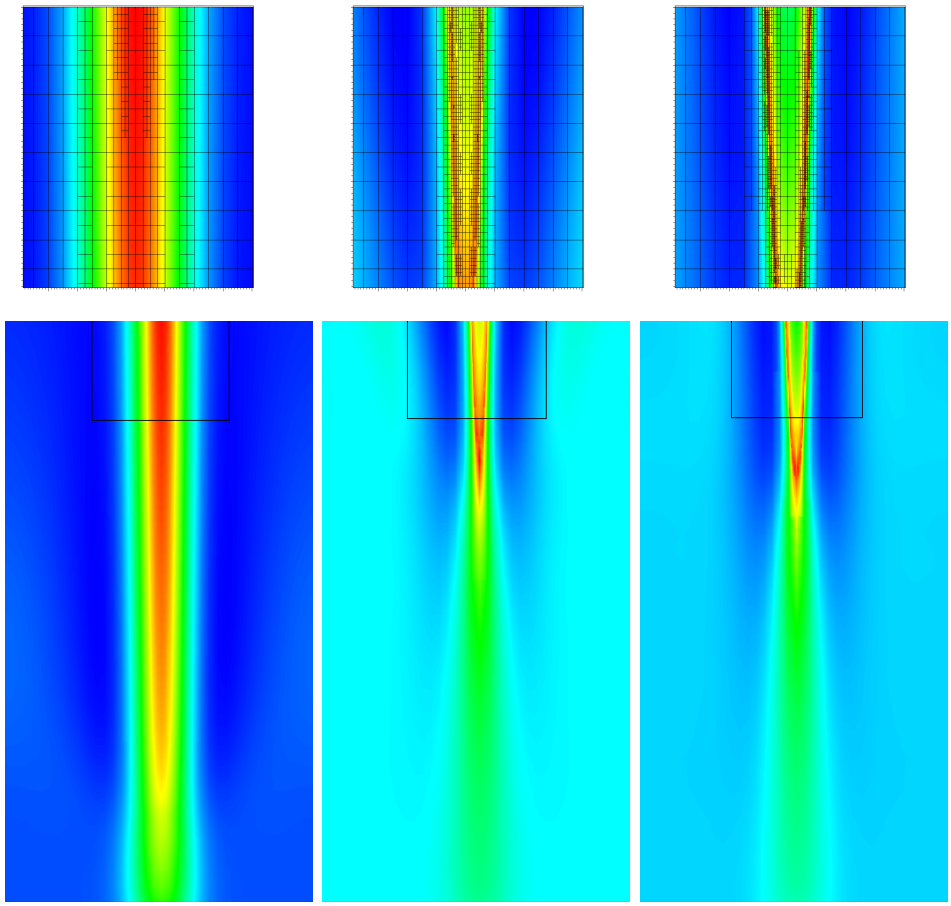

Figure 4.4: Bottom: Time variation of fluid fraction with sustained inflow perturbation and adaptive mesh refinement using $4^{th}$ order DG elements with 5 levels of maximum refinement. From left to right, t = 0.0, 1.2, 2.4. Top: Mesh refinement near the channels for the corresponding timesteps.

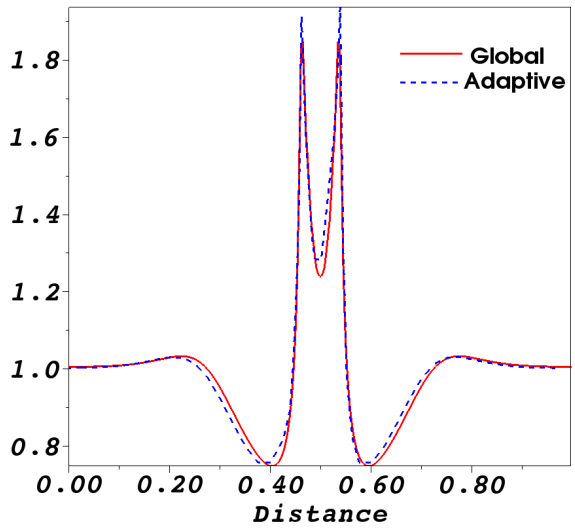


Figure 4.5: Line profiles of porosity at $t = 2.4$ along $z = 2$ using uniform mesh consisting of 10000 cells and adaptive mesh consisting of 4009 cells.

refinement strategies. The major advantage of using adaptive mesh refinement is that the number of cells and number of degrees of freedom are substantially less to capture the essential features of magma dynamics. The overall computational time decreases by 40% with an adaptive mesh for the simulation to run to steady state.

Based on the computational results, local timestepping methods provide a very good alternative to solve problems where the number of cells in the most refined cells are only a fraction of the total number of cells. But it is important to note that the CFL condition for local timestepping methods with more than one refinement level does not directly translate from the CFL condition for Adams-Bashforth methods. In fact, there is no theoretical estimate for the CFL condition in multi-rate schemes so far. The numerical work on stability of multi-rate multi-step methods is presented in [38] for further reference.

# Chapter 5

# Projective Pressure Estimation Methods

While the DG methods mentioned in Chapter 3 and Chapter 4 are well suited to study the characteristics of melt migration, there are two significant bottlenecks when solving these problems in 3D. As the problem size increases, the memory footprint of the global pressure matrix significantly increases. This is in particular the case as the degree of the polynomial increases, even when we consider an adaptive mesh. Table 5.1 gives the comparison between the memory occupied for a sparse matrix formulation as compared to a matrix free method. The second issue is that the time required to solve the pressure equation significantly increases during the time evolution of porosity and opx. The first issue is addressed by using a matrix-free solution of the finite element approximation for the pressure equation [40] and discontinuous Galerkin methods for the advection equations. Since all the operations in DG methods are local, there is no need to form a global matrix. The second issue is addressed, as discussed in Chapter 4, by observing that the pressure only weakly affects the advection equations. The local timestepping methods offer a motivation to seek an adaptive approach for solving the pressure equation exactly only when required. We shall discuss the use of a projective pressure estimation to reduce

Table 5.1: Comparison of memory requirements for the pressure equation

| #Cells | # dofs | Memory Consumption (MB) | |
|---|---|---|---|
| | | Sparse Matrix | Matrix-free |
| 6,400 (2D) | 25,921 | 3.28 | 1.63 |
| 40,000 (2D) | 160,801 | 20.50 | 11.10 |
| 384,000 (3D) | 3,136,441 | 1,581.07 | 231.75 |

computational cost of the iterative solver.

## 5.1 Motivation

Matrix-free methods offer distinct advantages for solving large problems as mentioned in the introduction. However, the time to solve the pressure equation efficiently remains a bottleneck. Table 5.2 gives a distribution of wall clock times for the major tasks to be performed until opx channel is formed for a 2D case. This highlights that it is necessary to solve the pressure equation only when necessary. Such ideas have been pursued with solving the pressure equation once per fixed number of time steps [1] or utilizing the particular form of elliptic equations [13]. In this work we explore an adaptive indicator of the pressure equation, driven by a user defined tolerance $\delta^*$, and use this indicator along with a projective pressure estimation to estimate the pressure for cases where an exact solver is not required.

Table 5.2: Wall time distribution for major segments to evolve the system

| Section | # calls | Wall Time (s) | % Total |
|---|---|---|---|
| Assemble + Solve Hyperbolic Equations | $1,000$ | $1.16e+03$ | 21% |
| Assemble Pressure RHS | $1,000$ | 150 | 2.7% |
| Output | 200 | 76 | 1.4% |
| Assemble+Solve Pressure | $1,000$ | $4.08e+03$ | 74% |

## 5.2 Numerical Method

Let $p^{n+1}$ be the pressure at the time step $n+1$ where the pressure is needed and let $p^{n_l}$ be the last time step at which the pressure was calculated through a global solve. We denote the matrix of previous global solutions by $\underline{p} = [p^n p^{n-1} p^{n-2} ..... p^{n-(n_{pp}-1)}]$ where $n_{pp}$ is the number of previous solutions we have collected. We assume that these vectors are orthonormalized. Let $\mathbf{A^{(n)}}$ be the matrix that is generated by the numerical discretization of the elliptic operator and $f^n$, the right hand side at time step number $n$.

If the tolerance of the iterative solver is given by $\epsilon$, then $p^n$ is the solution of the discretized PDE given as

$$||\mathbf{A}^n p^n - f^n|| < \epsilon.$$

Let

$$||\mathbf{A}^{(n+1)} p^{n_l} - f^{n+1}|| = \delta,$$

and assume that $p^{n+1} = \underline{p}\alpha$, i.e. a simple linear combination of past pressure computations but with their linear combination recovered by satisfying the pressure problem at the current stage. If $p^{n+1}(x)$ does not vary rapidly with time, this linear combination should offer a good approximation, obtained at a limited cost. To gauge the accuracy of the projective pressure estimation, we need to find a criterion to decide if $p^{n+1}$ can be expressed through $\underline{p} = [p^{n_l} p^{n_l-1} p^{n_l-2} ..]$ or if a full solution is required.

Generally we require

$$||p^{n+1} - p^{n_l}|| < C\delta^*,$$

where $C$ is a constant . Since we do not know $p^{n+1}$ we will estimate it in terms of

known quantities.

$$\begin{aligned} ||p^{n+1} - p^{n_l}|| &= ||\mathbf{A}^{(n+1)^{-1}} f^{n+1} - p^{n_l}|| \\ &= ||\mathbf{A}^{(n+1)^{-1}} f^{n+1} - \mathbf{A}^{(n+1)^{-1}} \mathbf{A}^{(n+1)} p^{n_l}|| \\ &\leq ||\mathbf{A}^{(n+1)^{-1}}||||\mathbf{A}^{(n+1)} p^{n_l} - f^{n+1}|| \\ &\leq C\delta^*, \end{aligned}$$

where $C = ||\mathbf{A}^{(n+1)^{-1}}||$ and the user defined tolerance $\delta^*$ that can be checked in terms of known quantities is given by the residual

$$||\mathbf{A}^{(n+1)} p^{n_l} - f^{n+1}|| < \delta^*.$$

This criterion is cheap to check as it involves just one matrix-vector multiplication.

To summarize, details of the algorithm using projected pressure estimation to compute the pressure based on the user defined tolerance is given in Algorithm 2.

**for** $n = 4 : N$ **do**
  Compute $\delta$;
  **if** $\delta < \delta^*$ **then**
    Solve $\underline{p}^T \mathbf{A}^{(n+1)} \underline{p}\alpha = \underline{p}^T f^{n+1}$ for $\alpha$
    $p^{n+1} = \underline{p}\alpha$
  **else**
    Solve $\underline{p}^T \mathbf{A}^{(n+1)} \underline{p}\alpha = \underline{p}^T f^{n+1}$ for $\alpha$
    Use $p^{n+1} = \underline{p}\alpha$ as the initial guess to solve the pressure equation. Solve $\mathbf{A}^{(n+1)} p^{n+1} = f^{n+1}$ for $p^{n+1}$
    Update $\underline{p}$
  **end**
  Solve for $\phi_f^{n+2}$ and $\phi_{opx}^{n+2}$ using $p^{n+1}$
**end**

**Algorithm 2:** Projective Pressure Estimation for time steps $n \geq 4$

## 5.3 A Note on Numerical Implementation

The algorithm in the previous section gives the criterion for solving for pressure exactly. However, the efficiency of the method relies on fast computation of matrix-vector multiplications. There are many methods that take advantage of GPU computations for fast matrix-vector multiplications ([38] and references therein). The projective pressure estimation methods can directly be used for GPU computations. For CPU computations, computational strategies that make floating point multiplications faster than the time required to access the data from memory are required. In other words, the computational algorithm to recompute the operator every time must be cheaper than storing entries in a global matrix and accessing them during solving stage. For this purpose, we follow the procedure in [40].

To describe the mechanism of the matrix-free methods mentioned in this paper, let us first consider a traditional way of solving the Helmholtz equation (by finite

element method for simplicity.)

$$-\nabla \cdot [\phi_f^3 \nabla p] + \phi_f p = -R \frac{\partial \phi_f^3}{\partial z} \tag{5.1}$$

The local matrix for each cell is given by the product of three matrices.

$$A_{loc} = B_{loc}^T D_{loc} B_{loc} \tag{5.2}$$

where $B_{loc}$ contains the information of the gradients and values of the test functions at the quadrature points in the cell and $D_{loc}$ is a diagonal matrix that contains the product of the Jacobian, quadrature weights and values of $\phi_f^3$ at the quadrature point. This local matrix $A_{loc}$ is then added to the global matrix, $A_g$. During the solving stage of an iterative method without a preconditioner, the resulting global matrix $A_g$ is multiplied with the solution vector and the residual of the right hand side, $f_{rhs}$, and this matrix-vector product is compared with a user defined tolerance. If the residual exceeds the tolerance, the new value of the solution vector is defined using the previous guess of the solution, the right hand side and the global matrix. This new value of the solution vector depends on the iterative method being employed.

At the assemble stage, the matrix-free methods can instantly reduce the computational work load since the three matrices in (5.2) are never formed but instead there are three successive matrix-vector products.

$$A_{loc}.u = B_{loc}^T D_{loc} B_{loc}.u \tag{5.3}$$

However, the real gain to computational wall time comes from bypassing the stage where the gradients and values of the shape functions in real space are computed which is done traditionally by transforming the gradient and values on the reference cell to real space using the Jacobian of the transformation. Essentially the whole process is converted into a series of local matrix-vector products instead of creating a

global sparse matrix and multiplying it with the global solutions during the solution stage as.

$$v_{loc} = B_{loc}^T J_{loc}^T D_{loc} J_{loc} B_{loc}.u \tag{5.4}$$

where $J_{loc}$ gives the Jacobian transformation from the unit to the real cell. For more information on the implementation of matrix-free methods, we refer [40].

## 5.4 Examples

The average number of iterations to solve the pressure equation at every time step can be improved by either providing the iterative solver with a good initial guess to the pressure solution or a good preconditioner to the matrix. The projective pressure estimation method can be used at every time step ($\delta^* = 0$) and the initial guess to the pressure solution comes from a linear combination of the previous solutions, $\underline{p}\alpha$. Table 5.3 gives the average number of iterations for an $80 \times 80$ mesh for various choices of $n_{pp}$. It can be seen that the average number of iterations goes down as the number of previous solutions in $\underline{p}$ increase. Going further, we can improve the computational

Table 5.3: Average number of iterations to solve the pressure equation with an initial guess using $n_{pp}$ previous solution vectors

| $n_{pp}$ | Average # of iterations |
|---|---|
| 1 | 313 |
| 2 | 112 |
| 3 | 82 |
| 4 | 73 |

speed by solving the pressure equation exactly only when the residual $\delta$ is greater than the user defined tolerance $\delta^*$, otherwise we use the projected solution. In the present study we take $\underline{p} = [p^n p^{n-1} p^{n-2}]$.

Table 5.4 gives the computational time to solve a given set of equations until opx becomes zero for a $40 \times 40$ mesh. We observe from the table that even though the number of calls to solve the pressure equation is less than 10% for $\delta^* = 0.25$ as compared to solving the pressure equation at every time step, the gain in computational time is about six times. This is due to the average number of iterations to solve the pressure equation increases as the projected solution slowly drifts further away from the actual solution. Figure 5.1 gives a graphical comparison of the solutions at various times for various choices of $\delta^*$. As $\delta^*$ increases the solution deviates from the pressure solution obtained by solving the pressure equation at every time step. This shows that for the higher values of $\delta^*$ the projective pressure estimate deviates from the true solution of pressure which results in an error in computing the porosity solution as well. The opx solution deviates relatively less compared to porosity solution since there is no compaction term ($p\phi_{opx}$) in the opx equation. In practice, it has been observed that taking $\delta^* = 10^{-3}\epsilon$ where $\epsilon$ is the tolerance for the iterative solver results in an efficient use of the projective pressure estimated solution.

Table 5.4: Variation of wall time with user defined tolerance

| $\delta^*$ | # calls | Wall Time (s) |
|---|---|---|
| 0 | 1000 | $1.37e+04$ |
| 0.05 | 128 | $3.05e+03$ |
| 0.15 | 98 | $2.58e+03$ |
| 0.25 | 87 | $2.31e+03$ |

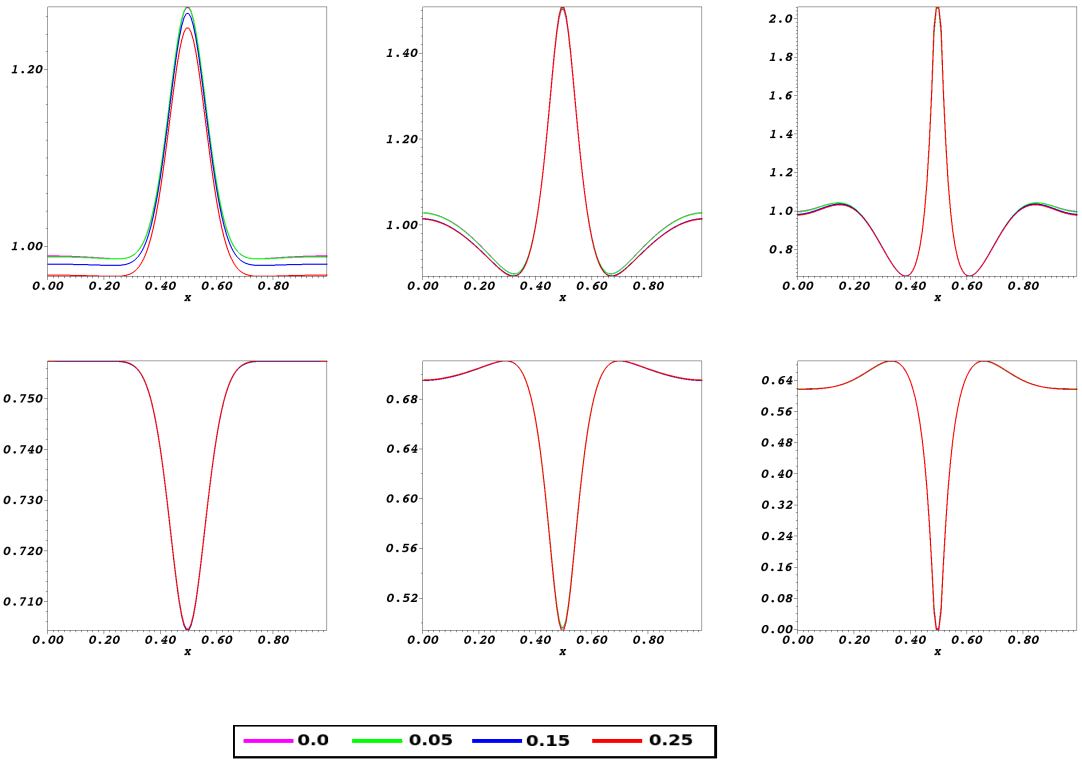


Figure 5.1: Time variation of solutions with sustained inflow perturbation for $\delta^* = 0, 0.05, 0.15, 0.25$. Top: fluid fraction. Bottom: opx fraction. From left to right, t = 0.25, 0.625, 1.0

# Chapter 6

# 2D Results

## 6.1 Introduction

This chapter presents the results for the numerical simulations to understand the lithology and geometry of high-porosity melt channels. The final governing equations are given by equations (2.17)-(2.21). Linear stability analysis done by [27] shows that the governing equations allow steady-state solutions in the z-direction. Further, the stability of the steady-state solution to infinitesimal transverse perturbations was addressed by linearizing the governing equations around the steady state. This is done by assuming the perturbations of the form $\hat{\boldsymbol{y}} = \tilde{y}(z)e^{\sigma t + \mathrm{i}kx}$ where $\tilde{y}(z)$ are eigenfunctions to be determined, $\sigma$ is the eigenvalue governing the temporal evolution of the perturbation and $k$ is the horizontal wave number. The resulting eigenvalues of the stability problem was solved numerically in [52] using DG methods. Important conclusions from the analysis in [27] is that the eigenvalues are complex for all $k$ and the corresponding eigenfunctions are complex and oscillatory. This implies that the steady solution is unstable to an oscillatory instability with a growth rate given by $Re[\sigma]$ and the angular frequency of the oscillations by $|Im[\sigma]|$. The linear stability analysis thus gives the conditions under which compaction-dissolution waves or high porosity channels form spontaneously in an upwelling, viscously deforming column.

## 6.2 High-Porosity Channel Formation

To understand the fundamental process of reactive dissolution, we consider the parameters resulting in a regime stable to porosity perturbation. For this, we consider a domain of size $(x, z) \in [0, 1] \times [0, 2]$ with the dimensionless parameter values $\delta = 10^{-2}$, $R = 10^2$ and $\frac{\phi_f^0}{\phi_{opx}^0} = 0.02/0.15$. The time-dependent governing set of equations, (2.17) - (2.21), with the above parameters and a Gaussian perturbation at the boundary for porosity are solved to steady state (approximately one solid overturn time, $t = 2$). The exact form of the boundary equations is given by:

$$\phi_f(x; y; 0; t) = 1 + A \exp(-100(x - \frac{x_{max}}{2})^2).$$

where $A$ is non-zero in the examples discussed in this section. The corresponding plots of porosity and opx are shown in Figure 6.1.

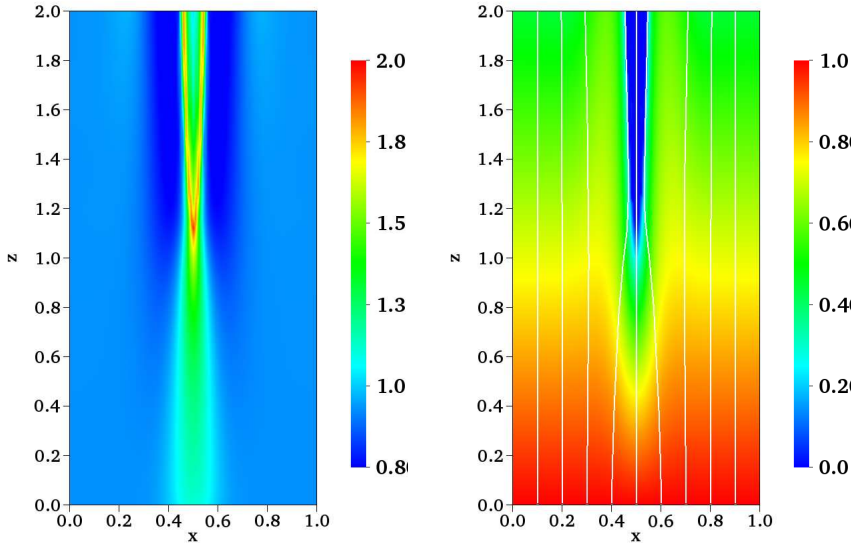


Figure 6.1: Steady state distributions of porosity (left) and opx (right) volume fractions in an upwelling column. The dark blue region in the opx plot is the opx-depleted dunite channel.

There is a constant higher influx of melt at the center of the lower boundary (x=0.5) which results in a higher dissolution rate (2.19). This sustained influx of melt accumulates and eventually depletes all the opx available for dissolution. This results in an opx-free dunite channel in the upper part of the column (blue region in Figure 6.1. The lower part of the column is harzburgite (contains both opx and olivine). When opx is completely exhausted in the dunite channel, there is no further melt generated in the dunite channel and the main melt channel splits into two smaller channels due to compaction in the dunite channel. A compacting boundary layer is observed outside the main channel features where the opx fraction increases compared to the far-field observations. Melt velocity streamlines in Figure 6.1 show the effects of melt focusing and isolation of melt and the matrix. As discussed in [52], the melt is focused from the surrounding matrix into the high-porosity dunite channel in the lower part of the upwelling column and around the tip of opx-free dunite channel. Melt localizes towards the dunite-harzburgite boundary in the upper part of the dunite channel because of the compaction within the dunite channel. There is a slight enrichment of melt near the outer-edge of the boundary layer because of compaction within the compacting boundary layer.

The depth of the dunite channel initiation and the characteristics of dunite channels depend on many other factors such as solubility gradient, soluble mineral abundance, inflow melt flux, melt suction rate and upwelling rate. A rigorous study of all these factors was done in [52] for 2D problems. It was shown that the depth of the dunite channels increases as the width of the inflow melt flux gets narrower. This results in a greater gradient in the perturbation which leads to more melt focusing and stronger compacting boundary layers. Similar analysis shows that as the soluble mineral opx abundance increases, the depth of the dunite channel decreases.

To compare with the 2D results of [53], we re-run a set of 5 simulations presented in Figure 7 of [53] for the amplitude $A = \{0.05, 0.1, 0.2, 0.4, 0.8\}$ using the more general numerical scheme developed here. To better and more efficiently resolve

large horizontal gradients, we use a highly non-uniform mesh which results in the reduction of the overall computational wall time.

Figure 6.2 displays steady-state distributions of the porosity (upper panels) and soluble mineral abundance ($\phi_{opx}$, lower panels) in the 2D domain for the five cases. These results agree very well with those reported in [53], including channel geometry (e.g., its width and depth), compacting boundary layers outside the high-porosity channels (deep blue regions in the upper panels), and melt channel bifurcation (two red branches within the dunite channels, upper panels). The larger perturbation or amplitude at inflow implies greater lateral porosity gradient leading to deeper and wider dunite channels.

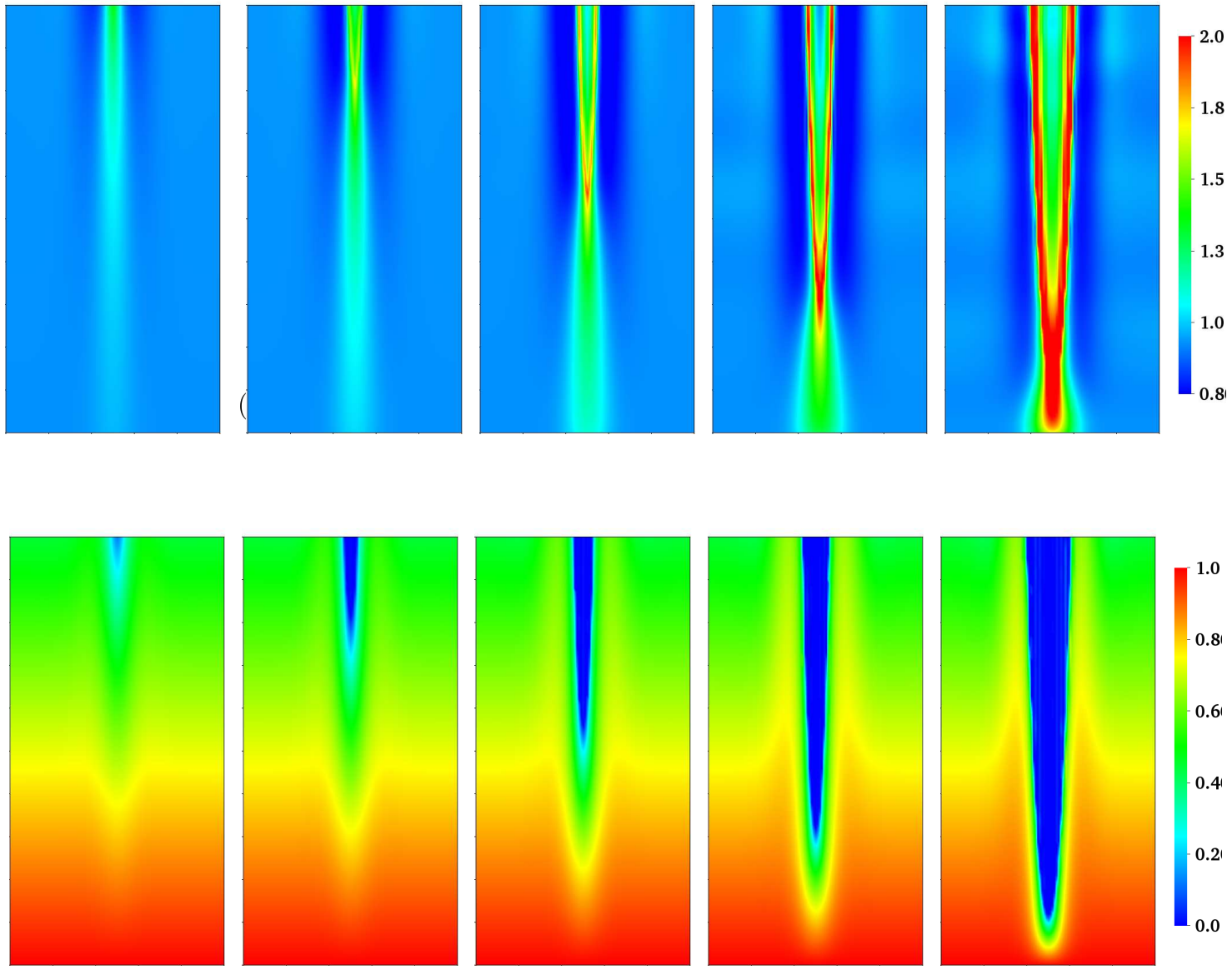


Figure 6.2: Steady state solutions with sustained inflow perturbation. Top: fluid fraction. Bottom: opx fraction. From left to right, $A = \{0.05, 0.1, 0.2, 0.4, 0.8\}$. Computational domain is $(x, z) \in [0, 1] \times [0, 2]$.

## 6.3 Compaction-Dissolution Waves

Let us now consider a domain of size $(x, z) \in [0, 2.8] \times [0, 6.75]$ with the dimensionless parameter values $\delta = 10^{-2}$, $R = 10^2$ and $\frac{\phi_f^0}{\phi_{opx}^0} = 0.01/0.20$. This results in a reaction feedback which leads to the spontaneous formation of compaction-dissolution waves. The boundary conditions are time-varying and numerically resolvable random perturbations. Before we consider the properties of dunite channel formation in this more realistic situation, it is informative to first consider the evolution of porosity and opx fractions when a time-independent Gaussian perturbation is imposed at the boundary.

### 6.3.1 Gaussian Perturbation

A Gaussian perturbation in the wave regime results in a dunite channel formation because of melt focusing as is the case in the channel regime simulations. After the initial effects of the boundary perturbation have fully evolved, the non linear interactions of the dunite channel and the porosity field results in wavelike features emerging. The strength of these waves increases they induce secondary high porosity regions which in turn increases the dissolution rate in these regions, thus resulting in the formation of secondary dunite channels. The time evolution of porosity and opx fractions in this case are shown in Figure 6.3.

### 6.3.2 Random Perturbation

Nonlinear interaction between dissolution, compaction, and solid upwelling can also give rise to compaction-dissolution waves [27, 52, 53]. We consider reactive dissolution in a $5.7 \times 6.75$ rectangular domain(measured in compaction length). Compaction length is similar to the definition given in [43] and in Chapter 2. This domain is an approximation of the uppermost part of the upwelling mantle beneath the mid-ocean ridge.

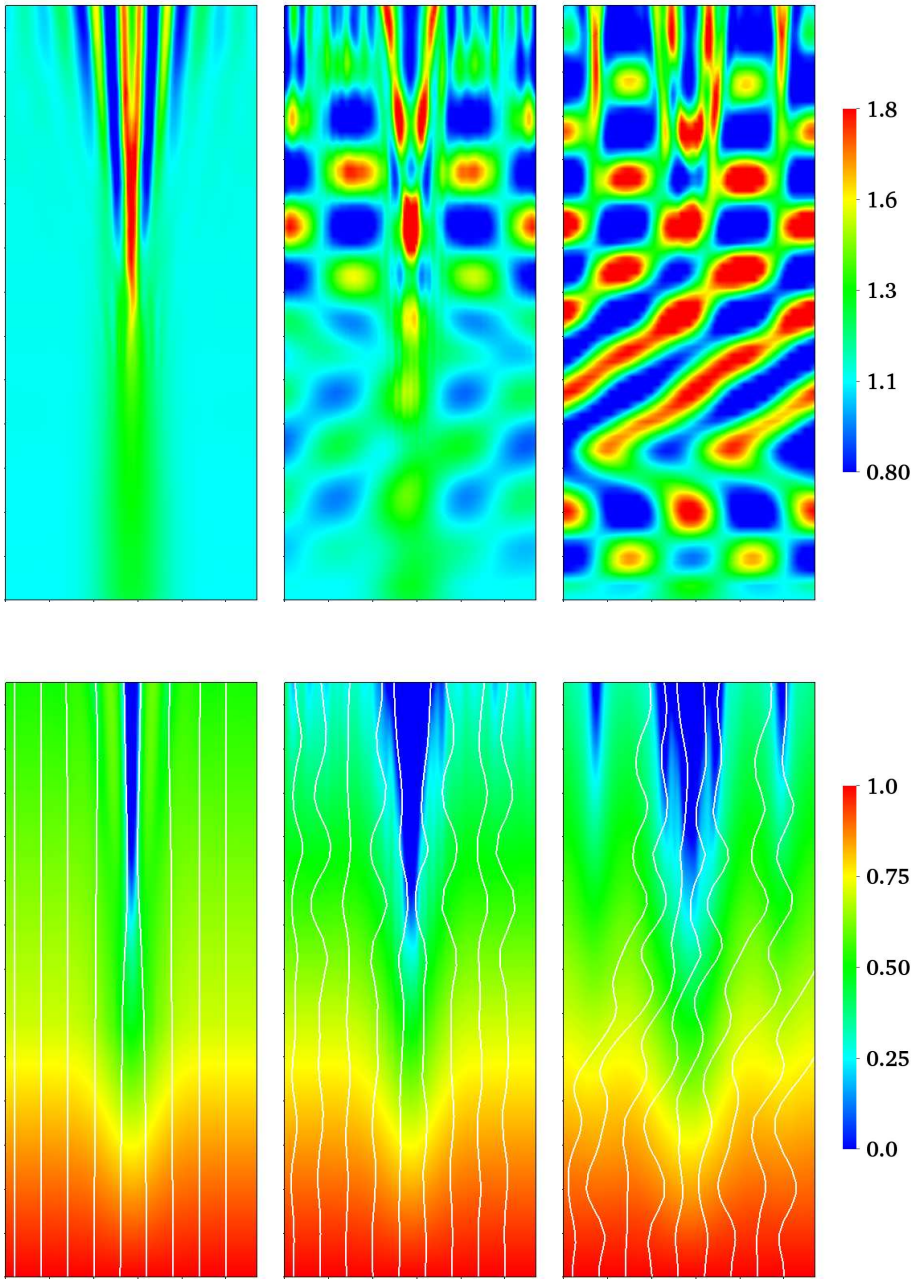


Figure 6.3: Porosity (top) and opx (bottom) volume fractions at $t = \{2.8, 24.0, 30.0\}$ Secondary channels are formed and the wave pattern emerges after 4 turnover times. Computational domain is $(x, z) \in [0, 2.8] \times [0, 6.75]$.

Figure 6.4 displays spatial and temporal evolutions of porosity (upper panels) and opx fractions in the simulation domain at four selected times. Random initial conditions diffuse out and the random boundary conditions slowly result in well organized waves before one solid overturn time (the time required for the solid to traverse through the domain once). At the end of the second solid overturn time, compaction-dissolution waves are fully developed at the lower half of the domain while high porosity channels are initiated at the top. The localization of the melt into the channels that are formed in the top half of the domain dissolves the remaining. Close to the third overturn time, six well-developed opx-free dunite channels are formed. Downward growth of these high porosity channels perturbs the local melt flow field which causes continuous nonlinear interactions between the lower part of the domain and the channels in the upper part. This eventually leads to a decrease in the wavelength of the porosity waves and an increase in the number of dunite channels to eight by the fourth overturn time after which it reaches a quasi-steady state.

### 6.3.3 Wave Regime Results with Anisotropic Mesh Refinement

We discussed the advantages of adaptive mesh refinement in Chapter 4 for channel regime computations. Adaptive mesh refinement can be used in the wave regime context as well. However by noticing that the gradients are sharp only in the x-direction, adaptive mesh refinement can be further improved by making it anisotropic. Based on the refinement indicators, the mesh is refined only in the x-direction while the mesh is uniform in the z-direction. Every cell marked for refinement is now divided into two cells in the x-direction unlike isotropic mesh refinement where the cell is refined in both the x and z-direction which results in four refined cells. Figure 6.5 shows the formation of dunite channels with three levels of anisotropic mesh refinement in the background. Based on the refinement indicators for each cell, the

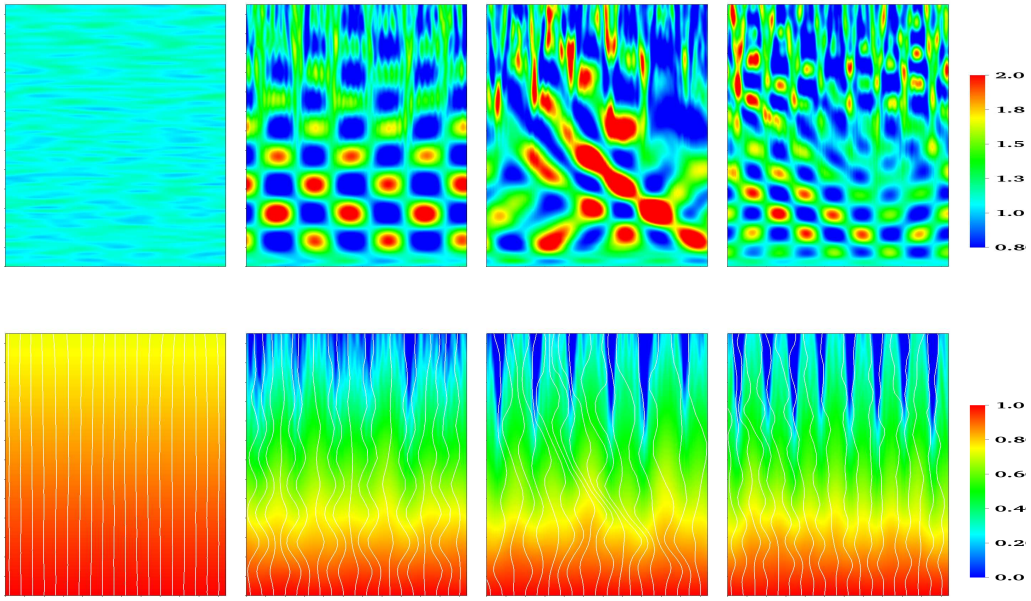


Figure 6.4: Time variation of solutions with $4^{th}$ order DG elements and random inflow perturbation and uniform mesh refinement with 3600 elements.
Top: fluid fraction. Bottom: opx fraction. From left to right, $t = \{0.0, 6.4, 15.2, 36.2\}$. Computational domain is $(x, z) \in [0, 5.7] \times [0, 6.75]$.

top 20% of the cells are marked for refinement while the bottom 30% are marked for coarsening. The anisotropic mesh refinement ensures that the mesh is refined only where the channels are formed and coarse everywhere else. These simulations were run in parallel with 128 processors and the wall time with anisotropic mesh refinement is 2 hours, an improvement over uniform mesh solutions by a factor of 2.

### 6.3.4 Wave Properties

To study the characteristics of melt migration, it is important to consider if the flow is dispersive or non dispersive and the characteristics of the wave patterns observed. This is important to understand if the melt observed on the surface comes

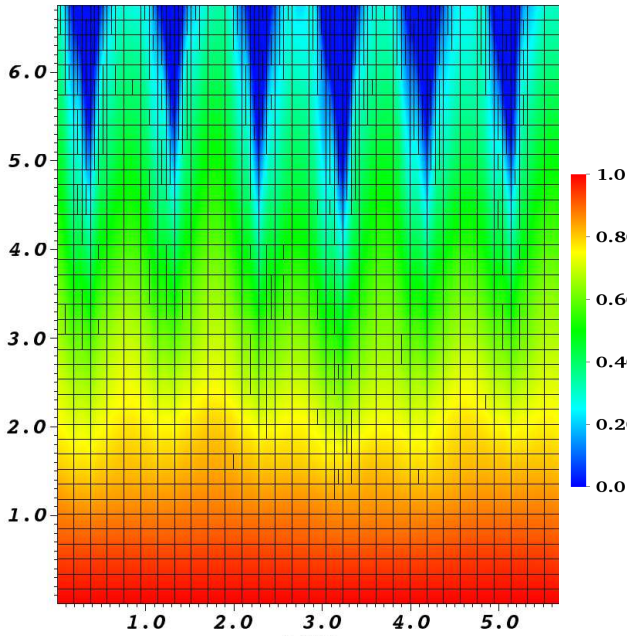


Figure 6.5: Spatial variations of normalized opx fraction in the simulation domain at $t = 15.0$ with anisotropic mesh refinement using 4th order DG elements with a fixed number of 60 elements in the z-direction. The elements in the x-direction are anisotropically refined with 3 levels of maximum refinement. The mesh is refined only in the x-direction.

directly from underneath or it comes from a different and deeper x location. For this, two points in the domain are considered, one in the bottom part of the domain at $P_b = (1.707, 1.0125)$ where the waves are well developed after 3 overturn times. The other point is considered near the top of the domain where dunite channel at $P_b = (1.707, 6.075)$. On taking the FFT of the x variation of the porosity, we observe that the initial distribution of porosity at the bottom and the top is composed of a number of Fourier modes. However, as time progresses the bottom point slowly evolves into well developed waves with a dominant wavenumber of 3. The distribution, disturbed because of the interaction with the dunite channels, again evolves into well developed waves but with a dominant wavenumber of 4 at quasi-steady state. On the contrary,

the variation of porosity in the x-direction at the top is never dominated by any single Fourier mode. This seems to indicate that the flow is always dispersive towards the top. An empirical or experimental understanding of the dispersion relation is required to quantify the wave properties like phase velocity and group velocities of the waves.

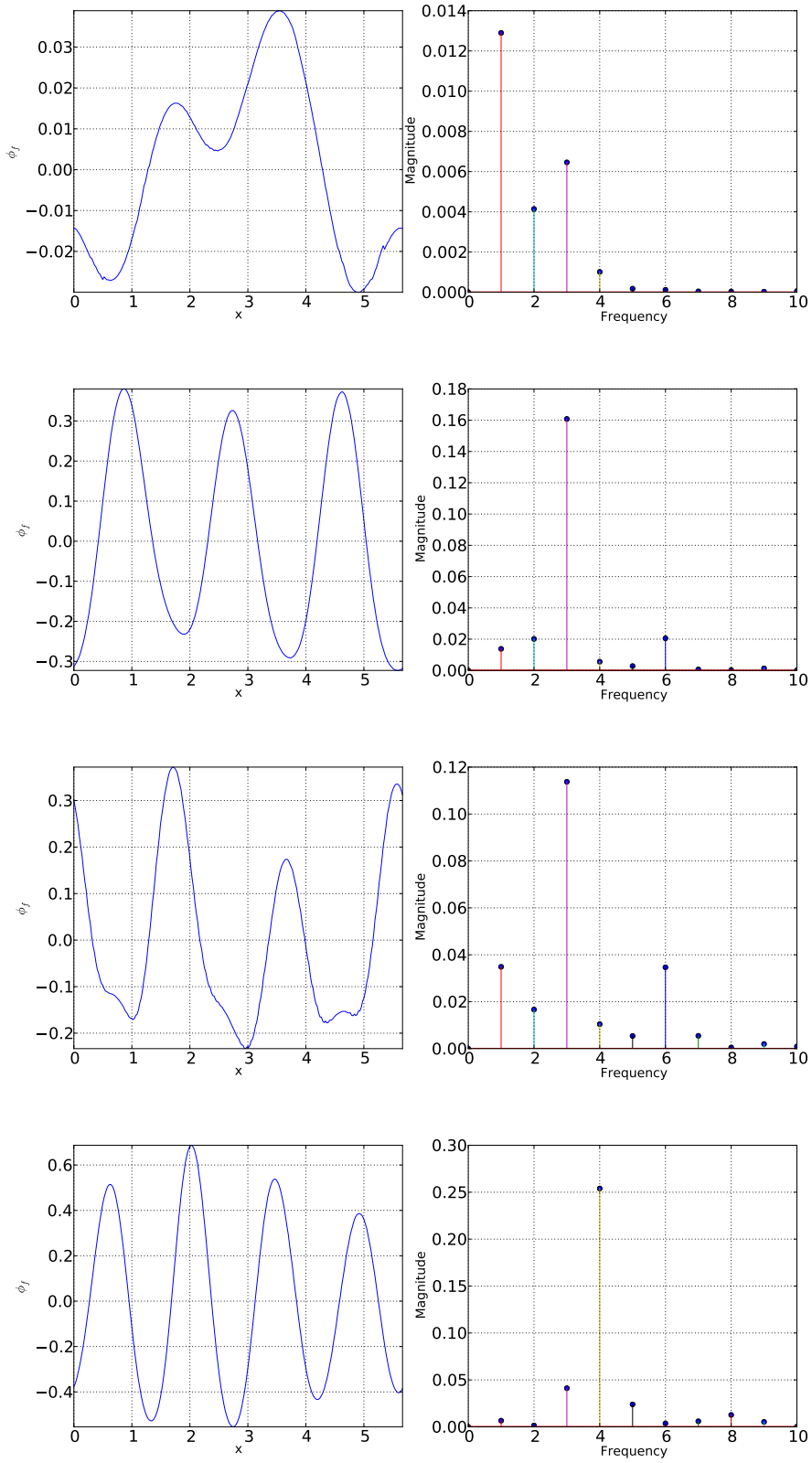


Figure 6.6: Line plots of porosity on the left and the corresponding Fourier modes on the right at the point $P_b = (1.707, 1.0125)$. From top to bottom $\{t = 0, 12.8, 16.2, 40.0\}$

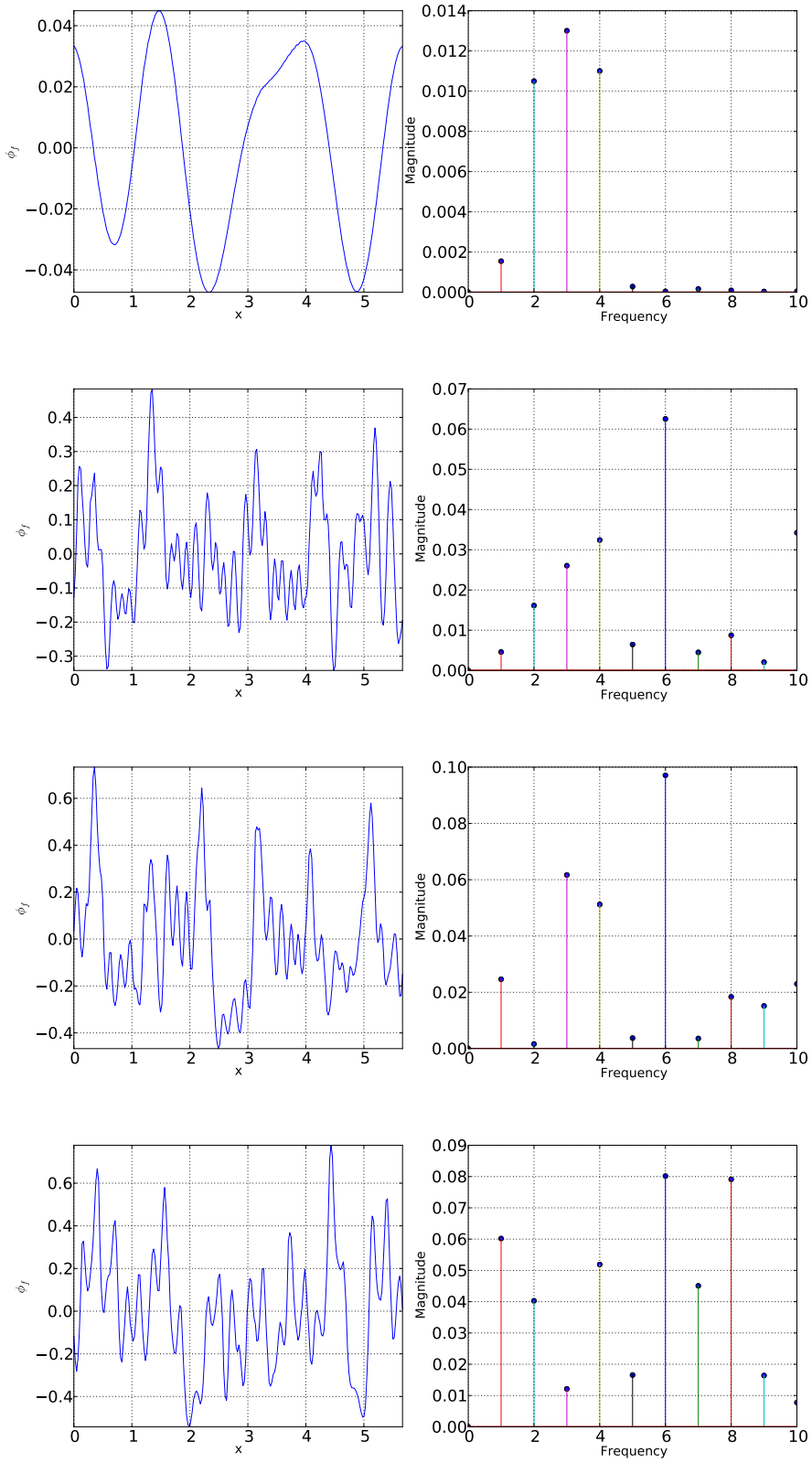


Figure 6.7: Line plots of porosity on the left and the corresponding Fourier modes on the right at the point $P_t = (1.707, 6.075)$. From top to bottom $\{t = 0, 12.8, 16.2, 40.0\}$

## 6.4 Other Results

### 6.4.1 Effect of Variable Viscosity

The results discussed so far assume that the shear viscosity is a constant. Equations for the conservation of momentum (or force balance) for the melt and solid matrix has been studied in a number of papers ([43, 54, 7]). Following the summary in [46, 53] but changing the unit vector in the vertical z direction to be positive upward, the momentum conservation equation is given as

$$\nabla \cdot \{(1-\phi_f)[(p_f - p_s)\mathbf{I} + \tau_s]\} - (1-\phi_f)\triangle\rho g\mathbf{n}_z + \frac{\mu}{\kappa_\phi}\phi_f(\mathbf{v}-\mathbf{V}) = 0, \tag{6.1}$$

where $\mathbf{I}$ is the unit tensor and $\tau_s$ is the deviatoric stress (stress that controls the distortion) in the solid matrix.

$$\tau_s = \eta[\nabla\mathbf{V} + (\nabla\mathbf{V})^T - \frac{2}{3}\nabla\cdot\mathbf{V}\mathbf{I}]. \tag{6.2}$$

Equation (6.1) can also be written as

$$\phi_f(\mathbf{v}-\mathbf{V}) = -\frac{\kappa_\phi}{\mu}\{\nabla\cdot[(1-\phi_f)[p\mathbf{I}+\tau_s]\} - (1-\phi_f)\triangle\rho g\mathbf{n}_z\}. \tag{6.3}$$

In the limit of small porosity, which is true for melt migration in the mantle, we get

$$\begin{aligned}\phi_f(\mathbf{v}-\mathbf{V}) &= -\frac{\kappa_\phi}{\mu}\{\nabla p + \eta[\frac{4}{3}\nabla(\nabla.\mathbf{V}) - \nabla\times\nabla\times\mathbf{V}] - \triangle\rho g\mathbf{n}_z\} \\ &\quad -\frac{\kappa_\phi}{\mu}\{\nabla\eta\cdot[\nabla\mathbf{V} + (\nabla\mathbf{V})^T - \frac{2}{3}\nabla\cdot\mathbf{V}\mathbf{I}]\}.\end{aligned}$$

Experimental observations in [54, 56] suggest a linear relationship between excess melt pressure and compaction rate:

$$p = \xi\nabla\cdot\mathbf{V} = \frac{\eta}{\phi_f}\nabla\cdot\mathbf{V}. \tag{6.4}$$

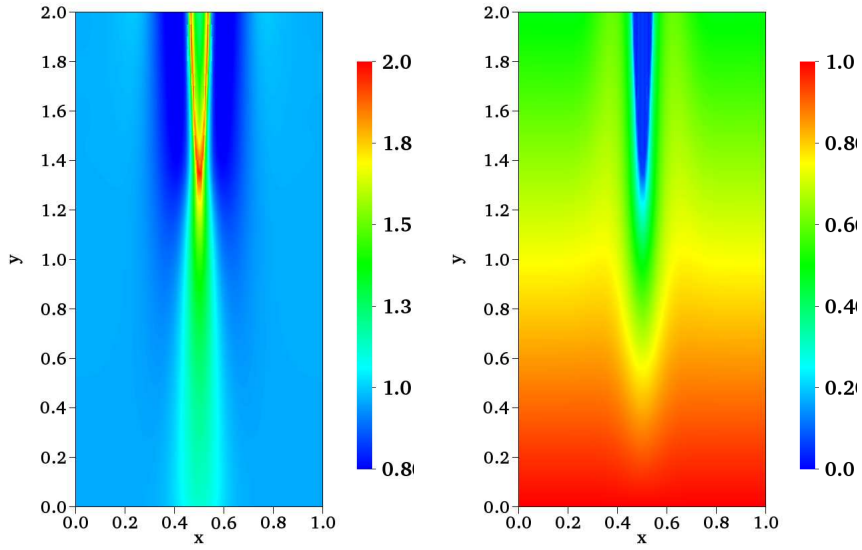


Figure 6.8: Steady state distributions of porosity and opx volume fractions with the variable viscosity formulation for $A = 0.2$.

If the solid flow is irrotational ($\nabla \times V = 0$) and because $\eta \ll \xi$ (i.e., bulk viscosity is much less than shear viscosity), (6.4) simplifies to

$$\phi_f(\mathbf{v} - \mathbf{V}) = -\frac{\kappa_\phi}{\mu}\{\nabla p - \triangle \rho g \mathbf{n}_z\} - \frac{\kappa_\phi}{\mu}\{\nabla \eta \cdot [\nabla \mathbf{V} + (\nabla \mathbf{V})^T - \frac{2}{3}\nabla \cdot \mathbf{V}\mathbf{I}]\}. \quad (6.5)$$

Substituting the above equation to (6.4), we get

$$\nabla \cdot [\frac{\kappa_\phi}{\mu}\{(\nabla p - \triangle \rho g \mathbf{n}_z) + (\nabla \eta \cdot [\nabla \mathbf{V} + (\nabla \mathbf{V})^T - \frac{2}{3}\nabla \cdot \mathbf{V}\mathbf{I}])\}] = \frac{\phi_f p}{\eta}. \quad (6.6)$$

Ignoring the symmetric tensor, we get

$$\nabla \cdot [\frac{\kappa_\phi}{\mu}\{(\nabla p - \triangle \rho g \mathbf{n}_z) + (\nabla \eta \cdot [-\frac{2}{3}\nabla . \mathbf{V}\mathbf{I}])\}] = \frac{\phi_f p}{\eta}. \quad (6.7)$$

Substituting the pressure term from the compaction rate,

$$\nabla \cdot [\frac{\kappa_\phi}{\mu}\{(\nabla p - \triangle \rho g \mathbf{n}_z) + ([-\frac{2}{3}\frac{\phi_f p}{\eta}]\nabla \eta)\}] = \frac{\phi_f p}{\eta}. \tag{6.8}$$

Empirically shear viscosity has been derived to be a function of porosity.

$$\eta(\phi) = \eta(0)\exp[-\alpha\phi] = \eta_0 \exp[-\alpha(\phi - \phi_0)], \tag{6.9}$$

where

$$\eta_0 = \eta(\phi_0) = \eta(0)\exp[-\alpha\phi_0],\ \alpha = 25. \tag{6.10}$$

In dimensionless variables, we have

$$\eta(\phi) = \eta_0 \exp[-\alpha\phi_0(\phi' - 1)]. \tag{6.11}$$

Non-dimensionalizing the above equation as in Chapter 2 and substituting the empirical formula for $\eta$, we recover

$$-\nabla \cdot [\phi_f^3 \nabla p] + \exp(\alpha\phi_{f_0}(\phi_f - 1))p\phi_f = -R\frac{\partial \phi_f^3}{\partial z}.$$

The governing equations for porosity, $\phi_f$ and opx, $\phi_{opx}$ remain the same. Figure 6.8 shows the steady state distribution of porosity and opx with the variable viscosity formulation. The coefficient of $p\phi_f$ is approximately equal to one and hence the first order characteristics of dunite channel formation should not significantly change when we consider variable viscosity. This can be seen from the plots of the difference of porosity and opx variation between variable viscosity and constant viscosity at steady state in Figure 6.9.

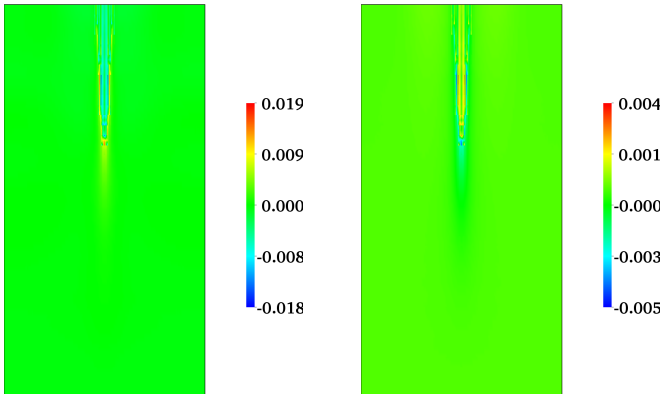


Figure 6.9: Difference of porosity distribution with variable and constant viscosity (left) and difference of opx distribution with variable and constant viscosity (right) at steady state for $A = 0.2$.

### 6.4.2 Reverse Solubility

The solubility can be considered to be a linear function of $z$ beneath the mid ocean ridge. But there are conditions where the solubility does not vary linearly with the depth but rather increases for a certain depth and then crystallization begins. If a domain away from the mid-ocean ridge is considered, then, as the melt reaches the surface, the temperature decreases and the rate of solubility decreases. Similarly regions of subduction can result in reverse solubility. The affects of reverse solubility can be modeled to first order by changing the governing equations only in the dissolution rate, $\Gamma_{opx}$. For the purpose of illustration, we consider a nonlinear solubility of the form

$$F(z) = A \sin\left[\pi \left(\frac{z}{z_{max}}\right)^{\alpha_F}\right], \tag{6.12}$$

where $A$ is the amplitude, $z_{max}$ is the column height, and $\alpha_F = 1, 2, 3$. The curves for the three cases of reverse solubility and linear solubility are shown in Figure 6.10

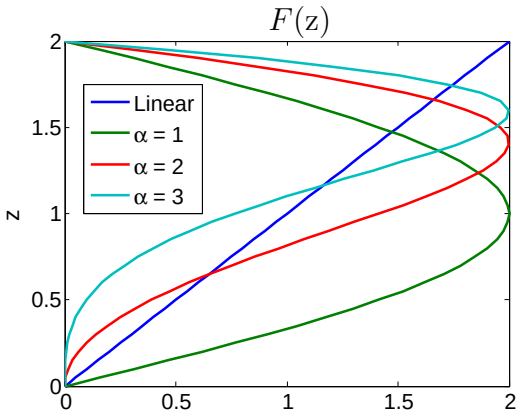


Figure 6.10: Profiles for linear and reverse solubilities

The dimensionless solubility is given by

$$\Gamma_{opx} = \frac{R\phi_f(\boldsymbol{V_f}.\boldsymbol{n_z})}{1-\delta F}\frac{dF}{dz}. \tag{6.13}$$

Reverse solubility affects the region of dunite channel formation. Unlike the linear solubility case where $F'(z) = 1$, reverse solubility results in solubility for a part of the domain and crystallization in other regions. Crystallization results in an increase in the opx fraction in the domain. The effects of reverse solubility are illustrated in Figure 6.11. Dunite channels are still formed but the dunite channel initiation is not at the top. Instead, dunite channels form in regions just before crystallization. Therefore, as $\alpha_F$ increases, the dunite channel forms closer to the top of the domain.

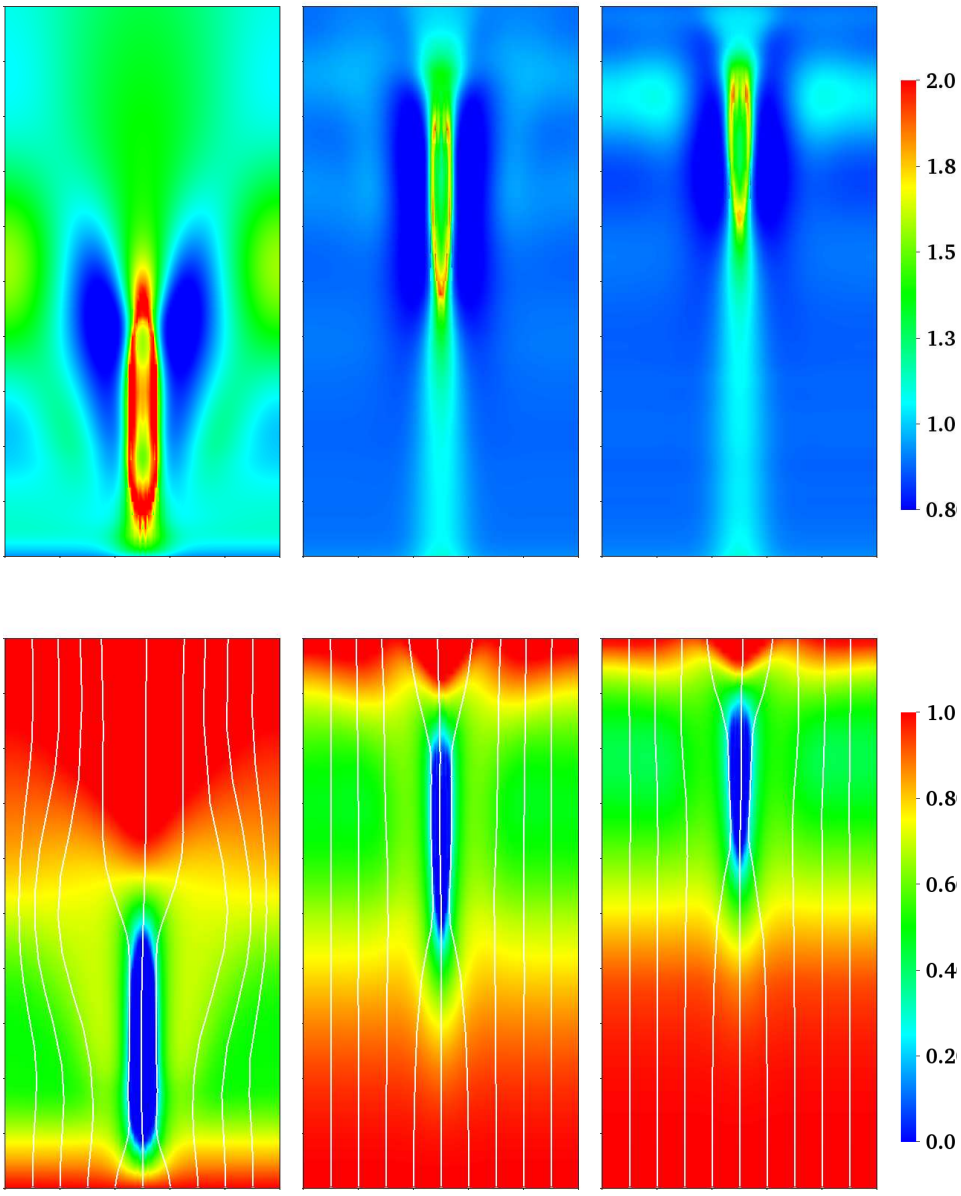


Figure 6.11: Porosity (top) and opx (bottom) distributions with reverse solubility in the domain $(x, z) \in [0, 1] \times [0, 2]$. From left to right $\alpha_F = \{1, 2, 3\}$.

# Chapter 7

# 3D Results

## 7.1 High-Porosity Channel Formation

### 7.1.1 Gaussian Perturbation

All the simulations reported so far are in simple 2D geometries. However, to compare with real field observations, we need to consider simulations in 3D. Extending the tensor product of Fourier collocation and discontinuous Galerkin method in 2D [52, 53] requires a substantial effort. The numerical analysis library, deal.ii, makes it very easy to extend our code from 2D to 3D as the flux terms are treated in a dimension independent manner where lines and surfaces can be easily interchanged. A variable mesh becomes all the more important in 3D to control the overall cost. With a variable mesh, the number of degrees of freedom are substantially less than a uniform grid with a collocation method in the x and y direction. These factors result in a substantial improvement over previous numerical methods to solve magma dynamics problems in 3D and allows us to present some of the first 3D results. Figure 7.1 shows the development of a tabular high-porosity dunite channel in 3D at three selected times and for the sustained inflow porosity

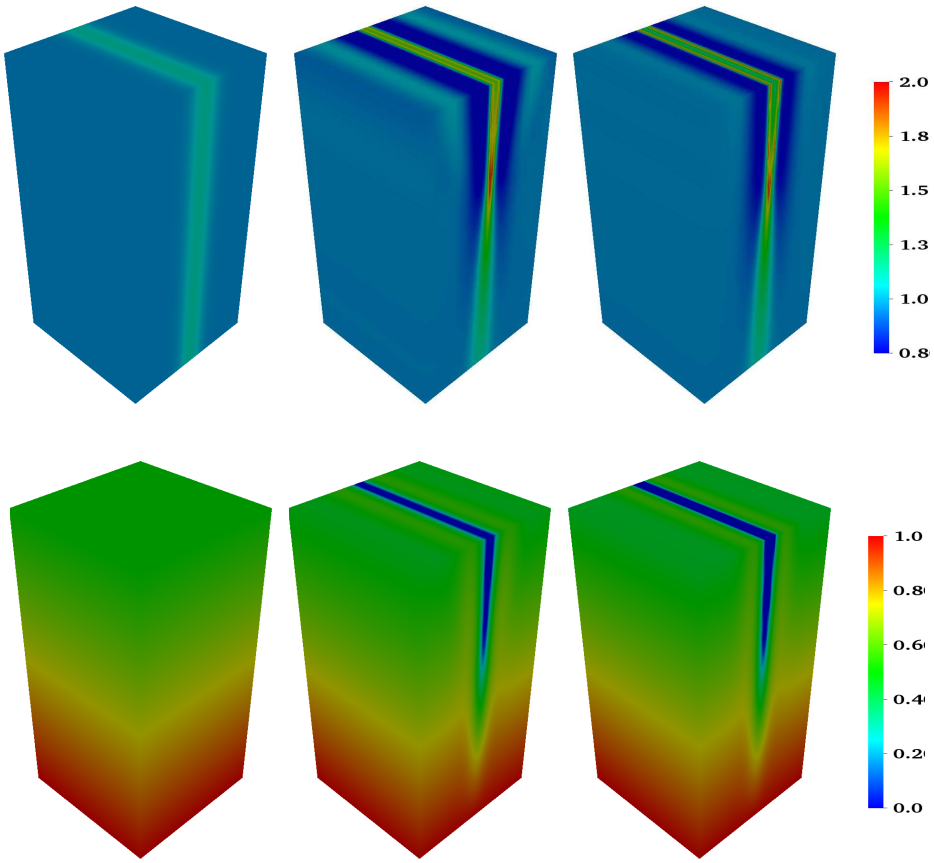


Figure 7.1: Distributions of porosity (top) and opx (bottom) volume fractions in channel regime with a Gaussian perturbation along x uniformly along y. From left to right $t = \{0.0, 1.2, 2.4\}$

$$\phi_f(x, y, 0, t) = 1 + 0.15 \exp(-100(x - \frac{x_{max}}{2})^2).$$

The computational domain for all channel regime simulations in 3D is $(x, y, z) \in [0, 1] \times [0, 1] \times [0, 2]$. Since the initial and boundary conditions are extended in the y direction (by one dimensionless unit), we observe the channel formation to be uniform along the y direction. Figure 7.1 shows that the channel geometry, compacting boundary layer (deep blue regimes outside the tabular channels), and melt channel bifurcation are well resolved. Steady state is established for $t > 2$. The degrees of freedom for this case are $704,000$ with a non-uniform mesh as compared

to a uniform mesh which would require $2,560,000$ degrees of freedom to recover the same channel features. In terms of physical features, the example shown in Figure 7.1 is effectively 2D. To further demonstrate the advantages of our numerical method and the importance of 3D simulations, we consider a simple 3D problem in a $1 \times 1 \times 2$ domain in which two sustained Gaussian perturbations in porosity at the inflow (bottom plane) are perpendicular to each other

$$\phi_f(x, y, 0, t) = 1 + 0.1 \exp(-100(x - \frac{x_{max}}{2})^2) + 0.1 \exp(-100(y - \frac{y_{max}}{2})^2).$$

From 2D analysis, we know that the amplitude and shape of the perturbation at the boundary strongly affects the formation and characteristics of dunites in the stable regime. Figure 7.2 shows that when the system reaches steady state, there is a deeper cylindrical shaped channel at the center because of the higher amplitude of the Gaussian perturbation and 4 tabular channels in x and y because of the perturbations in each dimension respectively. Figure 7.2 plots the snapshots of $\phi_f$ and $\phi_{opx}$ at 3 different times prior to the solution reaching steady state. The spatial distribution of high-porosity melt channels and dunite channels in the earth's interior is an important geological problem. Whether the 3D shape of dunite channels in the earth's interior is tabular or cylindrical and if they are correlated with inflow perturbation are still not known.

The effect of inflow melt flux can also be deduced from Figure 7.2. Opx dissolution rate is directly proportional to the vertical melt flux. The inflow melt flux at the center of the domain is higher ($A = 0.2$) and this larger amplitude in porosity perturbation leads to greater melt focusing and hence increasing melt flux which results in an increase in the magnitude of the opx dissolution term ($\Gamma_{opx}$). This increased melt dissolves opx faster and thus lowers the depth of the opx-free dunite channel initiation. The amplitude of the x and y perturbations away from the center of the domain are comparatively weaker and hence the melt flux that arises from this perturbation is also small. Thus, this only results in a shallower dunite channel. The

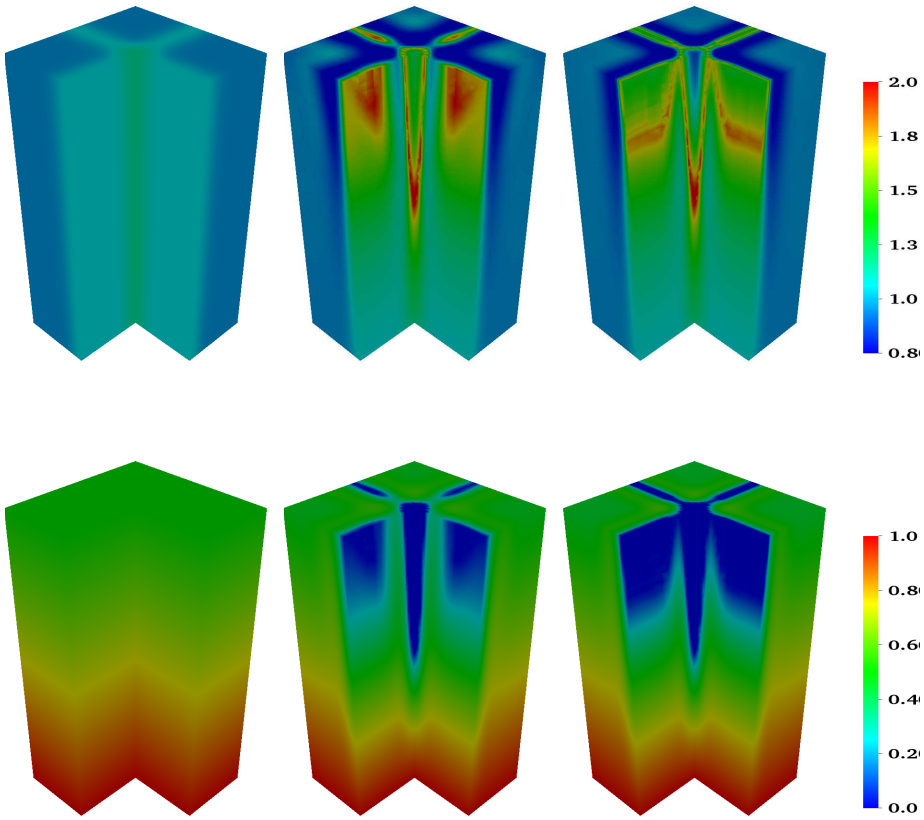


Figure 7.2: Distributions of porosity (top) and opx (bottom) volume fractions in channel regime with a Gaussian perturbation of amplitudes $A_1 = 0.1$ and $A_2 = 0.1$. From left to right $t = \{0.0, 1.2, 2.4\}$

resulting dunite channel at the center is deeper and wider with strong melt-channel bifurcation. It can also be observed that the separation distance between the Gaussian perturbations has an effect on the geometry of melt and dunite channels. The center region is composed of the Gaussian perturbations in both x and y directions ($A = A_1 + A_2 = 0.2$). Outside the center region, the amplitude of the perturbation is ($A_1 = A_2 = 0.1$). As the distance from the center increases, the depth of the dunite channel increases in both x and y directions respectively, and towards the boundary the channel formations are not influenced by the higher amplitude of the Gaussian

perturbation at the center. The dunite channel near the center is absorbed into the dunite channel at the center. Similarly, it can also be inferred from the dissolution term that deeper dunite channels are formed as the solubility gradient at the inflow increases. Plots of the compaction rate and dissolution rate for perturbations in x and y directions are shown in Figure 7.3.

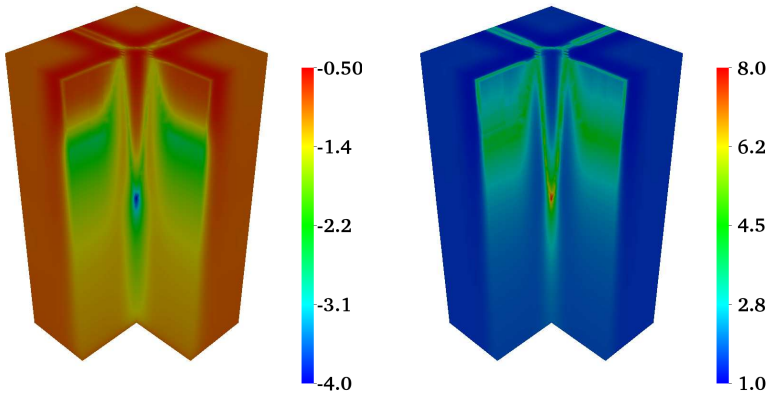


Figure 7.3: Steady state distributions of compaction rate, $\phi_f p$ and dissolution rate, $\delta\Gamma_{opx}$ with the same parameters as Figure 7.2.

### 7.1.2 Non-Gaussian Perturbation

While only Gaussian perturbations have been considered so far, the conclusions can be extended to any kind of perturbation. As an example, a combination of a sine function and Gaussian perturbation is considered.

$$\phi_f(x, y, 0, t) = 1 + 0.15 \sin(2\pi y) \exp(-100(x - \frac{x_{max}}{2})^2).$$

As discussed in the previous section, since the sine term results in a smooth change in the amplitude of the Gaussian perturbation in the y direction, the opx-free dunite channels get merged into one big channel for $0 \leq y \leq 0.5$, where $\sin(2\pi y)$ is positive. In the other half, melt influx at the boundary is less than the mean and this results

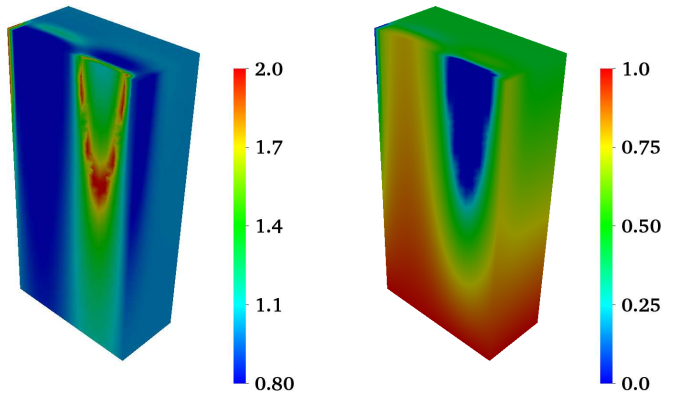


Figure 7.4: Steady state distributions of porosity and opx volume fractions for non-Gaussian perturbations in the y-direction.

in the melt focusing in the other half. The corresponding steady state solutions are presented in Figure 7.4

### 7.1.3 Time-Dependent Perturbations

To study the impact of time dependent boundary conditions on dunite channel formation, the following boundary conditions are considered:

$$\phi_f(x, y, 0, t) = 1 + 0.15 \exp(-100(x - \frac{x_{max}}{2})^2) + A_t \exp(-100(x - 0.3)^2),$$

where $A_t$ is 0.15 or zero alternately for every 20 time steps. Figure 7.5 shows the results for these perturbations. Even though the amplitude of the perturbation is the same at $x = 0.3, 0.5$, the constant influx of melt at $x = 0.5$ results in a deeper channel while the channel at $x = 0.3$ is weaker. The distance between the channels is large enough to not impact the depth of the dunite channels.

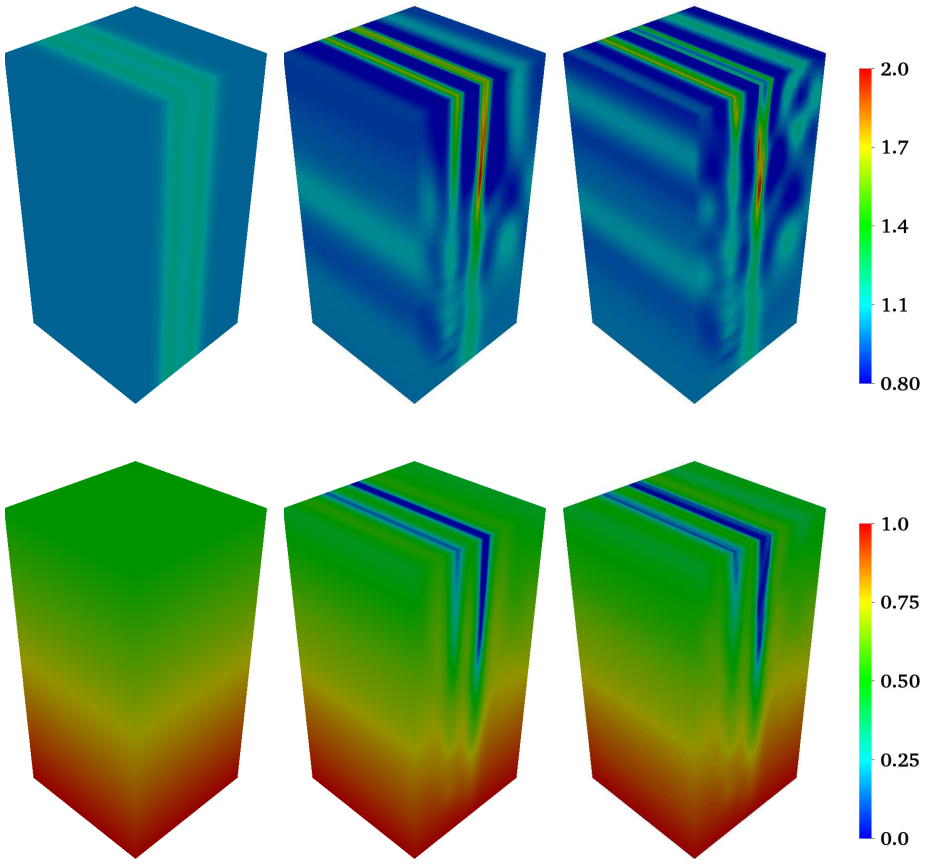


Figure 7.5: Distributions of porosity (top) and opx (bottom) volume fractions with time varying perturbation at $x = 0.3$ and a fixed Gaussian perturbation at $x = 0.5$. From left to right $\{t = 0.0, 1.2, 2.4\}$

### 7.1.4 Discussion

The first order characteristics and their associated lithology of the high-porosity melt channel system formed by reactive-dissolution has been studied in the previous sections. A number of field, petrological and geochemical observations can potentially be explained even from the simplified set up of the numerical simulations. Some of the key conclusions are:

1. Based on the streamlines of the velocity field, it can observed that opx-free dunite channels are transient and shallow parts of pathways for melt migration

in the mantle. The lower part of the high-porosity channel are opx-bearing dunite and harzburgite.

2. The depth of the dunite channel depends on a number of factors. Some of the factors considered in this thesis are inflow melt flux and strength of melt focusing. The geometry of the dunite channel is paraboloid or conic depending on the perturbation of melt influx. Although not covered in this section, it can be clearly seen that the melting rate and opx abundance also play an important role in dunite channel characteristics.

3. The amplitude of the lateral variation in porosity at the base of the upwelling column plays an important role in determining the shape and depth of the dunite channel, the strength of melt focusing and the presence of the compacting boundary layer. The variation in the distribution of porosity at the lower boundary can be attributed to the mantle heterogeneities that start to melt at a greater depth in the upwelling mantle.

4. Compaction and dissolution dictate the distribution of melt in and around the opx-free dunite channel. Melt channels can interact if the separation distance is smaller than the compacting boundary layer thickness.

## 7.2 Compaction-Dissolution Waves

Based on the linear stability analysis, as explained for $2D$ cases, there are certain parametric conditions for which compaction dissolution waves occur. Figure 2.2 gives the choice of values for the parameters for an instability resulting in waves. Studies like [27] indicate that this parameter regime might be favored beneath the mid-ocean ridges.

We consider reactive dissolution in a $3D$ domain with dimensions of $5.71 \times 5.71 \times 6.75$ compaction lengths. The initial conditions for the melt fraction and opx are

shown in Figure 7.6.

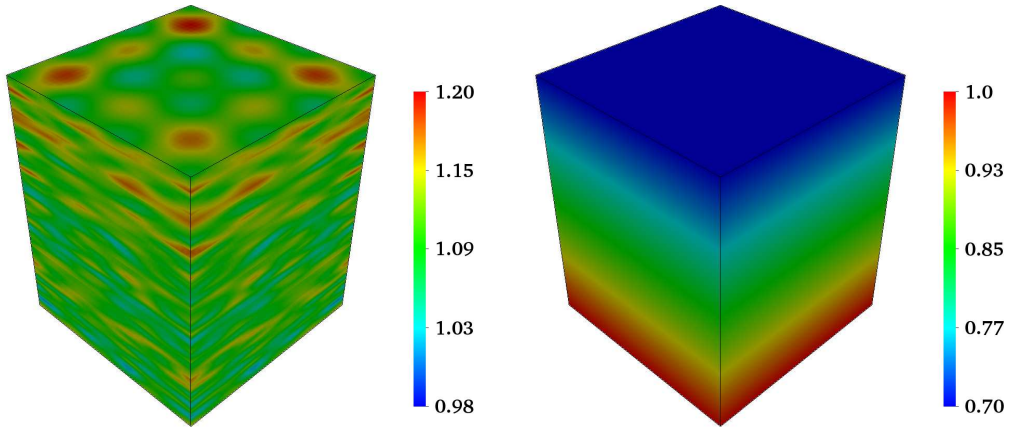


Figure 7.6: Initial conditions for porosity and opx fractions in the wave regime. The The average horizontal wavelength of 1.8 compaction lengths in $x$ and $y$ directions and 0.12 compaction lengths in the $z$ direction.

Infinitesimal perturbations of the melt fraction results in porosity waves. Figure 7.7 shows that well-organized wave patterns emerge after one solid overturn time. But it can be observed that the wave pattern is still weak after one overturn time as the amplitude of the waves is approximately constant. The amplitude of the perturbation grows with time and fully evolved compaction-dissolution waves are observed after 3 overturn times. The wave patterns are well organized in the lower part of the domain while the dunite channels that form at the top of the domain along the nodal lines of the waves cause the wave pattern to be irregular at the top. By the third overturn time, the dunite channels are organized in a checkerboard pattern. High porosity channels are initiated at the top and grow along the nodal lines of the waves. This results in the decrease of the opx abundance and the remaining opx abundance is further dissolved because of the localization of the melt into these channels. By the third overturn time, there are 36 well developed channels.

The wave pattern features and the dunite channel development can be better observed in the plots with a quadrant cut off in Figure 7.8 and the isosurface plots

shown in Figure 7.10. The downward growth of these channels strongly perturb the local melt field and this causes a disturbance in the regular wave pattern of the waves. These continuous nonlinear interactions between the compaction dissolution waves in the lower part and the channels in the upper part of the domain leads to the wavelengths in the $xy$ plane of the domain further decreasing. This can be observed in the Figure 7.9. As in 2D it can be expected that the redistribution of the wave pattern should again result in dunite channels formed along the nodal lines of the new wave structure but the numerical resolution does not capture these characteristics in 3D.

The shapes of dunite channels and organized pattern of the dunite channels is better visualized in the isosurface plots with $\phi_{opx} = 0$ which capture the dunite channels as shown in Figure 7.11.

The next important question to consider is the pathways of melt migration. This can be visualized in the Figures 7.12 and 7.13. For the first two overturn times, the flow is nearly vertical and the horizontal gradients and wave patterns are not strong enough for the melt to change direction. But as the waves become stronger, the melt flows in a coiled path. This can be inferred from Figure 7.12, where the streamlines are curved when observed with x-direction as a normal (top) or y-direction as normal (bottom). The coiled streamlines pattern is not regular at the top because of the interactions of the melt with dunite channels. From Figure 7.13, it can be observed that the melt tries to flow through the dunite channels at the top. This makes it deviate from the symmetric coiled structure at the bottom of the domain.

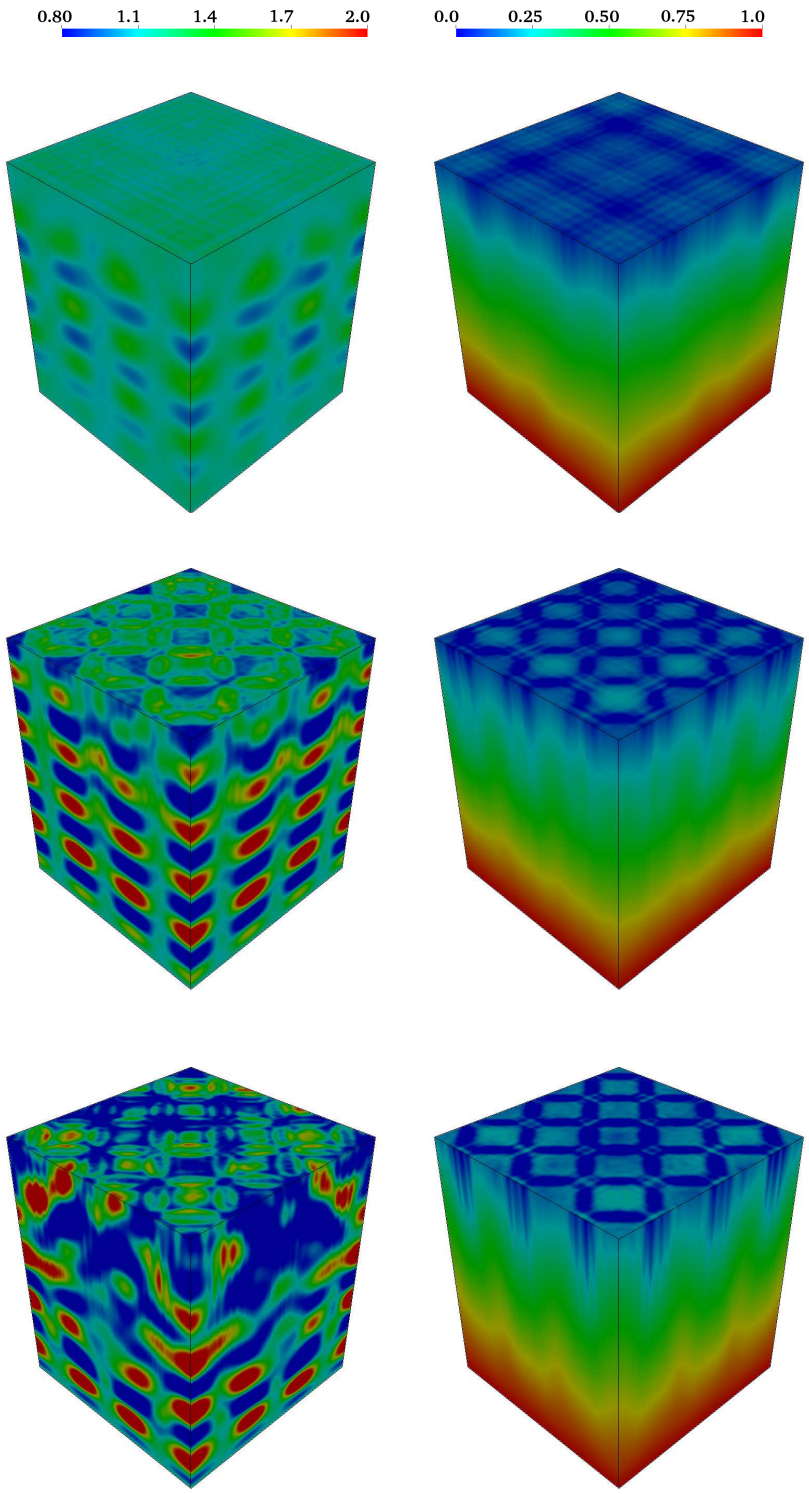


Figure 7.7: Distributions of porosity (left) and opx (right) volume fractions at three selected times after the initiation of waves in the domain. From left to right $\{t = 9.2, 16.8, 20.0\}$. It can be seen that the waves become stronger from one overturn to three overturns.

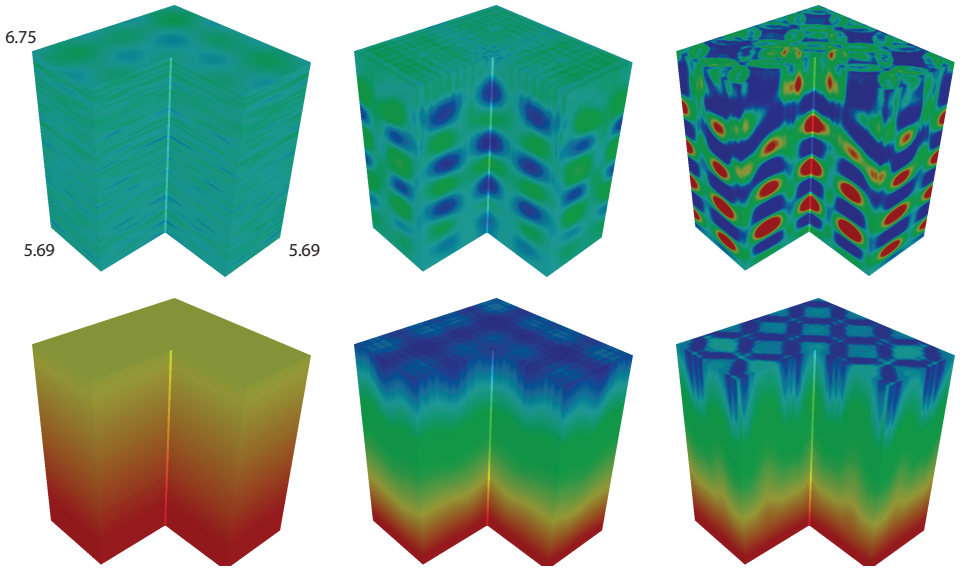


Figure 7.8: Porosity (top) and opx (bottom) volume fractions with a quadrant cut off to see the the wave pattern inside the domain.

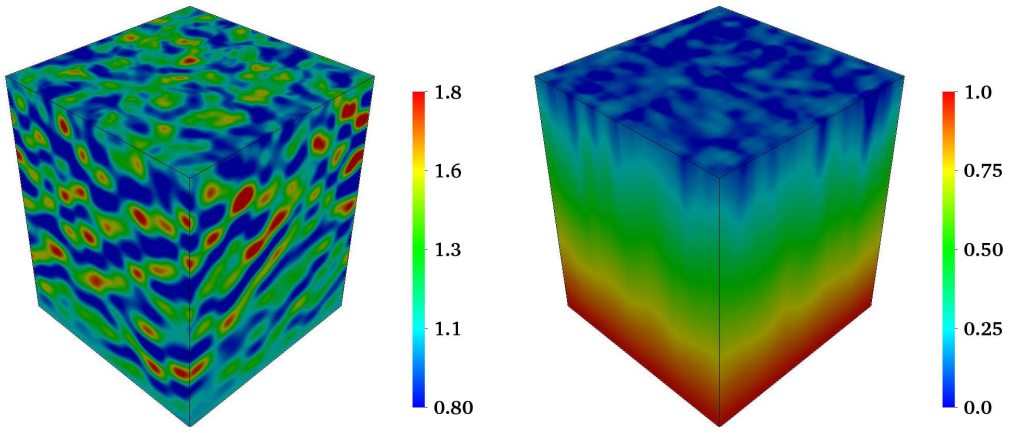


Figure 7.9: Porosity and opx fields after 7 overturns with the average horizontal wavelength decreasing from the average wavelength observed at 3 overturns. The dunite channels redistribute from the crossboard pattern after 3 overturns.

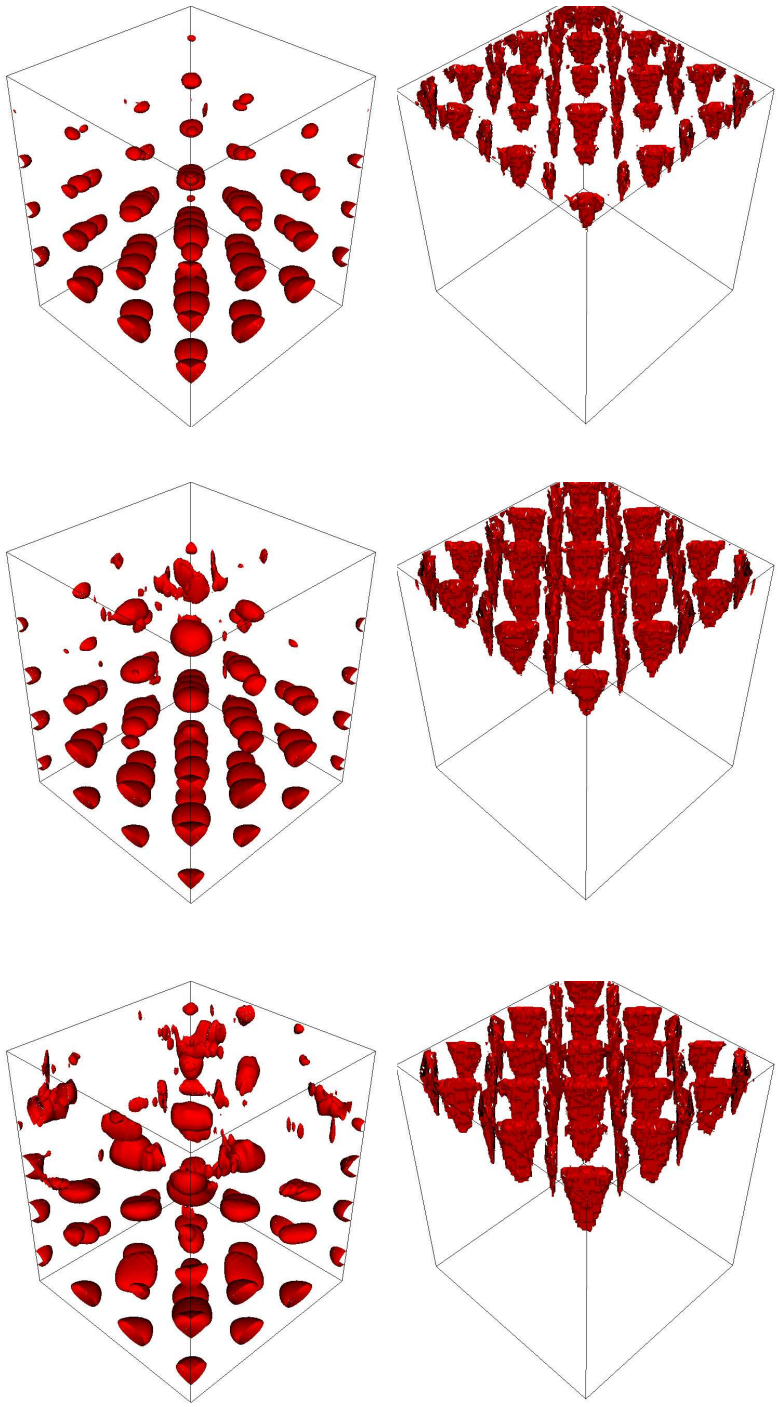

Figure 7.10: Contour plots of porosity and opx for the same timestamps as Figure 7.7. It can be seen that the wave patterns are regular throughout the domain and as the dunite channels get deeper (bottom panel), the interaction with the flow field causes the porosity field to redistribute.

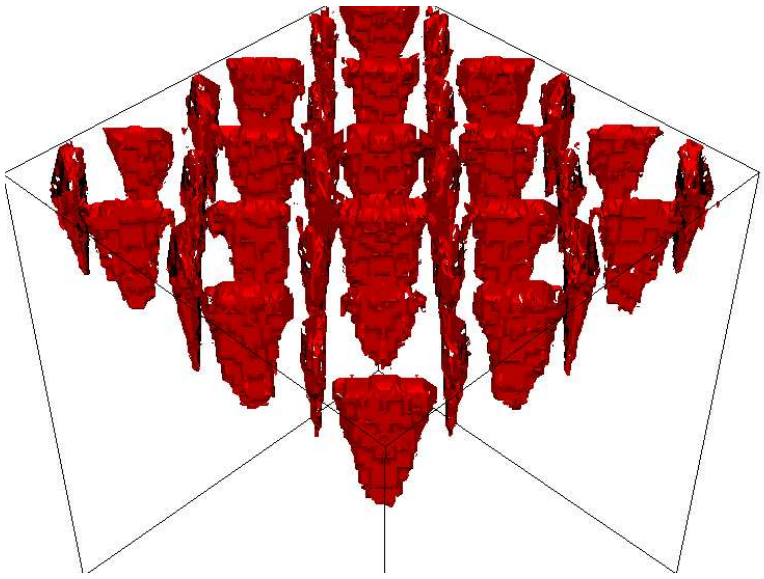

Figure 7.11: Dunite channel distribution in the domain after 3 overturn times

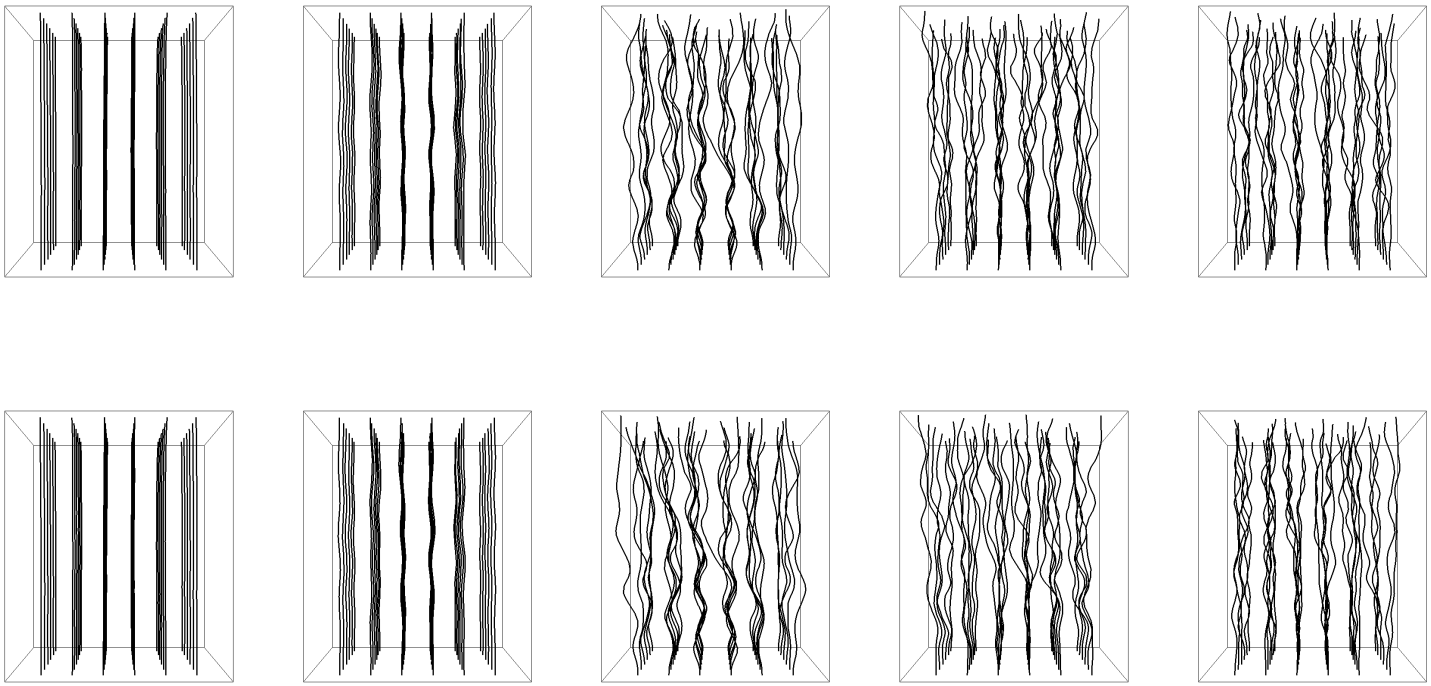

Figure 7.12: Streamlines normal to the x-axis (top) and normal to the y-axis (bottom). Streamlines are initially vertical but as the wave patterns become stronger the melt starts to move up in coiled pathways. From left to right $\{t = 0, 9.2, 20, 29.0, 40.0\}$

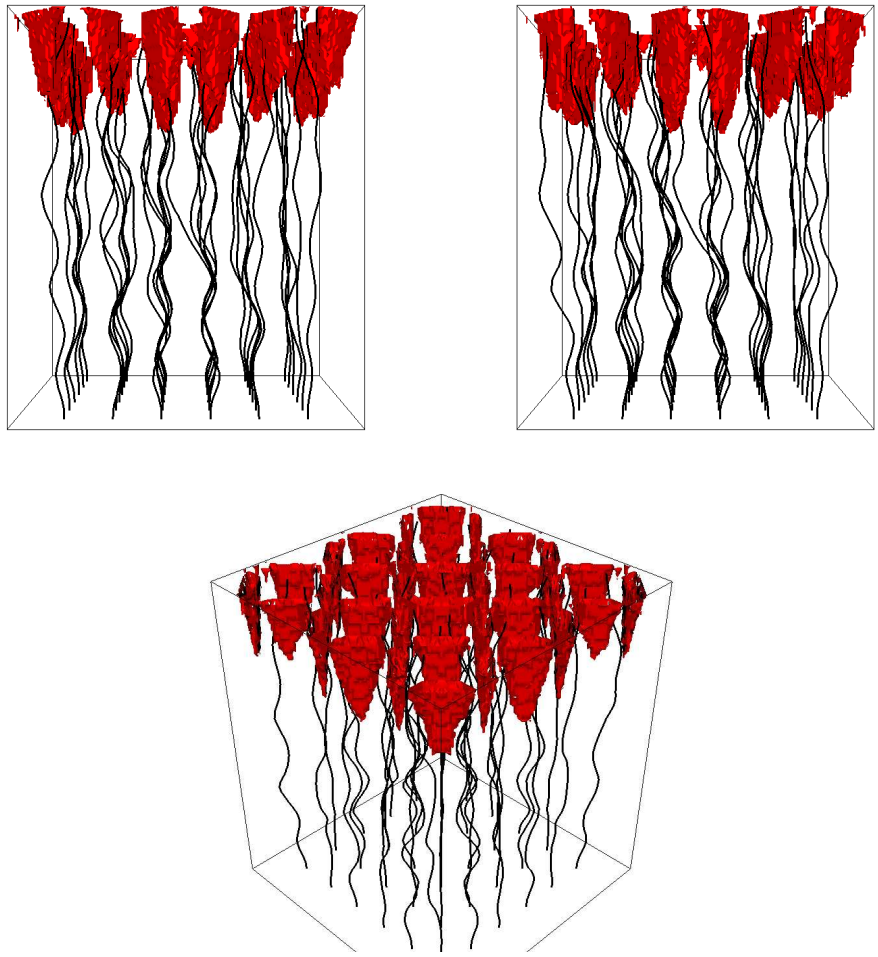

Figure 7.13: Streamlines at $t = 20.0$, it can be observed that the streamlines follow a regular pattern in the bottom half of the domain but tend towards the dunite channels when reaching the top.

# Chapter 8

# Shearing, Temperature and Permeability Effects on Dunite Channel Formation

There are many other factors that affect dunite channel formation apart from the factors considered so far i.e. compaction, dissolution, solid upwelling and buoyancy driven melt migration. If a domain is considered at the same depth as what has been considered so far but away from the mid-ocean ridge axis, shearing (a continuous deformation of the solid matrix) and corner flow become important. In these cases, the melt flow diverges from the solid flow direction as one moves away from the mid-ocean ridge axis. The impact on the shape of dunite channels and the orientation of dunite channels with respect to solid and melt flow fields are important questions to consider.

Dissolution and compaction are the two factors by which the solid transforms into fluid. Melting is the third important factor that can result in a phase change and this factor has not been considered so far. Melting primarily occurs due to temperature gradient whereas the primary driving force for dissolution is the gradient in chemical potential (or concentration) [62]. The stabilizing affect of matrix melt-

ing on the formation of unstable dissolution channels was first noted in [59]. This important observation has recently been confirmed by Hewitt [31] through simple analysis (without dissolution). The stabilizing effect of matrix melting can be overcome by a flux of melt focused from upstream [31]. The latter can be induced by deformation, freezing along a sloping boundary, corner flow or the presence of mantle heterogeneity.

These two important factors of melt migration will be considered in the next two sections. These are preliminary results and this chapter is mainly intended to provide a reference and framework for exploring these two aspects in depth in the future.

## 8.1 Shearing Effect

The conceptual model which indicates the region of interest where shear is important is shown in Figure 8.1. The effects of shearing in this setting will be considered in this section.

Following the procedure in Chapter 2, the conservation equations are given by:

$$\frac{\partial \phi_f}{\partial t} + \nabla \cdot (\phi_f \boldsymbol{V_f}) = (1-\beta)\Gamma_{opx}, \tag{8.1}$$

$$\frac{\partial (1-\phi_f)}{\partial t} + \nabla \cdot ((1-\phi_f) \boldsymbol{V_s}) = -(1-\beta)\Gamma_{opx}, \tag{8.2}$$

$$\frac{\partial \phi_{opx}}{\partial t} + \nabla \cdot (\phi_{opx} \boldsymbol{V_s}) = (-\beta)\Gamma_{opx}, \tag{8.3}$$

$$\phi_f(\boldsymbol{V_f} - \boldsymbol{V_s}) = -\frac{\kappa_\phi}{\mu}\left\{\nabla p + \eta\left[\frac{4}{3}\nabla(\nabla \cdot \boldsymbol{V_s} - \nabla \times \nabla \times \boldsymbol{V_s})\right] - \Delta\rho g \boldsymbol{n_z}\right\}, \tag{8.4}$$

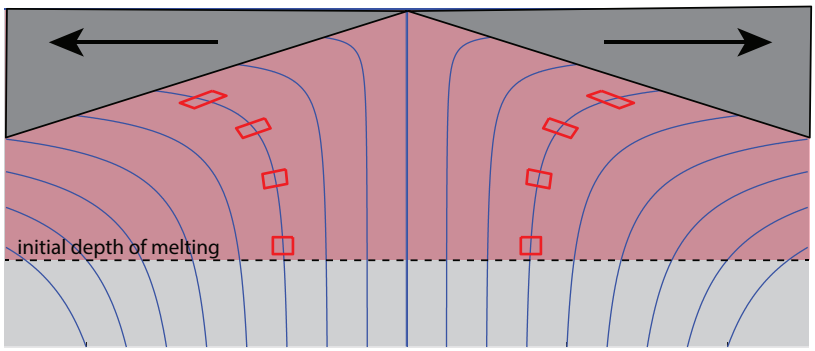


Figure 8.1: Conceptual model that is considered for the numerical model. The rectangular region is the domain of interest.

$$p = p_f - p_s = \psi \nabla \cdot \boldsymbol{V_s} = \frac{\eta}{\phi_f} \nabla \cdot \boldsymbol{V_s}. \tag{8.5}$$

We first derive the generalized Helmholtz equation. From equations (8.1) and (8.2), we have

$$\nabla \cdot [(\phi_f \boldsymbol{V_f} + (1 - \phi_f)\boldsymbol{V_s})] = \nabla \cdot [\boldsymbol{V_s} + \phi_f(\boldsymbol{V_f} - \boldsymbol{V_s})] = 0. \tag{8.6}$$

Substituting (8.4) into (8.6), we get

$$\nabla \cdot \left\{ \boldsymbol{V_s} - \frac{\kappa_\phi}{\mu} \left\{ \nabla p + \eta \left[ \frac{4}{3} \nabla (\nabla \cdot \boldsymbol{V_s} - \nabla \times \nabla \times \boldsymbol{V_s}) \right] - \Delta \rho g \boldsymbol{n_z} \right\} \right\} = 0. \tag{8.7}$$

Since $p = \xi \nabla \cdot \boldsymbol{V_s}$

$$\nabla \cdot \left\{ \frac{\kappa_\phi}{\mu} \left\{ \nabla \left[ (\xi + \frac{4}{3}\eta) + \nabla \cdot \boldsymbol{V_s} \right] - \eta \nabla \times \nabla \times \boldsymbol{V_s} - \Delta \rho g \boldsymbol{n_z} \right\} \right\} = \frac{p}{\xi}. \tag{8.8}$$

Using the identity $\nabla \times \nabla \times \boldsymbol{V_s} = \nabla(\nabla \cdot \boldsymbol{V_s}) - \nabla^2 \boldsymbol{V_s}$, we have

$$\nabla \cdot \left\{ \frac{\kappa_\phi}{\mu} \left\{ \nabla \left[ (\xi + \frac{1}{3}\eta) + \nabla \cdot \boldsymbol{V_s} \right] + \eta \nabla^2 \boldsymbol{V_s} - \Delta \rho g \boldsymbol{n_z} \right\} \right\} = \frac{p}{\xi}. \tag{8.9}$$

When the porosity is small, $\xi + \frac{1}{3}\eta : \xi$, we have

$$\nabla \cdot \left[ \frac{\kappa_\phi}{\mu} \left( \nabla p + \eta \nabla^2 \boldsymbol{V_s} - \Delta \rho g \boldsymbol{n_z} \right) \right] = \frac{p}{\xi}, \tag{8.10}$$

which can also be written as

$$\nabla \cdot \left[ \frac{\kappa_\phi}{\mu} \left( \nabla p - \Delta \rho g \boldsymbol{n_z} \right) \right] = \frac{p}{\xi} - \nabla \cdot \left( \frac{\eta \kappa_\phi}{\mu} \nabla^2 \boldsymbol{V_s} \right), \tag{8.11}$$

or equivalently

$$\nabla \cdot \left[ \frac{\kappa_\phi}{\mu} \left( \nabla p - \Delta \rho g \boldsymbol{n_z} \right) \right] = \frac{p}{\xi} - \frac{\eta \kappa_\phi}{\mu} \nabla \cdot \left( \nabla^2 \boldsymbol{V_s} \right) - \frac{\eta}{\mu} \nabla \kappa_\phi \cdot \nabla^2 \boldsymbol{V_s}. \tag{8.12}$$

Now, $\nabla \cdot (\nabla^2 \boldsymbol{V_s}) = \nabla^2 \left( \frac{p}{\xi} \right)$

$$\nabla \cdot \left[ \frac{\kappa_\phi}{\mu} \left( \nabla p - \Delta \rho g \boldsymbol{n_z} \right) \right] = \frac{p}{\xi} - \frac{\eta \kappa_\phi}{\mu} \nabla^2 \left( \frac{p}{\xi} \right) - \frac{\eta}{\mu} \nabla \kappa_\phi \cdot \nabla^2 \boldsymbol{V_s}, \tag{8.13}$$

which is further simplified as

$$\frac{\kappa_\phi}{\mu} \nabla^2 p + \frac{1}{\mu} \nabla \kappa_\phi \cdot \nabla p = \frac{p}{\xi} + \nabla \cdot \left[ \frac{\kappa_\phi \Delta \rho g \boldsymbol{n_z}}{\mu} \right] - \frac{\eta \kappa_\phi}{\mu} \nabla^2 \frac{p}{\xi} - \frac{\eta}{\mu} \nabla \kappa_\phi \cdot \nabla^2 \boldsymbol{V_s}, \tag{8.14}$$

$$\frac{\kappa_\phi}{\mu} \nabla^2 (1 + \phi_f) p + \frac{1}{\mu} \nabla \kappa_\phi \cdot \nabla p = \frac{p}{\xi} + \nabla \cdot \left[ \frac{\kappa_\phi \Delta \rho g \boldsymbol{n_z}}{\mu} \right] - \frac{\eta}{\mu} \nabla \kappa_\phi \cdot \nabla^2 \boldsymbol{V_s}, \tag{8.15}$$

We get the final generalized version of the Helmholtz equation by again taking the small porosity approximation

$$\nabla . \left[ \frac{\kappa_\phi}{\mu} (\nabla p - \Delta \rho g \boldsymbol{n_z}) \right] = \frac{\phi_f p}{\eta} - \frac{\eta}{\mu} \nabla \kappa_\phi \cdot \nabla^2 \boldsymbol{V_s}, \tag{8.16}$$

$$\phi_f (\boldsymbol{V_f} - \boldsymbol{V_s}) = -\frac{\kappa_\phi}{\mu} \left\{ \nabla p + \eta \nabla^2 \boldsymbol{V_s} - \Delta \rho g \boldsymbol{n_z} \right\}. \tag{8.17}$$

Non-dimensionalizing the conservation equations and the modified Helmholtz equation with the same scaling parameters as in Chapter 2, we get the final governing set of equations.

$$\frac{\partial \phi_f}{\partial t} + \boldsymbol{V_s} \cdot \nabla \phi_f = \phi_f p + \delta \Gamma_{opx}, \tag{8.18}$$

$$\frac{\partial \phi_{opx}}{\partial t} + \boldsymbol{V_s} \cdot \nabla \phi_{opx} = -\phi_f^0 \phi_{opx} \phi_f p - \frac{\phi_f^0}{\phi_{opx}^0} \frac{\delta}{(1-\beta)} \Gamma_{opx}, \tag{8.19}$$

$$\nabla \cdot \left[ \phi_f^n (\nabla p - R \boldsymbol{n_z}) \right] = \phi_f p - \phi_f^n \nabla^2 \boldsymbol{V_s}, \tag{8.20}$$

$$\phi_f \left( \boldsymbol{V_f} - \frac{1}{R} \boldsymbol{V_s} \right) = -\frac{1}{R} \phi_f^n (\nabla p + \nabla^2 \boldsymbol{V_s} - R \boldsymbol{n_z}). \tag{8.21}$$

### 8.1.1 Numerical Discretization

Following the discussion and setup of numerical discretization in Chapter 3, we get the following weak forms of the governing equations,

$$\int_{D^k} v_h \partial_t \phi_{f_h}^k d\mathbf{x} - \int_{D^k} \phi_{f_h}^k \boldsymbol{V_s} \cdot \nabla v_h d\mathbf{x} = - \oint_{\partial D^k} v_h (\phi_{f_h}^k)^* \mathbf{n}_e . \mathbf{V_s} d\mathbf{x} + \int_{D^k} v_h p \phi_{f_h}^k d\mathbf{x} + \int_{D^k} \delta v_h \Gamma_{opx_h}^k d\mathbf{x} + \int_{D^k} v_h \nabla \cdot \boldsymbol{V_s} d\mathbf{x}, \tag{8.22}$$

which gives the weak form of the porosity equation. The last term on the right hand side is the only extra term that emerges by rewriting the governing equation in conservation form before multiplying the equation with test functions. Similarly, the weak form of the opx equation is given by:

$$\int_{D^k} v_h \partial_t \phi_{opx_h}^k d\mathbf{x} - \int_{D^k} \phi_{opx_h}^k \boldsymbol{V_s} \cdot \nabla v_h d\mathbf{x} = - \oint_{\partial D^k} v_h (\phi_{opx_h}^k)^* \mathbf{n}_e . \mathbf{V_s} d\mathbf{x} - \int_{D^k} \frac{\phi_f^0}{\phi_{opx}^0} \frac{\delta}{(1-\beta)} v_h \Gamma_{opx_h}^k d\mathbf{x} + \int_{D^k} v_h \nabla \cdot \boldsymbol{V_s} d\mathbf{x}, \tag{8.23}$$

The discretized form of the pressure equation is the same as in Chapter 3.

$$\sum_{k\in\Omega_h}\int_k \phi_f^3\nabla p.\nabla v_h + \int_\Omega \phi_f p v_h + \epsilon\sum_{e\in\partial D_{in}\cup\partial\Omega_d}\int_e \{\phi_f^3\nabla v_h.\mathbf{n}_e\}[p] - \sum_{e\in\partial D_{in}\cup\partial\Omega_d}\int_e \{\phi_f^3\nabla p.\mathbf{n}_e\}[v_h] + \sigma\sum_{e\in\partial D_{in}\cup\partial\Omega_d}\int_e [p][v_h]$$
$$= \int_\Omega -R\frac{\partial\phi_f^3}{\partial z}v_h + \sum_{e\in\partial\Omega_d}\int_e(\epsilon\phi_f^3\nabla v_h.\mathbf{n}_e + \sigma_e v_h)g_D + \sum_{k\in\Omega_h}\int_k \phi_f^n\nabla^2\boldsymbol{V_s}v_h. \tag{8.24}$$

### 8.1.2 Parameters and Boundary Conditions

In order to study the fundamental process of melt migration with shearing and its impact on dunite channel formation, we first focus on the $2D$ behavior induced by a sustained Gaussian perturbation in porosity at the inflow boundary of the domain.

$$\phi_f(x,0,t) = 1 + A\exp(-100(x - x_{max}/2)^2),$$

$$\phi_{opx}(x,0,t) = 1,$$

$$p(x,0,t) = -\frac{\delta(1+R)}{1+nR}.$$

Periodic boundary conditions are prescribed at left and right boundaries and a zero Neumann boundary condition at the top. The background solid velocity due to shearing is prescribed using a simple linear model, i.e,

$$\boldsymbol{V_s} = (\gamma z, 1),$$

where $\gamma$ is the shear rate. When $\gamma = 0$, it corresponds to the case of uniform upwelling mantle flow as discussed in Chapter 6.

### 8.1.3 Numerical Results

Consider a domain $(x, z) \in [0, 6] \times [0, 3]$ with shear rate, $\gamma = 0.5$. Unlike, the case with no shear, there is an alternating pattern of compacted regions and the shearing of dunite channel increases with time. Since the matrix moves away with time, the channel becomes weaker. Figure 8.2 shows the time evolution of melt and opx fractions with time. Referring to [5], it has also been observed that the dunite channels are effected by the mantle heterogeneity and the boundary perturbations. It can also be observed from Figure 8.3, that the dunite channels form along the streamlines of the solid matrix. Other conclusions on the effect of shearing on dunite channels are listed below:

- Shearing tends to rotate the dissolution channels away from the vertical. This reduces the component of buoyancy acting along the channels and consequently decreases the stability of the channel.

- Compaction on the downstream side of the channel generates a region of reduced porosity which advects with the velocity of the matrix. Melt that collects under the compacting region generates new melt channels at an angle corresponding to the shear rate.

- In the shear, melt rising vertically in the melt channel remains within the mantle matrix. Horizontal shearing destroys this isolation by causing the melt to flow horizontally relative to the matrix.

- Dunite channel forms in the direction of the shear, and the channels are deeper for stronger porosity and weaker shearing in the solid matrix.

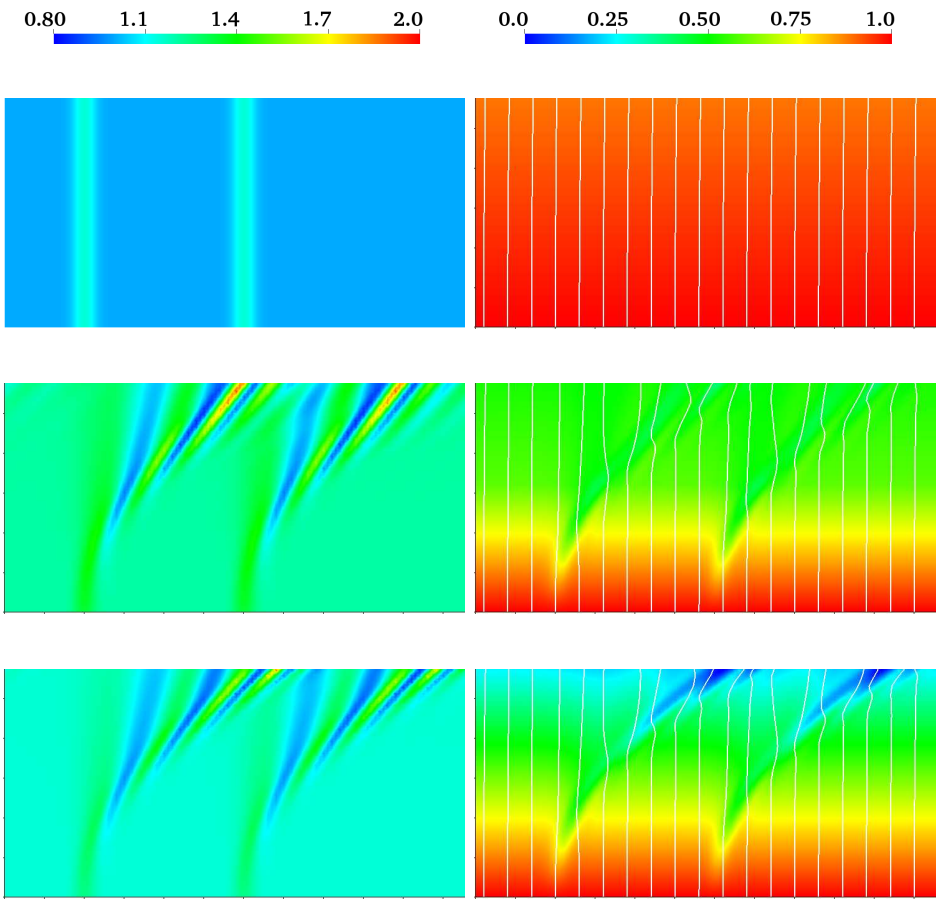


Figure 8.2: Effect of matrix shear on dunite channel formation. Shearing rotates the channel in the direction of the shear. Computational domain is $(x, z) \in [0, 6] \times [0, 3]$.

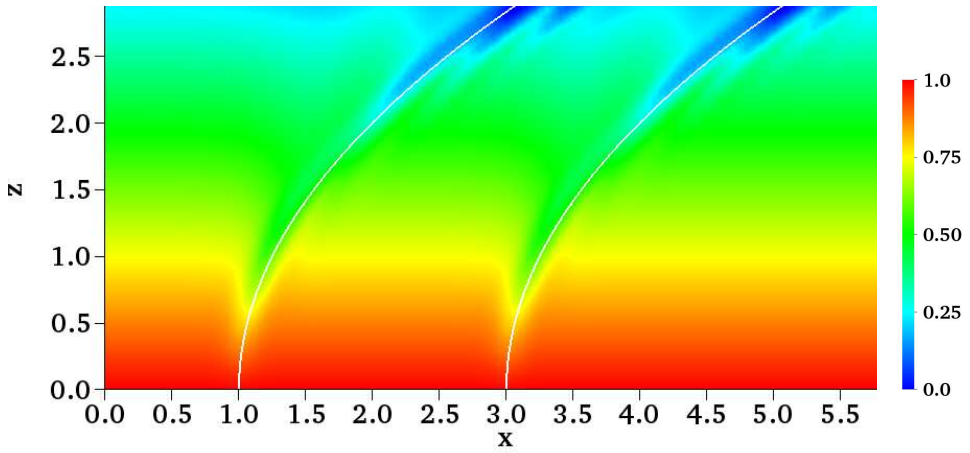


Figure 8.3: Distribution of opx fraction in steady state. The white lines are the streamlines of solid matrix originating from the centers of perturbation.

## 8.2 Temperature Dependence

The governing equations can be derived using the conservation laws following the procedure similar to the set of governing equations derived in Chapter 2 . The conservation laws for melt and opx remain the same. But the temperature dependence of the solution now results in an additional governing equation. The dissolution rate incorporates the influence of temperature too,

$$\frac{\partial \phi_f}{\partial t} = -\frac{\partial \phi_f}{\partial z} + \phi_f p + \delta \Gamma_{opx}, \tag{8.25}$$

$$\frac{\partial \phi_{opx}}{\partial t} = -\frac{\partial \phi_{opx}}{\partial z} - \frac{\phi_f^0}{\phi_{opx}^0}\frac{\delta}{(1-\beta)}\Gamma_{opx}, \tag{8.26}$$

$$-\nabla.[\phi_f^3 \nabla p] + \phi_f p = -R\frac{\partial \phi_f^3}{\partial z}, \tag{8.27}$$

$$\frac{\partial T}{\partial t} + [\phi_f^0 R \phi_f \mathbf{v} + \mathbf{n_z}] \cdot \nabla T = \frac{1}{P_e^T}\nabla^2 T + \frac{\phi_f^0 \delta St}{1-\beta}\Gamma_{opx}, \tag{8.28}$$

$$\Gamma_{opx} = \frac{R\phi_f \mathbf{v} \cdot [\mathbf{n}_z + \epsilon(1-\phi_f^0\phi_f)\nabla T] + \frac{\epsilon}{P_e^T}\phi_f \nabla^2}{1-\delta(z+\epsilon T) - \epsilon\delta\phi_f^0\phi_f St/(1-\beta)}\mathcal{I}_{opx}. \tag{8.29}$$

Here, $\mathcal{I}_{opx}$ is the same indicator function as defined before. Equations (8.25)-(8.28) are discretized and solved using DG methods. LSERK methods were used to progress the solution in time. A preliminary study of the computational results are presented in Figure 8.4. The model runs smoothly until channel formation as can be seen in the figure, but when the dunite channels are formed, the sharp gradient in $\phi_f$ which in turn affects the fluid velocity, $\mathbf{v}$ can cause numerical issues. The other aspect that needs to be worked on in handling convection diffusion problems is the issue of time stepping. The diffusion term results in the time step that scales as

$$\Delta t \sim \frac{1}{\lambda_{max}\frac{N^2}{h} + ||\frac{1}{P_e^T}||_L^\infty \frac{N^4}{h^2}}, \tag{8.30}$$

where $\lambda_{max}$ is the largest characteristic velocity and the Peclet number $P_e^T$ is the magnitude of the viscosity, $h$ is the local mesh size and $N$ is the degree of the DG polynomial [30] and hence the diffusion term can put a severe restriction on the time step. Even though explicit Runge Kutta methods were used in this thesis, future work should consider other alternatives like Implicit-Explicit Runge-Kutta Methods [4].

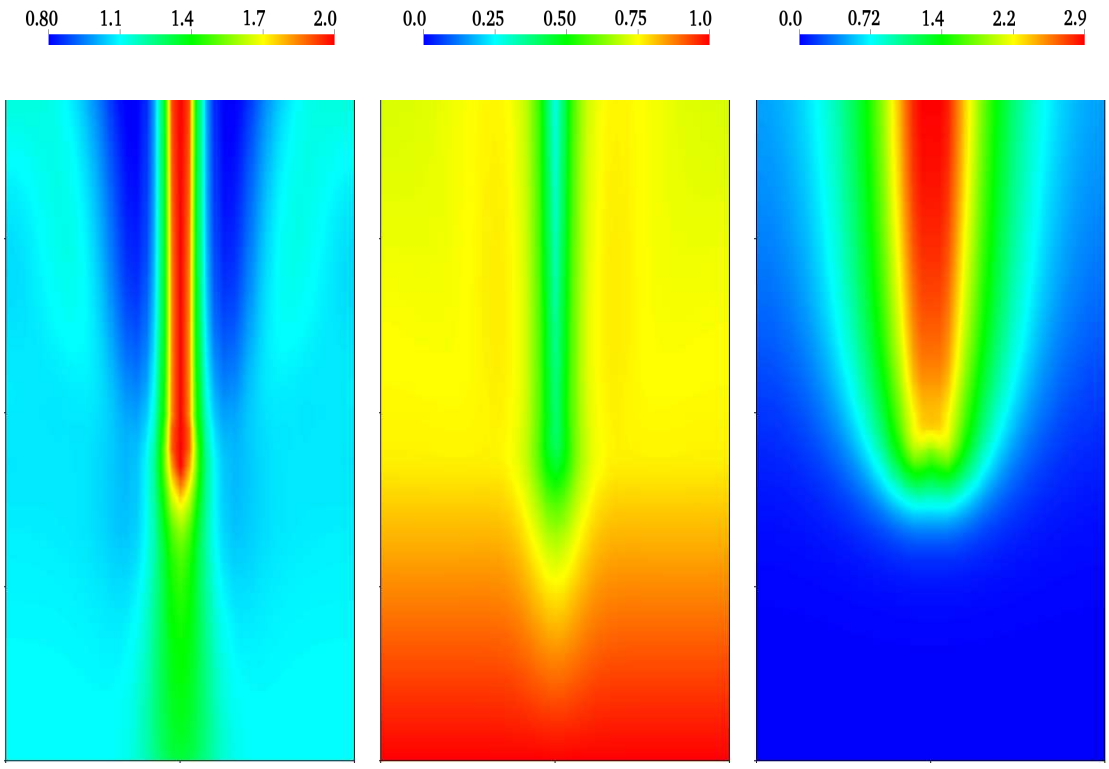


Figure 8.4: Distribution of melt fraction, opx fraction and temperature at $t = 0.86$ using $2^{nd}$ degree DG polynomials and 800 cells in a $1 \times 2$ domain.

## 8.3 Anisotropic Permeability

In order to extend the formulation of melt migration to more realistic situations, it is important to consider a domain which is not homogeneous. This results in a situation where the permeability varies between the horizontal and the vertical. This is known as anisotropic permeability. Two cases of anisotropic permeability are considered.

- $$\mathbf{K} = \begin{pmatrix} 1 & 0 \\ 0 & 0.25 \end{pmatrix}$$

- $$\mathbf{K} = \begin{pmatrix} 0.25 & 0 \\ 0 & 1 \end{pmatrix}$$

The pressure equation now changes to

$$-\nabla \cdot [\mathbf{K}\phi_f^3 \nabla p] + \phi_f p = -R\frac{\partial \phi_f^3}{\partial z}. \tag{8.31}$$

Anisotropic permeability seems to radically change the nature of instabilities in the wave regime. One can observe that when the x-directional permeability, $k_x$, is 4 times the z-directional permeability, there are no waves formed. The flow is more or less vertical as can be seen from the streamlines in Figure 8.5. This can probably be explained from the fact that there is no melt focusing when the permeability in the x direction is higher. But on the contrary when the z-directional permeability is higher, as in Case-2, then the flow is nearly vertical but wave patterns emerge over time. The wavelengths of these waves as compared to the isotropic case are much smaller because of the weaker permeability in the x-direction which leads to a reduction in the horizontal compaction length. These wave patterns dominate over time and the streamlines deviate substantially from their point of origin. Further investigation is necessary to study the wave characteristics with anisotropic permeability. Linear stability analysis with anisotropic permeability should validate the results obtained in these simulations. Higher resolution is required to capture the dunite channel formation. The plots for Case-2 are shown in Figure 8.6.

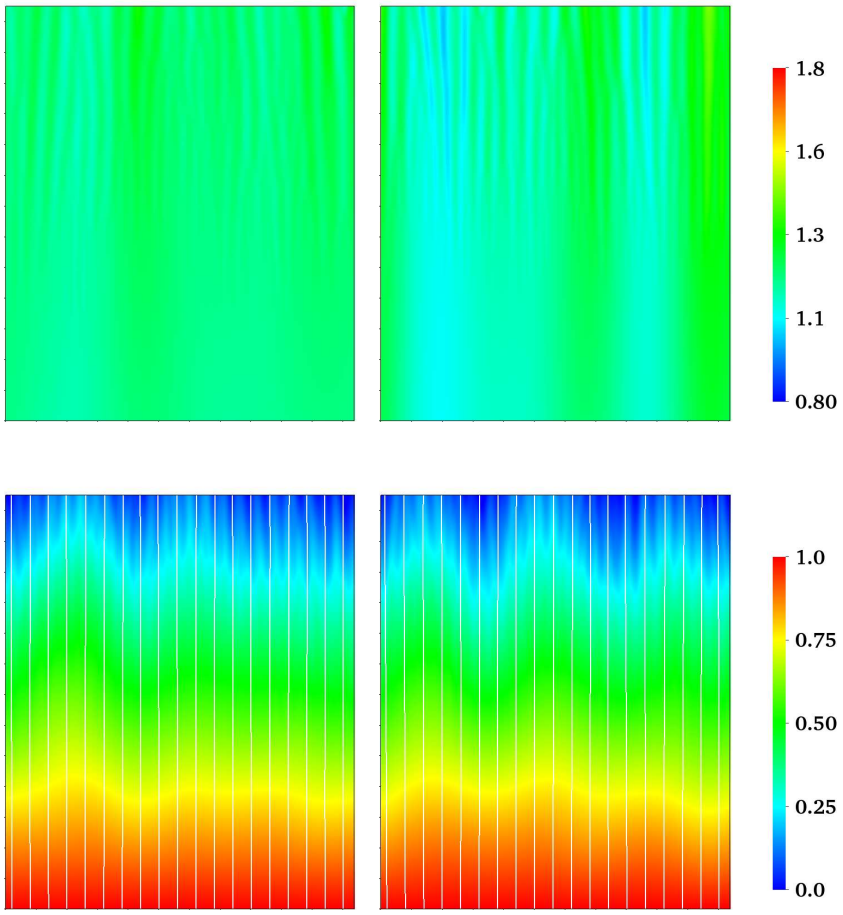


Figure 8.5: Porosity (top) and opx (bottom) distributions at $t = 16$ and $t = 40$ for the x-directional permeability dominating. Computational domain is $(x, z) \in [0, 5.7] \times [0, 6.75]$.

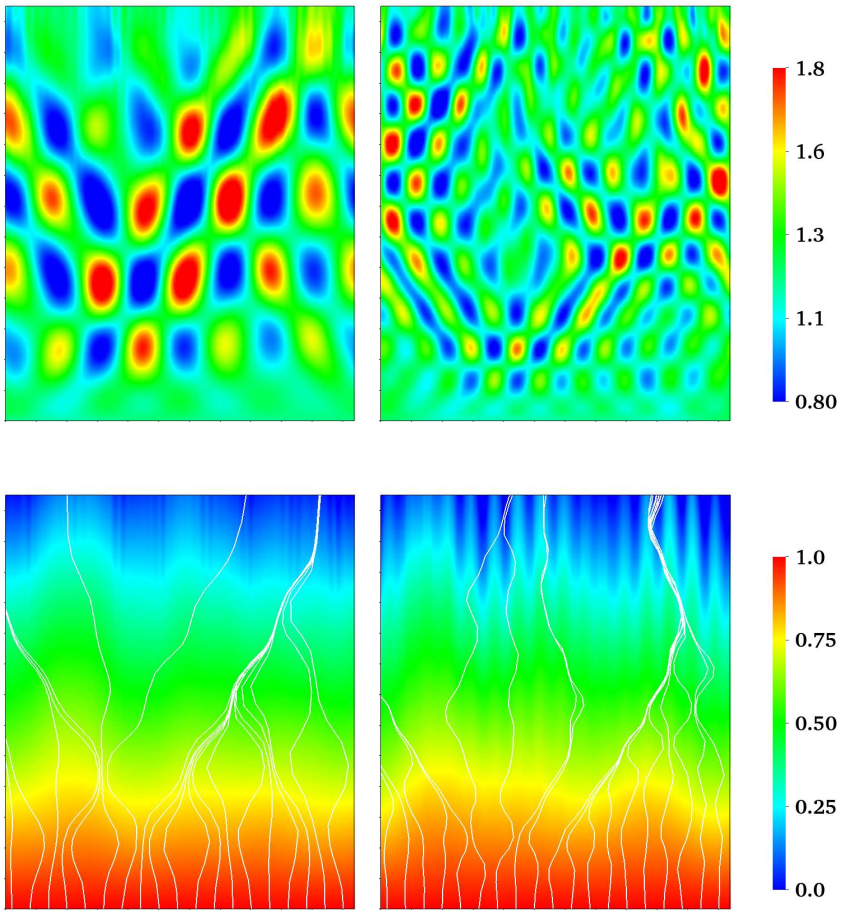


Figure 8.6: Porosity (top) and opx (bottom) distributions at $t = 16$ and $t = 40$ for the z-directional permeability dominating. Computational domain is $(x, z) \in [0, 5.7] \times [0, 6.75]$.

# Chapter 9

# Summary and Further Discussion

## 9.1 Possible Extensions

The work done in this thesis is by no means exhaustive. While it answers some of the important questions arising in geosciences, there are other factors that need to be studied in detail to get a complete understanding of the physics of melt migration. A lot of questions remain unanswered on dunite channels like the factors that control the width of dunite channel, the affect of corner flows or the chemical variations during melt migration in the upwelling mantle. DG methods should be an attractive option to deal with these convection dominated problems as well. The computational tools to achieve the results in this thesis are freely available and should provide a good headstart overcoming the need to start from scratch and hopefully help tackle the challenges of numerical modeling of magma dynamics.

On the mathematical side, while computational methods have been developed to study the usefulness of local timestepping methods, there is no theoretical estimate on the CFL condition to be met for local timestepping methods. Multi-phase flows in general have a weak dependence on pressure. So it will be interesting to see if local time stepping methods and projective pressure estimation methods can be extended to other coupled hyperbolic-elliptic equations especially like the ones arising in oil

recovery and polymer electrolyte fuel cells where, like in magma dynamics, solving the elliptic equation accounts for the major computational time.

## 9.2 Summary

The main contributions of this thesis are summarized below:

- **Discontinuous Galerkin Methods for Melt Migration Simulations:** There have been various topics that have been discussed throughout this thesis. The common theme to all chapters has been to develop accurate, high order numerical methods using discontinuous Galerkin methods to model melt migration in an upwelling mantle. Scalable, robust and high order numerical methods were developed to model magma migration in an upwelling mantle. Isotropic and anisotropic mesh refinement strategies were also discussed. Usage of limiters and entropy viscosity to control numerical oscillations was also discussed. Dunite channel features in 2D and 3D and the physics of melt migration in an upwelling column were studied in detail. Numerical results were validated using the linear stability analysis done previously by Hesse *et al.* Characteristics of porosity waves were also quantified. Transient numerical simulations reveal new insight into the full, nonlinear system. The numerical method developed in this study enables the study of an important but unresolved geological problem regarding the shape or geometry of high-porosity channels in 3D. Influence of other factors in melt migration such as variable viscosity, shearing and temperature was also briefly studied. Results in Chapter 8 provides the framework for studying the impact of shearing and melting in dunite channel formation.

- **Local Timestepping Methods:** Pressure equation only weakly affects the porosity and opx equations in the channel regime computations of melt migration. The CFL condition that is dictated by the smallest cell diameter in

an initially variable or adaptively refined mesh can highly constrain the time step and solving the pressure equation at every time step is very costly. Local timestepping methods prove to be an efficient alternative to bypass this problem. While local timestepping methods have been used to solve only hyperbolic equations, the pressure constraint can also be solved locally by using DG methods for the pressure equation as well.

- **Projective Pressure Estimation Methods:** A new estimator was developed taking advantage of the slow changes in pressure with time. The estimator requires fast computations of matrix-vector products and for this matrix-free methods were used to compute the estimator. Matrix-free methods also help in reducing the memory to store the matrix elements especially for $3D$ problems. Projective pressure estimation also helps in solving the pressure equation faster by providing a much better initial guess to the solution.

# Bibliography


[1] E. Abreu, J. Douglas, F. Furtado, and F. Pereira. Operator splitting for three-phase flow in heterogeneous porous media. *Commun. Comput. Phys.*, 6:72–84, 2009.

[2] E. Aharonov, J. Whitehead, P.B. Kelemen, and M. Spiegelman. Channeling instability of upwelling melt in the mantle. *J. Geophys. Res.*, 100:433–450, 1995.

[3] J. F. Andrus. Stability of a multi-rate method for numerical integration of ODEs. *Computers and Mathematics with Applications*, 25(2):3–14, 1993.

[4] U. M. Ascher and Linda R. Petzold. *Computer Methods for Ordinary Differential Equations and Differential-Algebraic Equations*. Society for Industrial and Applied Mathematics, 1998.

[5] C. Baltzell, E. M. Parmentier, Y. Liang, and S. Tirupathi. The effect of shearing on the buoyant migration of melt in compacting-dissolution channels. *AGU conference*, 2013.

[6] W. Bangerth, R. Hartmann, and G. Kanschat. deal.ii: A general-purpose object-oriented finite element library. *ACM Transactions on Mathematical Software*, 2007.

[7] D. Bercovici, Y. Ricard, and G. Schubert. A two-phase model for compaction and damage 1. General theory. *J. Geophys. Res.*, 106:8887–8906, 2001.

[8] M. G. Braun and P. B. Kelemen. Dunite distribution in the oman ophiolite: Implications for melt flux through porous dunite conduits. *Geochemistry, Geophysics, Geosystems*, 3:1–21, 2002.

[9] O. Buneman. Diagnosing oscillatory growth or decay. *J. Comput. Phys.*, 29:295–296, 1978.

[10] A. Burbeau, P. Sagaut, and C. H. Bruneau. A problem-independent limiter for high-order Runge-Kutta discontinuous Galerkin methods. *Journal of Computational Physics*, 169(1):111–150, 2001.

[11] S. L. Butler. The effects of buoyancy on shear-induced melt bands in a compacting porous medium. *Physics of the Earth and Planetary Interiors*, 173:51–59, 2009.

[12] Mark H. Carpenter and Christopher A. Kennedy. Fourth-order 2n-storage Runge-Kutta schemes. NASA TM 109112, NASA Langley Research Center, 1994.

[13] C. C. Chueh, N. Djilali, and W. Bangerth. An h-adaptive operator splitting method for two-phase flow in 3d heterogeneous porous media. *SIAM Journal on Scientific Computing*, 35:B149–B175, 2013.

[14] C. C. Chueh, M. Secanell, W. Bangerth, and N. Djilali. Multi-level adaptive simulation of transient two-phase flow in heterogeneous porous media. *Computers and Fluids*, 39:1586–1596, 2010.

[15] B. Cockburn, B. Dong, and J. Guzmán. Optimal convergence of the original DG method for the transport-reaction equation on special meshes. *SIAM Journal on Numerical Analysis*, 46:1250–1265, 2008.

[16] B. Cockburn, S. Hou, and C. W. Shu. TVB Runge-Kutta local projection discontinuous Galerkin finite element method for conservation laws IV: The multidimensional case. *Math. Comp.*, 54:545–581, 1990.

[17] B. Cockburn, S. Y. Lin, and C. W. Shu. TVB Runge-Kutta local projection discontinuous Galerkin finite element method for conservation laws III: One dimensional systems. *Journal of Computational Physics*, 84:90–113, 1989.

[18] B. Cockburn and C. W. Shu. TVB Runge-Kutta local projection discontinuous Galerkin finite element method for conservation laws II: General Framework. *Mathematics of Computation*, 52:411–435, 1989.

[19] B. Cockburn and C. W. Shu. The Runge-Kutta local projection P1-discontinuous Galerkin finite element method for scalar conservation laws. *Mathematical Model and Numerical Analysis*, 25:337–361, 1991.

[20] B. Cockburn and C. W. Shu. TVB Runge-Kutta local projection discontinuous Galerkin finite element method for conservation laws V: Multidimensional systems. *J. Comput. Phys.*, 141:199–224, 1998.

[21] B. Cockburn and C. W. Shu. Runge-Kutta discontinuous Galerkin methods for convection-dominated problems. *Journal of Scientific Computing*, 16:173–261, 2001.

[22] J. Van der Ven and J. J. W. Van der Vegt. Space-time discontinuous Galerkin finite element method with dynamic grid motion for inviscid compressible flows: I. General Formulation. *Journal of Computational Physics*, 182(2):546–585, 2002.

[23] C. W. Gear and D. R. Wells. Multirate linear multistep methods. *BIT Numerical Mathematics*, 24(4):484502, 1984.

[24] A. Ghods and J. Arkani-Hamed. Melt migration beneath mid-ocean ridges. *Geophys. J. International*, 140:687–697, 2000.

[25] F. X. Giraldo, J. S. Hesthaven, and T. Warburton. Nodal high-order discontinuous Galerkin method for the spherical shallow water equations. *J. Comput. Phys.*, 181:499–525, 2002.

[26] N. Goedel, S. Schomann, T. Warburton, and M. Clemens. Local timestepping discontinuous Galerkin methods for electromagnetic RF field problems. *3rd European Conference on Antennas and Propagation*, 2009.

[27] M. A. Hesse, A. R. Schiemenz, Y. Liang, and E. M. Parmentier. Compaction dissolution waves in an upwelling mantle column. *Geophys. J. Int.*, 187:1057–1075, 2011.

[28] J. S. Hesthaven, T. Warburton, C. Chauviere, and L. Wilcox. High-order discontinuous Galerkin methods for computational electromagnetics and uncertainty quantification. *Scientific Computing in Electrical Engineering*, pages 403–412, 2010.

[29] J.S. Hesthaven, S. Gottlieb, and D. Gottlieb. *Spectral Methods for Time-Dependent Problems*. Cambridge University Press, 2006.

[30] J.S. Hesthaven and T. Warburton. *Nodal Discontinuous Galerkin Methods: Algorithms, Analysis, and Applications*. Springer, 2008.

[31] I. J. Hewitt. Modelling melting rates in upwelling mantle. *Earthplanet. Sci. Lett.*, 300:264–274, 2010.

[32] C. Johnson and J. Pitkaranta. An analysis of the discontinuous Galerkin method for a scalar hyperbolic equation. *Mathematics of Computation*, 46:1–26, 1986.

[33] R. Katz. Porosity-driven convection and asymmetry beneath mid-ocean ridges. *Geochem. Geophys. Geosyst.*, 10, 2010.

[34] R. Katz and M. Spiegelman. An introduction to coupled magma/mantle dynamics, 2013.

[35] P. B. Kelemen, G. Hirth, N. Shimizu, M. Spiegelman, and H. J. B. Dick. A review of melt migration processes in the adiabatically upwelling mantle beneath oceanic spreading ridges. *Phil. Trans. R. Soc. Lond.*, 355:282–318, 1997.

[36] P.B. Kelemen. The origin of the land under the sea. *Scientific Americal 300*, 2:52–57, 2009.

[37] T. Keller, D. A. May, and B. J. P. Kaus. Numerical modelling of magma dynamics coupled to tectonic deformation of lithosphere and crust. *Geophys. J. Int.*, 186:641–664, 1997.

[38] A. Kloeckner. *High-Performance High-Order Simulation of Wave and Plasma Phenomena*. PhD thesis, Brown University.

[39] L. Krivodonova. Limiters for high-order discontinuous Galerkin methods. *Journal of Computational Physics*, 226(1):879896, 2007.

[40] M. Kronbichler and K. Kormann. A generic interface for parallel cell-based finite element operator application. *Computers and Fluids*, 63:135–147, 2012.

[41] Y. Liang, A. Schiemenz, and M. Hesse. Waves, channels, and the preservation of chemical heterogeneities during melt migration in the mantle. *Geophys. Res. Lett.*, 38, 2011.

[42] Y. Liang, A. Schiemenz, M. Hesse, E. M. Parmentier, and J. S. Hesthaven. High-porosity channels for melt migration in the mantle: top is the dunite and bottom is the harzburgite and lherzolite. *Geophys. Res. Lett.*, 37(L15306), 2010.

[43] D. McKenzie. The generation and compaction of partially molten rock. *J. Petrol.*, 25:713–765, 1984.

[44] C. Pirard, J. Hermann, and H. O'Neill. Melt transport in the mantle: transition from dunite channels to pyroxenite dykes in the upper mantle section of New Caledonia. *Geochmica et Cosmochimica Acta*, 73, 2009.

[45] W.H. Reed and T.R. Hill. Triangular mesh methods for the neutron transport equation. Technical Report LA-UR-73-479, Los Alamos Scientific Laboratory, 1973.

[46] Y. Ricard. Physics of mantle convection. *Treatise on Geophysics, 7: Mantle Dynamics*, pages 31–87, 2009.

[47] A. Richter, J. Stiller, and R. Grundmann. Stabilized high-order discontinuous Galerkin methods for aeroacoustic investigations. *Computational Fluid Dynamics*, pages 77–82, 2009.

[48] G. R. Richter. An optimal-order error estimate for the discontinuous Galerkin method. *Mathematics of Computation*, 50:75–88, 1988.

[49] B. Riviere. *Discontinuous Galerkin Methods For Solving Elliptic And Parabolic Equations*. Frontiers in Applied Mathematics, 2008.

[50] Y. Saad. *Iterative methods for sparse linear systems.* SIAM Publishing, 2003.

[51] A. Sandu and E. Constantinescu. Multirate explicit Adams methods for time integration of conservation laws. *Journal of Scientific Computing*, 38(2):229–249, 2009.

[52] A. R. Schiemenz, M. A. Hesse, and J. S. Hesthaven. Modeling magma dynamics with a mixed fourier collocation-discontinuous Galerkin method. *Commun. Comput. Phys*, 10(2):433–452, 2011.

[53] A. R. Schiemenz, Y. Liang, and E. M. Parmentier. A high-order numerical study of reactive dissolution in an upwelling heterogeneous mantle: I. channelization, channel lithology, and channel geometry. *Geophys. J. Int.*, 186:641–664, 2012.

[54] D. R. Scott and D. J. Stevenson. Magma ascent by porous flow. *J. Geophys. Res.*, 91:9283–9296, 1986.

[55] C. W. Shu. Discontinuous Galerkin methods: General approach and stability, 2008.

[56] N. H. Sleep. Segregation of magma from a mostly crystalline mush. *Geol. Soc. Am. Bull*, 85:1225–1232, 1974.

[57] M. Spiegelman and R. Katz. A Semi-Lagrangian Crank-Nicolson algorithm for the numerical solution of advection-diffusion problems. *Geochemistry, Geophysics, Geosystems*, 7, 2006.

[58] M. Spiegelman and P. B. Kelemen. Extreme chemical variability as a consequence of channelized melt transport. *Geochem. Geophys. Geosyst.*, 4(7), 2003.

[59] M. Spiegelman, P. B. Kelemen, and E. Aharonov. Causes and consequences of flow organization during melt transport: The reaction infiltration instability in compactible media. *J. Geo. Res.*, 106:2061–2077, 2001.

[60] C. Steefel and A. Lasaga. Evolution of dissolution patterns, in chemical modeling in aqueous systems II. *Am. Chem. Soc.*, pages 212–225, 1990.

[61] A. Tommasi, A. Vauchez, M. Godard, and F. Belley. Deformation and melt transport in a highly depleted peridotite massif form the Canadian Cordillera: Implications to seismic anisotropy above subduction zones. *Earth Planet. Sci. Lett.*, 252:245–259, 2006.

[62] A. W. Woods. Melting and dissolving. *J. Fluid. Mech.*, 239:429–448, 1992.

[63] Q. Zhang and C. W. Shu. Error estimates to smooth solutions of Runge-Kutta discontinuous Galerkin methods for scalar conservation laws. *SIAM Journal on Numerical Analysis*, 42:641–666, 2004.

[64] X. Zhong and C. W. Shu. A simple weighted essentially nonoscillatory limiter for Runge-Kutta discontinuous Galerkin methods. *Journal of Computational Physics*, 232:397–415, 2012.

[65] V. Zingan, J. L. Guermond, J. Morel, and B. Popov. Implementation of the entropy viscosity method with the discontinuous Galerkin method. *Computer Methods in Applied Mechanics and Engineering*, 253:479–490, 2012.